

---

# Particle hydrodynamics with tessellation techniques

Steffen Heß

---



München 2011



---

# Particle hydrodynamics with tessellation techniques

Steffen Heß

---

Dissertation der Fakultät für Physik  
an der  
Ludwig–Maximilians–Universität München

angefertigt am  
Max-Planck Institut für Astrophysik

vorgelegt von  
Steffen Heß  
aus Roth

München, den 2. Mai 2011

Erstgutachter: Prof. Dr. Simon D. M. White  
Zweitgutachter: Prof. Dr. Andreas Burkert  
Tag der mündlichen Prüfung: 3. Juni 2011



# Contents

<b>Zusammenfassung</b>	<b>xi</b>
<b>1 Introduction</b>	<b>1</b>
1.1 The $\Lambda$ CDM model . . . . .	2
1.2 Cosmic structure formation . . . . .	2
1.3 Numerical simulations . . . . .	4
1.4 Thesis outline . . . . .	5
<b>2 Hydrodynamical simulation methods</b>	<b>7</b>
2.1 The Euler equations . . . . .	8
2.2 Eulerian methods . . . . .	8
2.3 Lagrangian methods . . . . .	9
2.4 Systematic differences in existing hydrodynamical methods . . . . .	10
2.5 Voronoi particle hydrodynamics . . . . .	14
2.6 Application prospects of VPH . . . . .	15
<b>3 Particle hydrodynamics with tessellation techniques</b>	<b>17</b>
3.1 Introduction . . . . .	17
3.2 Particle based hydrodynamics . . . . .	20
3.2.1 A Lagrangian approach for particle based fluid dynamics . . . . .	20
3.2.2 Density estimates with tessellation techniques . . . . .	21
3.2.3 Equations of motion for Voronoi-based particle hydrodynamics . . . . .	23
3.2.4 Artificial viscosity . . . . .	25
3.2.5 Treatment of mixing . . . . .	27
3.3 Issues of cell regularity . . . . .	29
3.3.1 Viscous forces that help to improve order . . . . .	31
3.3.2 Imposing regularity through the fluid Lagrangian . . . . .	32
3.4 Implementation . . . . .	34
3.5 Test results . . . . .	35
3.5.1 Surface tension . . . . .	35
3.5.2 Sod shock tube . . . . .	37
3.5.3 Dispersion relations . . . . .	37
3.5.4 Density noise and regularity in a settled particle distribution . . . . .	40

3.5.5	Point explosion . . . . .	42
3.5.6	Kelvin-Helmholtz instabilities . . . . .	44
3.5.7	The ‘blob test’: mass loss of a gas cloud in a supersonic wind . . . . .	51
3.5.8	Gravitational collapse of a gas sphere . . . . .	53
3.6	Conclusions . . . . .	58
<b>4</b>	<b>Gas stripping and mixing in galaxy clusters</b>	<b>61</b>
4.1	Introduction . . . . .	61
4.2	Methodology . . . . .	63
4.2.1	Smoothed particle hydrodynamics . . . . .	63
4.2.2	Voronoi particle hydrodynamics . . . . .	64
4.2.3	Hydrodynamical moving-mesh code . . . . .	65
4.3	Isolated galaxies and their evolution . . . . .	66
4.3.1	Gas density maps and structure of the disk . . . . .	67
4.3.2	Star formation rate evolution . . . . .	72
4.4	Galaxy in a wind tunnel . . . . .	72
4.4.1	Initial conditions . . . . .	73
4.4.2	Stripping . . . . .	75
4.4.3	Dependence on resolution and artificial viscosity . . . . .	80
4.4.4	Structure of the wake . . . . .	83
4.5	Stripping of a galaxy during cluster infall . . . . .	89
4.5.1	Setup of galaxy-cluster interaction simulations . . . . .	89
4.5.2	Properties of the head wind . . . . .	89
4.5.3	Gas stripping and star formation truncation . . . . .	92
4.6	Cosmological cluster simulations . . . . .	93
4.6.1	Gas stripping in non-radiative zoom simulations of galaxy clusters . . . . .	94
4.6.2	The Santa Barbara Cluster . . . . .	95
4.7	Discussion . . . . .	101
<b>5</b>	<b>Conclusions</b>	<b>103</b>
<b>A</b>	<b>Voronoi mesh operators and shape control</b>	<b>107</b>
A.1	Differential operators on Voronoi meshes . . . . .	107
A.1.1	Gradient . . . . .	107
A.1.2	Divergence and curl . . . . .	109
A.1.3	Accuracy of the gradient . . . . .	109
A.2	Controlling the shape of cells . . . . .	111
<b>B</b>	<b>More stripping results for the VPH code</b>	<b>117</b>
B.1	Wind tunnel simulations . . . . .	117
B.1.1	Stripped clumps . . . . .	117
B.1.2	Statistical analysis of resolution elements . . . . .	117
B.1.3	Variable wind properties . . . . .	117

---

References	122
Acknowledgements	130
Curriculum Vitae	132



# List of Figures

1.1	Distribution of galaxies in the 2dFGRS . . . . .	3
2.1	Gas density slices of a stripped cloud . . . . .	11
2.2	Voronoi mesh geometry . . . . .	12
2.3	Density field reconstructions . . . . .	13
3.1	Section of a Voronoi diagram . . . . .	23
3.2	Voronoi tessellations of two point distributions . . . . .	30
3.3	Surface tension effect in SPH . . . . .	36
3.4	Sod shock tube . . . . .	38
3.5	Dependence of the numerical sound speed on wavenumber . . . . .	39
3.6	Mesh geometry in VPH in a settling test . . . . .	41
3.7	Density distribution functions of a settling test . . . . .	42
3.8	Cell-regularity of a noisy flow after relaxation . . . . .	43
3.9	Sedov-Taylor point explosion . . . . .	45
3.10	Thermal and kinetic energies in the Sedov-Taylor point explosion . . . . .	46
3.11	Study of methods in a KH-instability simulation . . . . .	47
3.12	Growth rate of the KH-instability . . . . .	49
3.13	KH-instability test with additional shape correction . . . . .	50
3.14	Evolution of the density for a gas cloud . . . . .	54
3.15	Loss of a gas cloud in a supersonic wind . . . . .	55
3.16	Cell regularity without/with cell regularization . . . . .	56
3.17	Evrard collapse . . . . .	57
3.18	Energy evolution for the Evrard collapse . . . . .	58
4.1	Gas density maps of an isolated galaxy . . . . .	68
4.2	Vertical structure of an isolated galaxy . . . . .	69
4.3	Density maps of newly formed stars in an isolated galaxy . . . . .	70
4.4	Profiles of density and pressure in an isolated galaxy . . . . .	71
4.5	Evolution of the SFR of an isolated galaxy . . . . .	73
4.6	Gas density maps of a galaxy in a wind tunnel . . . . .	74
4.7	Loss of star-forming ISM of a galaxy in a wind tunnel . . . . .	77
4.8	Maps of star formation density of a galaxy in a wind tunnel . . . . .	78

4.9	Star-forming gas plus stars of a galaxy in a wind tunnel . . . . .	79
4.10	Stellar density maps of a galaxy exposed to a supersonic wind . . . . .	80
4.11	Resolution study of the mass loss of a galaxy in a wind tunnel . . . . .	81
4.12	Loss of gas mass of a galaxy in a wind tunnel . . . . .	83
4.13	Dependence of the stripping efficiency on the strength of shape correction .	84
4.14	Gas density and specific entropy in a wind tunnel . . . . .	85
4.15	Temperature maps of a galaxy encountering wind . . . . .	86
4.16	Velocity spectrum of our wind tunnel . . . . .	87
4.17	Properties of the ‘headwind’ . . . . .	90
4.18	Spatial distribution of lost gas of an infalling galaxy . . . . .	91
4.19	Gas mass loss of an infalling galaxy . . . . .	93
4.20	Star formation rate for an infalling galaxy . . . . .	94
4.21	Radial dependence of gas fraction of specific substructures . . . . .	96
4.22	Radial dependence of mean gas fraction of substructures . . . . .	97
4.23	Resolution study of the Santa Barbara cluster with VPH . . . . .	98
4.24	Comparison of the Santa Barbara cluster for different codes . . . . .	99
A.1	Illustration of the integration variables . . . . .	108
A.2	Relative error in the gradient estimate . . . . .	110
B.1	Loss of star-forming ISM gas . . . . .	118
B.2	Distribution of resolution elements over density . . . . .	119
B.3	Sum of star forming gas plus new stellar mass in a variable wind . . . . .	120
B.4	Infalling galaxy: sum of mass of star-forming gas and formed stars . . . . .	121

# Zusammenfassung

Um Galaxien, Galaxienhaufen oder noch größere Strukturen im Universum zu simulieren, benötigt man eine angemessene Behandlung der in diesen Fällen dominanten Kraft, der Gravitation. Darüber hinaus ist im Hinblick auf eine korrekte Nachbildung auch kleinerer Details eine Simulation des in diesen Objekten vorhandenen Gases notwendig. Eine Möglichkeit zur Simulation der Hydrodynamik bei astrophysikalischen Problemen bietet das etablierte Lagrange'sche Verfahren "Smoothed Particle Hydrodynamics (SPH)". Diese Methode empfiehlt sich besonders wegen ihrer intrinsischen geometrischen Flexibilität und ihrer Fähigkeit, die Auflösung mit der Dichte automatisch zu erhöhen. Damit ist SPH in der Lage, Gas mit sehr großen Unterschieden in Geschwindigkeit und Dichte angemessen zu simulieren. Neuere Untersuchungen zeigten aber, dass SPH in Situationen, in denen große Dichtesprünge auftreten, ungenau wird. Hier kann es zu einem unterdrückten oder unphysikalisch verlangsamtem Wachstum von hydrodynamischen Instabilitäten kommen. Die Probleme von SPH mit diesen Instabilitäten können letztlich vor allem auf systematisch bedingte Ungenauigkeiten in der Dichtebestimmung dieser Methode zurückgeführt werden.

Um diese Probleme zu vermeiden, haben wir eine neue Methode entwickelt, um die Hydrodynamik in astrophysikalischen Systemen zu simulieren. Dabei wird die Dichte der Simulationsteilchen mit Hilfe eines zusätzlichen Gitters bestimmt. Dieses Gitter ist eine Voronoi Pflasterung, die auf den Positionen der Simulationsteilchen basiert. Zur Erzeugung des Voronoi Gitters verwenden wir eine angepasste Version der Triangulationsroutinen aus dem AREPO Code. Die Pflasterung des Raumes wird dabei durch einen inkrementellen Algorithmus erzeugt, der zunächst das topologisch duale Delaunay-Gitter erstellt, aus dem dann am Ende das Voronoi Gitter berechnet wird. Im Vergleich zu SPH erhöht der Einsatz eines Voronoi Gitters die effektive Auflösung, da die Dichtebestimmung nur mit Hilfe benachbarter Punkte erfolgt. Wichtiger ist jedoch, dass mit Hilfe dieses Prinzips hydrodynamische Instabilitäten korrekt simuliert werden können.

Da unsere neue "Voronoi Particle Hydrodynamics" (VPH) genannte Methode genauso wie SPH eine künstliche viskose Kraft benötigt, haben wir als erstes die Simulation von Schockwellen getestet, um sicherzustellen, dass das Gas sich in den Schockwellen korrekt aufheizt. Es zeigte sich, dass VPH Schockwellen ähnlich genau simulieren kann wie SPH. Die Simulation von turbulenten Strömungen gelingt in VPH dagegen besser. Wir haben daher VPH als vollwertige Alternative zu SPH in dem parallelen kosmologischen Code GADGET-3 implementiert. Das erlaubt uns auch, alle vorhandenen Implementierungen

zur Simulation zusätzlicher physikalischer Prozesse (z.B. Sternentstehung, Kühlung durch Wärmestrahlung usw.) sofort weiter zu nutzen.

Situationen, in denen Scherströmungen entlang großer Dichtesprünge, hydrodynamische Instabilitäten oder Turbulenz auftreten, sind besonders ungünstig für SPH, da es hier zu großen Ungenauigkeiten kommen kann. Daher erwarten wir dort den größten Unterschied zu SPH. Eine Anwendung, in der genau solche Situationen zu erwarten sind, ist der Einfall einer Galaxie in einen Galaxienhaufen. Dabei verliert die Galaxie aufgrund des Staudrucks des anströmenden Galaxienhaufen-Gases mehr und mehr ihres eigenen Gases an den Galaxienhaufen. Dieser Verlust an Gas hängt signifikant davon ab, wie gut die verwendete Methode zur Simulation der Hydrodynamik die auftretenden Instabilitäten in der Umströmung der Galaxie nachbilden kann. Da SPH aufgrund seiner Dichtebestimmung und seiner vollständigen Unterdrückung von Mischungsprozessen auf der Skala einzelner Gasteilchen diese Instabilitäten nicht korrekt simuliert, ermittelt SPH einen zu geringen Verlust von Gas. Wir konnten dies mit Hilfe unserer Simulationen belegen, die außerdem verdeutlichen, dass unsere neue VPH-Methode viel besser mit dem Gitter-basierten AREPO Code übereinstimmt, welchen wir ebenfalls zu einem zusätzlichen Vergleich nutzten. Auch die Eigenschaften des bereits an der Galaxie vorbeigeströmten Gases sind unterschiedlich. So ist das von der Galaxie abgelöste Gas in den SPH Simulationen deutlich dichter und kompakter, so dass es dadurch sogar effizienter neue Sterne bilden kann als das in VPH Simulationen der Fall ist.

Wir haben unsere Resultate aus hoch aufgelösten Windtunnel-Rechnungen sowohl mit Simulationen von Galaxien, die in einen komplett modellierten Galaxienhaufen fallen, als auch mit kosmologischen Simulationen von sich bildenden Galaxienhaufen überprüft. In all diesen Simulationen bestätigte sich, dass in SPH der Gasverlust der einfallenden Galaxien zu gering ist. Desweiteren ist der Gasverlust in den AREPO Simulationen stets am höchsten, während VPH eine mittlere Stellung einnimmt. Wir führen die verbleibende, kleine Diskrepanz zwischen VPH und dem Gitterverfahren in AREPO auf die unterschiedliche Behandlung von Mischungsprozessen auf der Skala der Auflösungsgrenze zurück.

Wir konnten insgesamt zeigen, dass unsere neue VPH-Methode in Situationen mit großem Dichtekontrast eine Verbesserung zu dem Lagrange'schen Verfahren SPH darstellt. Auch wenn unsere Resultate keine vollständige Übereinstimmung mit dem Gitter-basierten AREPO Code zeigen, stellen sie doch eine wichtige Annäherung zwischen Teilchen- und Gitter-basierten hydrodynamischen Verfahren dar. VPH empfiehlt sich vor allem als eine gegenüber SPH verbesserte Methode zur Simulation von hydrodynamischen Prozessen in kosmologischen Problemen.



To my wife and daughter



# Chapter 1

## Introduction

Astronomy is one of the oldest scientific fields of humankind, and pondering about the origin and fate of the Universe has always exerted a deep fascination on people. However, only over the course of the last century, cosmology has been put on a firm scientific basis, made possible by the discovery of general relativity and Hubble's observation of the expansion of the Universe. Since then, revolutionary progress in our understanding of the Universe has been achieved, culminating in what is now called a standard cosmological model.

In this picture, the Universe starts out in a 'Big Bang', characterized by an early hot and dense state. This is deduced both from the observation of an expanding Universe, and the detection of the cosmic microwave background (CMB) radiation, which is the thermal relic radiation of the hydrogen plasma that existed before the universe cooled enough to form neutral hydrogen and leave this radiation field behind. Today, the radiation has cooled down to just 2.73 K and forms a nearly perfect black body radiation spectrum. Indeed, the regularity of the observed CMB radiation indicates that the Universe was not only very hot but also spatially very homogeneous and smooth at the time of recombination. Yet, modern observations with satellites such as WMAP have been able to detect tiny fluctuations around the mean temperature of the CMB, showing that there have been, after all, very small deviations around this high degree of homogeneity. These fluctuations are interpreted to be the seeds of cosmic structure formation. However, it is still a subject of intense research to understand how complex structures such as galaxies have grown out of these initial fluctuations and produced the highly clustered state of today's Universe.

One of the primary tools used to study this process are cosmological hydrodynamical simulations. It will be the primary topic of this thesis to improve these methods by proposing and validating novel hydrodynamical simulation techniques. Before we discuss this in detail, we here briefly recall some of the most basic aspects of the standard cosmological model and cosmic structure formation.

## 1.1 The $\Lambda$ CDM model

Currently, the most widely used theoretical framework for cosmology is the Lambda-Cold-Dark-Matter model ( $\Lambda$ CDM). It proposes that the Universe is filled by dark energy and dark matter besides the baryonic matter; in fact, today, the total energy density is dominated by dark energy, and the total matter content by dark matter. The concept of dark energy is introduced to support the measured accelerated expansion of the Universe, which can only be understood if there is something that counteracts the attractive force of gravity. Dark matter is postulated in order to account for a diverse set of observations where the gravitational pull of the baryonic matter alone falls short of explaining the dynamics. This is for example the case in the rotation curves of galaxies, in the motion of galaxies in clusters of galaxies, or in systems that exhibit strong gravitational lensing.

The missing mass is believed to be in the form of a new elementary particle which interacts only gravitationally with itself and ordinary baryonic matter. Hence this dark matter behaves as a collision-less fluid. In the specific variant of *cold* dark matter (CDM) models, the “cold” refers to the velocities of the particles at decoupling. If the particles are massive enough, these velocities will be non-relativistic and quickly decay, such that the thermal velocities of the dark matter particles at the beginning of structure formation are unimportant. In this situation, structures grow “bottom-up” in a hierarchical fashion, with small objects forming first and then building up every bigger structures later on.

The parameters of the  $\Lambda$ CDM model are now quite tightly constrained, especially by the most recent 7-year data release of the WMAP-satellite (Jarosik et al. 2010), but also by a host of other observations, for example the detection of baryon acoustic oscillations (BAO) in the distribution of galaxies (SDSS and 2dFGRS, Percival et al. 2010; Cole et al. 2005, see also Figure 1.1), or observations of distant type-Ia supernovae. These supernovae serve as “standard candles” and provide a relation between their magnitude and redshift (Kowalski et al. 2008), allowing a measurement of the acceleration parameter. Within the  $\Lambda$ CDM model, these combined observations lead to a universe where the dark energy (here taken to be a cosmological constant) contributes 72.8% to the energy density, dark matter accounts for 22.7%, and baryonic matter for 4.56% (likeliest parameters from Jarosik et al. 2010). Today’s expansion rate is described by a Hubble constant of  $70.4 \text{ km s}^{-1} \text{ Mpc}^{-1}$ , and looking backwards for 13.75 billion years would show the “Big Bang”, a state where the energy density becomes so large that ordinary physics ceases to be applicable. It is remarkable that despite the in principle unknown contents of dark matter and dark energy, the  $\Lambda$ CDM model manages to yield a remarkably successful explanation of cosmic structure formation.

## 1.2 Cosmic structure formation

The formation of structure in the universe can be traced back to small perturbations in the matter density of the early universe, left behind by the Big Bang. The theory of inflation conjectures that the origin of these fluctuation ultimately lies in quantum noise that has

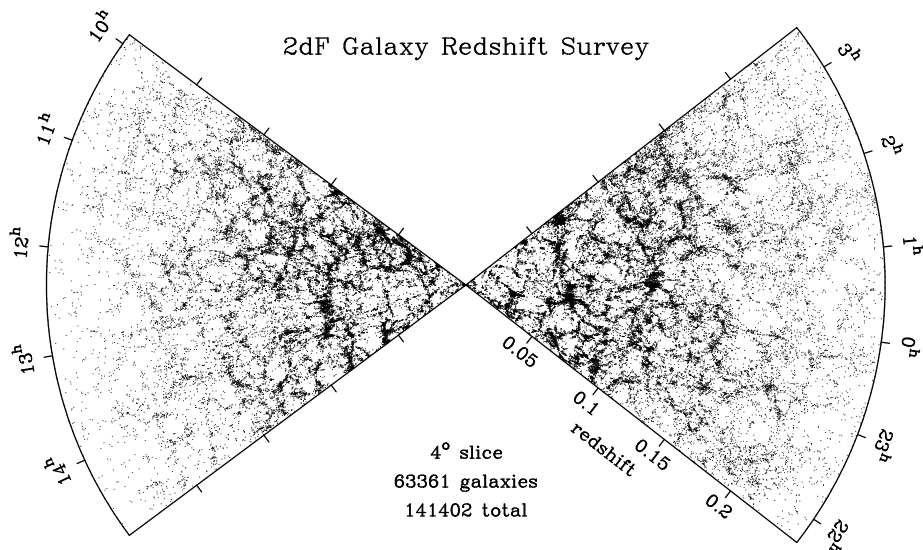


**Figure 1.1:** The distribution of galaxies in the Two Degree Field Galaxy Redshift Survey (2dFGRS) (from Cole et al. 2005). Drawn is a fraction of the total of 141,402 galaxies in a slice that is 4 degrees thick.

been greatly amplified and stretched to macroscopic scales during an inflationary epoch in the very earliest phase of the Big Bang. Once the inflation has stopped, the dark matter particles have been created, and the fluctuations have entered the horizon, they can start to grow due to gravitational instability.

Because the cold dark matter (CDM) has negligible inherent pressure, even small perturbations can grow and reach densities where they collapse non-linearly. First, small objects composed of CDM form. They then subsequently accrete more mass and merge into bigger objects. This hierarchical formation of structure is purely driven by gravity, as the CDM particles do not interact via electromagnetic forces. In contrast, baryonic matter also experiences hydrodynamic pressure forces, in addition to being coupled to radiation and magnetic fields.

Initially, the growth of the perturbations can be followed by linear perturbation theory, where the evolution of the density contrast  $\delta = (\rho - \bar{\rho}) / \bar{\rho}$  is governed by

$$\ddot{\delta} + 2(\dot{a}/a)\dot{\delta} + (c_s^2 k^2 - 4\pi G\bar{\rho})\delta = 0. \quad (1.1)$$

Here  $c_s$  is the sound speed (in case of gas), and  $k$  is the comoving wavelength of the growing mode in an expanding universe with scale factor  $a$ . However, the linear theory is only accurate for  $\delta \ll 1$ . Once structures exceed this limit, their growth accelerates. Eventually, a perturbation decouples from the background expansion, it turns around and collapses under its own gravity in the so-called non-linear regime of structure formation, where the density contrast in the center of objects reaches  $\delta \simeq 10^8$  and more. Here linear theory can not be applied any more, and it becomes extremely challenging to carry out any analytical calculations. Moreover, on these small scales, the effects of gas physics

become relevant, which are hard to describe anyway due to their often inherently non-linear character. In order to tackle this problem, one needs to resort to direct numerical simulations, which offer a flexible and powerful method to follow the evolution of structures far into the non-linear regime.

### 1.3 Numerical simulations

The development of new telescopes and instruments has led to an explosive growth of data gathered through observations. As a result, cosmological measurements have already reached a high level of precision, and increasingly demand ever more accurate theoretical predictions in order for a proper interpretation. In particular, of key importance is a detailed understanding of cosmic structure growth, linking the observations of the high redshift universe (including the initial conditions observed in the CMB) to observations of the local Universe.

Unfortunately, as already pointed out, the growth of dark matter perturbations into non-linear halos cannot be modelled analytically with precision. While statistical descriptions of the clustering of matter in the non-linear regime can be constructed, as for example in the Press-Schechter formalism (Press and Schechter 1974), these approaches ultimately rely on a calibration through numerical simulations. Without the latter, one would have little knowledge about the accuracy of such approximations. Also, the analytic fitting functions are often quite limited in their information content. For example, Press and Schechter (1974) methods do not provide spatial information about the halo distribution.

This emphasizes the importance of numerical simulations for the study of cosmic structure formation. And since the dark matter dominates the matter content (it accounts for about  $\sim 85\%$  of the mass), it is primarily important to simulate the dark matter accurately. The method of choice for this purpose are cosmological N-body simulations, which discretize the dark matter in terms of a set of simulation particles. These N-body simulations follow purely self-gravitating collision-less systems based on methods first comprehensively described by Hockney and Eastwood (1981). Over the years, cosmological N-body codes have reached a high degree of accuracy. These methods are now quite well understood and mature, allowing them to make significant contributions to the investigation of the  $\Lambda$ CDM model and to elucidate its properties.

Among the most important findings established by collision-less N-body simulations is the existence of a cosmic web, together with a quantitatively precise understanding of the halo abundance as a function of mass, and the spatial distribution of the halos at different times (Helly et al. 2003; Springel et al. 2005b). Importantly, the internal structure of the halos themselves (Navarro et al. 2004; Gao et al. 2004), as well as their content of substructures has been determined accurately. Interestingly, an approximately universal shape of CDM halos has been established, which can be described by the NFW-profile (Navarro et al. 1996), or by fits based on the Einasto profile (Einasto 1965). These predictions for the mass distribution have also led to accurate predictions for strong and weak gravitational lensing effects in the  $\Lambda$ CDM model.

While the methods to simulate dark matter are comparatively well understood, implementations of additional physics, especially physics of the baryons are considerably less mature. Generally speaking, they have not reached a similar level of precision yet, and despite a variety of different approaches for tackling gas physics exists, all of these hydrodynamical techniques are fraught with certain problems. This is not an issue on large scales, where gravity is still the dominant force. However, at smaller scales, say at the centers of halos where the actual galaxies form, the numerically very challenging physics of the gas becomes important. Here one would like to combine an accurate treatment of the gravitational interactions of the dark matter with an equally accurate treatment of the baryonic matter, only then the coupled dynamical evolution can be followed reliably. A particular challenge in this context is how a hydrodynamical method can be constructed that can cope with the variety of involved geometries, and the large dynamic range in densities occurring in cosmic structure formation. The traditional method of representing gas on a regular Cartesian mesh is hopelessly inadequate because it can not adjust to the strong clustering of matter. For this reason, particle based discretization schemes, which have an intrinsic adaptivity, have become popular in astronomy. However, as we will see, the methods presently in use have severe accuracy problems in certain situations. It remains therefore an extremely important task to find novel and improved hydrodynamics schemes for the use in cosmic structure formation, which is the goal of this thesis.

## 1.4 Thesis outline

In Chapter 2, we give a brief description of the numerical methods currently in use for simulating hydrodynamics in cosmological simulations, and what challenges these methods face in terms of accuracy and systematic effects. We will also provide an introduction to our new Voronoi particle hydrodynamics method that we propose in this thesis. A full description of the detailed construction of this new approach and of its characteristics is then given in Chapter 3. We turn to applications of our numerical techniques in Chapter 4, which also includes a comprehensive set of comparisons with other hydrodynamical techniques. Finally, in Chapter 5 we summarize the findings from these chapters, draw our primary conclusions, and give an outlook on future work in this area.





# Chapter 2

## Hydrodynamical simulation methods

The baryonic part of the Universe is the one that is most readily accessible by observations, because the baryons are directly or indirectly responsible for almost all the electromagnetic radiation we receive from space. It is hence important to include a proper description of the hydrodynamical interactions of baryons in cosmological simulations to arrive at accurate models of the Universe.

Initially, the baryons start out as homogeneously and smoothly distributed as the dark matter, and on large scales they follow the dynamical evolution of the dark matter. However, the more the dark matter and the baryons cluster into collapsed objects, the more pressure support builds up in the baryonic matter. This thermal pressure supports the gas against further gravitational collapse, similar to the random motions that prevent the dark matter from forming arbitrarily dense objects. However, unlike the dark matter, the gas can give off its thermal energy by emitting cooling radiation. This ultimately allows the gas to collapse much further, forming rotationally supported dense disks that can fragment and eventually create stars. Although the physical laws governing the gas dynamics are in principle well known, the non-linear behaviour of the relevant processes, in particular shocks and gas turbulence, make the hydrodynamics during structure growth extremely complex, such that many aspects are not yet understood in detail. Also, this complexity makes it effectively impossible to treat the problem analytically in a realistic fashion.

For these reasons, there is a substantial demand for reliable numerical treatments of the hydrodynamics during cosmic structure growth. It turns out that this is however substantially more complicated than the N-body method which is so successfully applied for the dark matter. In fact, as we briefly review in this chapter, a number of very different hydrodynamical methodologies are in use in cosmology, but they all have various shortcomings. For this reason we will propose a novel method in this thesis that we show to be able to improve the accuracy of existing techniques, therefore representing an interesting alternative to the established methods.

## 2.1 The Euler equations

Before we present the leading techniques for simulating gas in cosmological situations, a brief overview of the equations of hydrodynamics is in order. Because the cosmic gas is extremely thin, its internal viscosity can be neglected to very good approximation, so that it forms a truly ideal gas. Hence, the inviscid hydrodynamics of the cosmic gas can be described by the Euler equations. In comoving variables, they can be written in their Lagrangian form as:

$$D_t \rho = -\rho \vec{\nabla} \cdot \vec{v}, \quad (2.1)$$

$$D_t \vec{v} = -\frac{\vec{\nabla} P}{\rho}, \quad (2.2)$$

$$D_t u = -P \vec{\nabla} \cdot \vec{v}, \quad (2.3)$$

where  $D_t = \frac{\partial}{\partial t} + \vec{v} \cdot \vec{\nabla}$  is the convective derivative. This set of partial differential equations is completed with an equation of state, which gives the pressure as a function of the other thermodynamic variables. For an ideal gas this can be expressed as

$$P = A \rho^\gamma. \quad (2.4)$$

Here  $A$  is the specific entropy and  $\gamma$  is the adiabatic index. This formulation describes an inviscid gas continuum perfectly, in the absence of shocks. If the latter occur, the entropy  $A$  of gas elements can increase when kinetic energy is dissipated into heat.

Numerical hydrodynamics needs to seek discretizations for these formulae, for which a variety of possibilities exist. Two approaches are mainly used. Either one samples the flow of the gas in terms of constant mass elements that follow the gas motion, or one divides the volume of interest into a grid of stationary finite volume elements. The former approach is typically referred to as ‘‘Lagrangian’’, the latter as ‘‘Eulerian’’.

## 2.2 Eulerian methods

The traditional method to solve the Euler equations employs meshes of some kind, often in a structured form such as Cartesian or polar grids. In the original formulation of this technique, the mesh resolution has been taken to be uniform and constant, but modern methods can also use adaptive mesh refinement (AMR) techniques to implement a resolution that is variable in space and time. There are many different schemes for advancing the Euler equations forward in time on a mesh, but often the conservative character of the equations is directly exploited by calculating the fluxes of conserved quantities (mass, momentum and energy) across cell boundaries. This allows one to automatically fulfill the conservation laws to machine precision, but makes a good estimate of the fluxes all the more important.

For cosmological simulations, the most relevant disadvantage of Eulerian methods is that their mesh is stationary and not automatically adjusts to the strong clumping of matter. While the latter can be overcome to some extent via AMR techniques, the fact that

the mesh is defined in a fixed reference frame renders the results non-Galilean invariant and causes problems for large fluid velocities, which are common in cosmological simulations. Also, the mesh prefers certain directions (the principal coordinate axes), which can introduce spurious artefacts (for example an alignment of disks with the coordinate planes).

## 2.3 Lagrangian methods

Lagrangian methods take a different approach for discretizing the fluid. Instead of dividing the volume into resolution elements, they try to partition the mass. The Lagrangian for an inviscid continuum of gas is given by

$$L = \int \left( \frac{\bar{v}^2}{2} - u \right) dm, \quad (2.5)$$

where  $u$  describes the thermal energy per unit mass. This form of the Lagrangian is very suggestive for a discretization in terms of elements of constant mass. Effectively, this means that the discretization takes place in a moving frame of reference which is defined by the flow of the gas. The resulting equations of motion for the mass elements can be then be interpreted as discretized versions of the Euler equations (2.1), (2.2), and (2.3). The most important conceptual advantage of Lagrangian approaches is that the adaptivity of the method is intrinsic and automatic, in contrast to AMR, where one has to try to approximate this through special refinement strategies.

Smoothed particle hydrodynamics (SPH) as introduced by Lucy (1977a) and Gingold and Monaghan (1977) is the most widely used Lagrangian method in astronomy. Here the Lagrangian evolution of the gas is computed by forces on “fluid particles”, and these forces can be naturally interpreted in terms of pressure gradients. The gradients are estimated by differences with respect to neighboring points, using adaptive kernel estimation techniques. The direct derivation of SPH from the fluid Lagrangian (a discretization of Eq. 2.5) ensures that momentum and energy are conserved accurately, while conservation of mass is guaranteed by construction (since the particle number is constant). A central role in SPH is played by the prescription to estimate the local gas density. In SPH, the densities are obtained with the help of adaptive kernel estimation, which can also be thought of as distributing the masses of particles with a spherically symmetric smoothing kernel. This is a numerically very robust procedure, but it has some intrinsic disadvantages. To begin with, there is no optimal shape of the smoothing kernel, and therefore the performance of SPH depends on the choice of the shape of the kernel. A rather obvious disadvantage is that the smoothing kernel reduces the effective resolution, depending on the radius of the kernel. However, the biggest disadvantage of SPH is that discontinuous jumps in the density field, which for example occur at shocks and contact discontinuities, cannot be represented accurately. Instead they are smoothed over, causing artefacts on both sides of the interface.

Another important issue in SPH lies in the need for an artificial viscosity. Because the inviscid formulation of SPH preserves the specific entropies of its particles by construction, one must add special means to allow dissipation in regions where it is needed. This is normally accomplished by imposing artificial friction forces that try to prevent particles from interpenetrating, such that shocks can be “captured” in a physically meaningful way, and post-shock oscillations are avoided. However, it is difficult to choose these viscous forces in an optimum way, and one usually ends up with slightly viscous behaviour everywhere. Several approaches exist that try to minimize this effect (see e.g. Dolag et al. 2005), but in principle it would be preferable if one could completely avoid the need for an artificial viscosity, similar to grid-based methods that use Riemann solvers.

## 2.4 Systematic differences in existing hydrodynamical methods

Perhaps the most important difference between the Lagrangian SPH method and the Eulerian techniques is that the latter allow for the mixing of entropy and other properties on the resolution scale, whereas in the former such a mixing is completely suppressed at the particle level. Since Eulerian methods simulate hydrodynamics by exchanging fluxes between cells, the averaging (and hence the mixing) over the incoming fluxes from different resolution elements is a central ingredient of the scheme. It is hence ultimately the mass flux across cell boundaries that is responsible for the mixing. While in truly Lagrangian schemes there should be no such mixing, it is questionable whether SPH is correct in preventing it entirely, because in reality the neighbours of a given particle will change with time, indicating that really a “remap” of the associated volume of the particle has taken place. On the other hand, because Eulerian codes introduce mixing for any fluid motion, even pure advection, they likely over-mix to a certain extent. How this different behaviour affects the results of simulations, and which is ultimately the more accurate treatment, is not really settled at this point.

In order to make progress on understanding these systematic differences, a number of comparison projects have been undertaken where a variety of hydrodynamical codes was applied to the same physical problem. In Figure 2.1, we reproduce an important result by Agertz et al. (2007) which shows that SPH suppresses fluid instabilities in shear flows across density discontinuities. This has been traced to spurious, unphysical forces that act to artificially stabilize the interface of contact discontinuities. This spurious surface tension damps or even prevents the development of fluid instabilities, such as Rayleigh-Taylor and Kelvin-Helmholtz instabilities. As a consequence, SPH simulations can yield unphysical results when such fluid instabilities are important. We note that in cosmological simulations such density jumps arise naturally during the hierarchical growth of structure, and they have also been observed directly as “cold fronts” in galaxy clusters. Another important example is a galaxy falling into a cluster, where the correct treatment of fluid instabilities is crucial to predict the interaction of the galaxy’s interstellar medium with

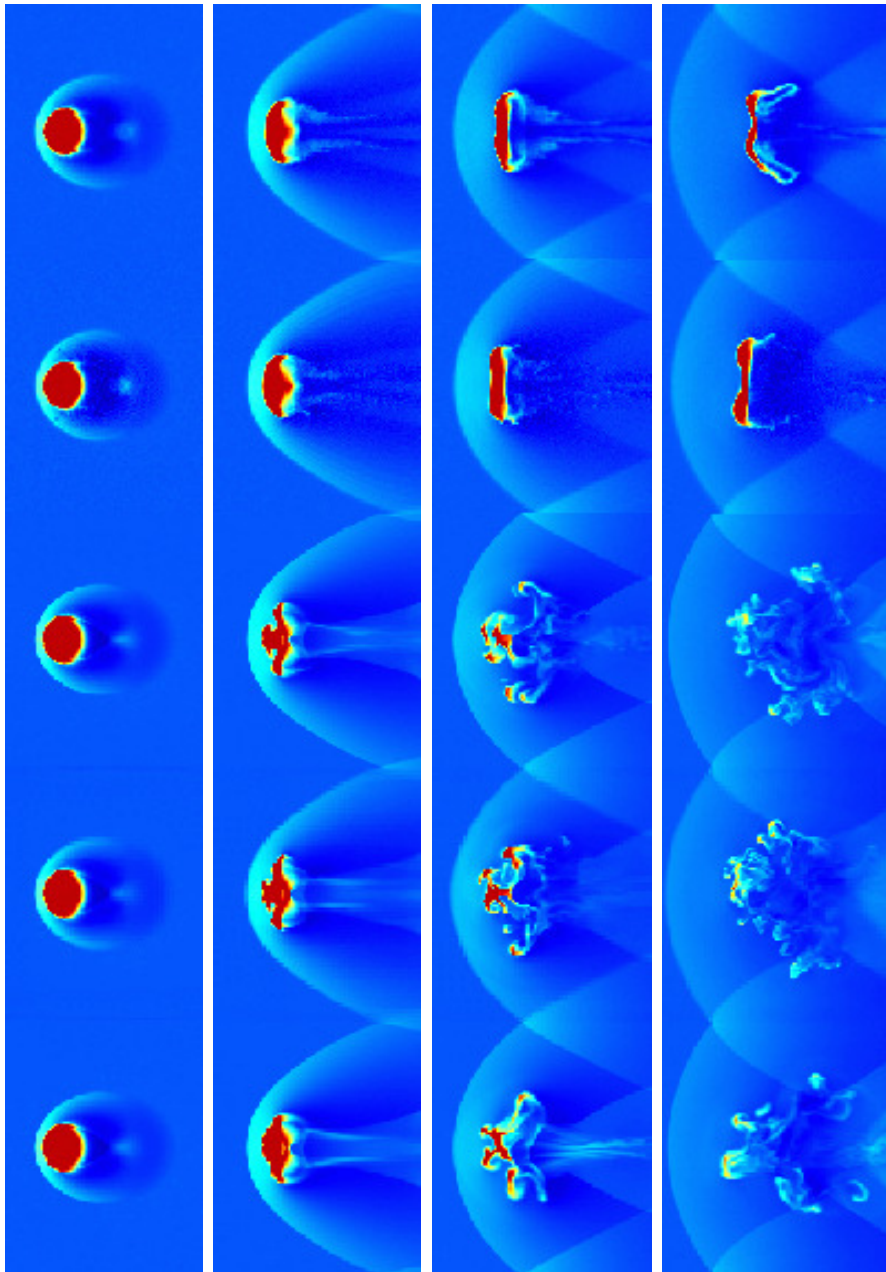


**Figure 2.1:** Gas density slices through the centre of the cloud test of Agertz et al. (2007), at times  $t = 0.25, 1.0, 1.75$  and  $2.5 t_{\text{KH}}$ . From top to bottom, the two SPH-based codes Gasoline, GADGET-2, and the three grid-based codes Enzo, FLASH, and ART-Hydro are compared at equivalent resolutions. The grid-based simulations show a considerably faster dissolving and a complete destruction of the cold dense blob, whereas in SPH a residual part of the blob remains (figure taken from Agertz et al. 2007).

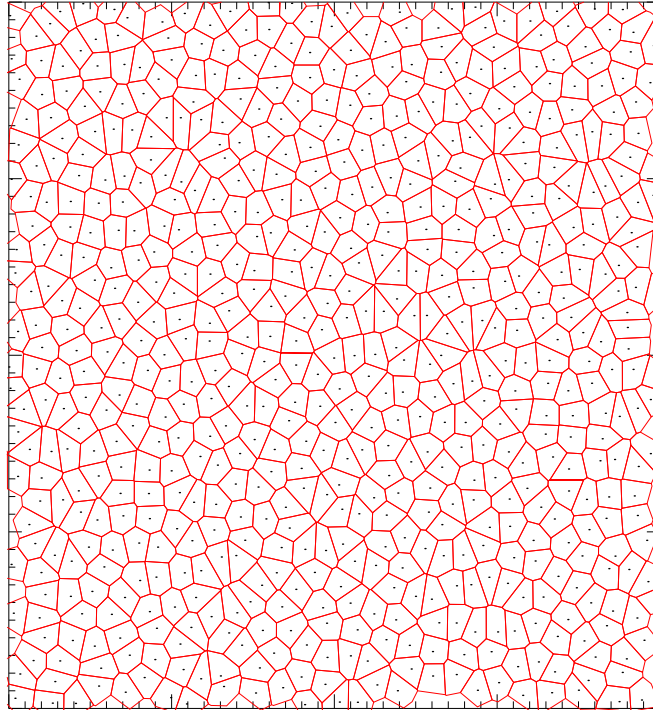


**Figure 2.2:** Voronoi mesh geometry of a relaxed gas distribution simulation with VPH. The region shows simulation particles that have identical mass, specific entropy and volume, and are therefore in pressure equilibrium.

the more tenuous intracluster gas.

Direct comparisons of Eulerian codes and SPH have also shown that the growth rates of fluid instabilities are different (Agertz et al. 2007; Mitchell et al. 2009). Furthermore, these simulation techniques disagree on the thermodynamic state predicted for the gas in rich clusters of galaxies. If radiative losses are neglected, with SPH one finds a lower entropy in the core compared with grid-based methods (Frenk et al. 1999; Mitchell et al. 2009). The origin of this discrepancy is still unclear, however, one can speculate that it is likely related to one or both of the main differences between Eulerian and SPH codes, which are the different treatment of mixing and the unequal capabilities to follow fluid instabilities (Agertz et al. 2007; Tasker et al. 2008; Wadsley et al. 2008a; Mitchell et al. 2009).

In this work, we will primarily focus on finding a way to improve the treatment of fluid discontinuities in particle-based methods such as SPH. Because the problems to accurately represent these interfaces appear to be also the root cause of SPH’s difficulty to model fluid instabilities, one can hope that improving the former will also help with the latter issue. A better density estimate than the one used in SPH may therefore help to greatly reduce the systematic differences between the different hydrodynamical methods.

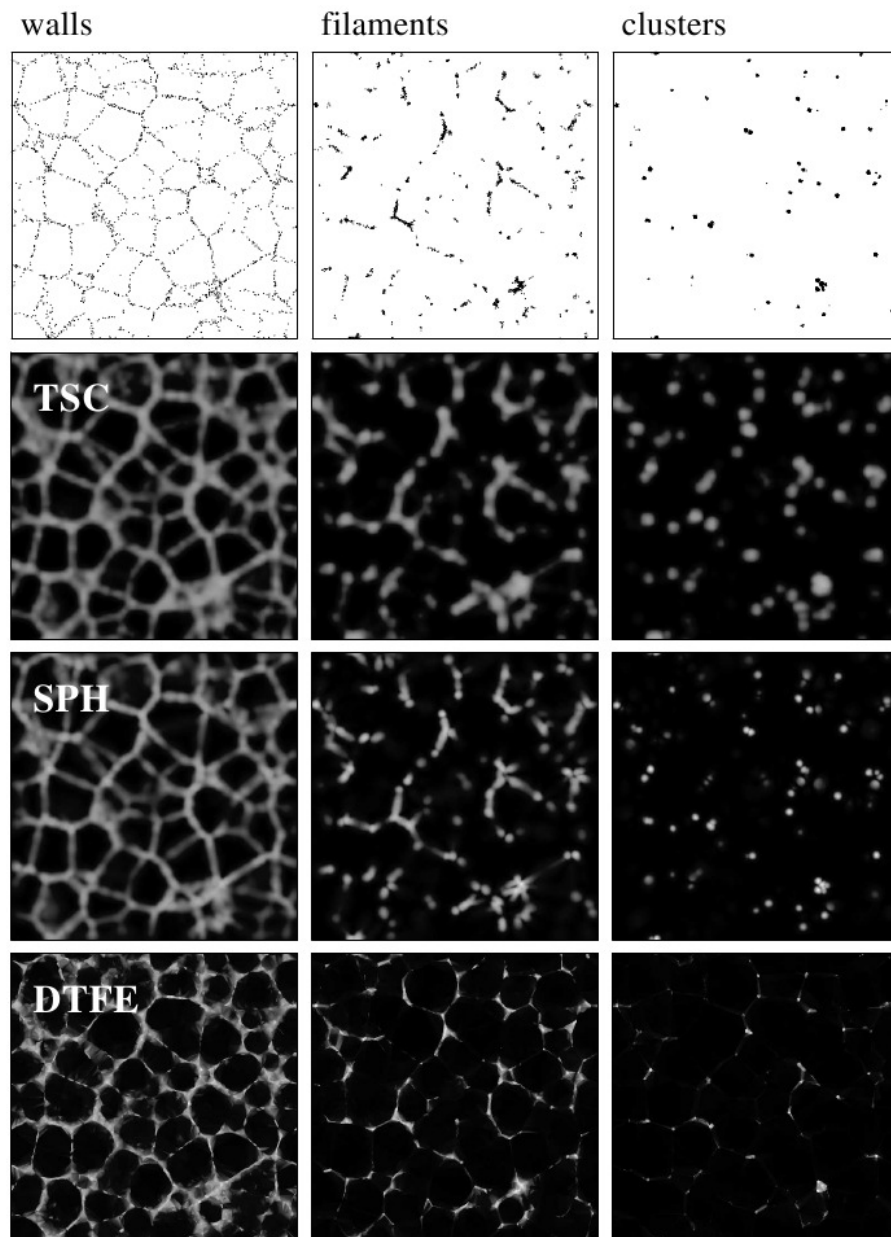


**Figure 2.3:** Slices through density field reconstructions for a toy galaxy distribution (adopted from Schaap 2007). Top row: The different components of the input galaxy distributions drawn as point distribution. Bottom three rows: Density field reconstructions using triangular-shaped-clouds (TSC) binning on a Cartesian grid, SPH or the Delaunay Tessellation Field Estimator (DTFE) method of Schaap (2007).

## 2.5 Voronoi particle hydrodynamics

In this thesis, we propose the new Voronoi particle hydrodynamics (VPH) technique, which is exactly trying to achieve such a fundamental improvement of SPH. It retains the Lagrangian nature of SPH, allowing it to follow advection perfectly and making the scheme Galilean-invariant. Just like in SPH, the flow of gas is also discretized into moving points which have a preassigned mass and a certain specific entropy. The point distribution follows the gravitationally driven growth of structure, such that the point density and therefore the resolution increases in regions that cluster strongly, yielding an automatic adaptivity.

All of these properties of VPH are the same as in SPH, but the main difference lies in the choice of the volume discretization method and in the density estimation. Whereas SPH uses a kernel estimation method to approximate the density field, VPH assigns to each point the volume which is closer to it than to any other point of the distribution (see Figure 2.2). This ‘‘Voronoi tessellation’’ is local as it only involves neighbouring points. That makes it ideal for parallel computing since only the information of the next neighbours in thin regions of overlap have to be synchronized between the computational domains.

The Voronoi mesh is also tightly related to the Delaunay-triangulation, which forms its topological dual. The Delaunay-tessellation is a unique construction where the circum-spheres of each tetrahedron do not contain further points. This unique triangulation of a point-set is dual to the Voronoi tessellation in the sense that each Delaunay edge connecting two points is the normal to the Voronoi face which separates the Voronoi cells of these two points. The tessellation-based volume discretization ensures the best possible resolution for a given set of points, as illustrated in Fig. 2.3 (adopted from Pelupessy et al. 2003). Because the Voronoi tessellation partitions the volume unambiguously, the sum of the volumes associated with each particle really exactly adds up to the total volume, unlike in SPH, where this volume sum can be significantly biased. Because we will define our density estimate as the mass of a particle divided by the associated Voronoi volume, this also means that the density field is represented more accurately. This comes on top of the higher effective resolution of VPH compared to SPH, which originates in the locality of the volume estimate and the absence of smoothing. VPH’s biggest strength lies in its capability to sample and follow shocks, and more importantly density discontinuities, within two resolution elements. Together with VPH’s ability to accommodate large dynamic ranges, these characteristics make VPH an ideal scheme to study cosmological problems.

In this thesis, we will develop VPH as a new method and explore its properties in detail. We expect that it will help to shed light on the origin of the differences that have been found between mesh-based simulations and SPH when applied to the same initial conditions, such as the prominent Santa Barbara cluster comparison project. We will develop a new numerical for VPH that is seamlessly integrated into the existing SPH code GADGET (Springel 2005a). This tight integration is especially ideal for comparisons between VPH and SPH, because it guarantees that self-gravity is treated in exactly the same way in both cases, as well as radiative cooling and sub-resolution treatments of star formation and associated feedback.



In our test applications we will make heavy use of this capability. In particular, we carry out simulations that are sensitive to the suppression of fluid instabilities due to spurious forces at the “surface” of a galaxy as it travels through the intragroup or intracluster medium. This can strongly effect the stripping rate of gas out of galaxies, which is a very important effect for the evolution of galaxies in dense environments.

## 2.6 Application prospects of VPH

Cosmological applications for VPH can be found everywhere where SPH has already been successfully applied. Since they are both Lagrangian techniques, they offer similar advantages, so that one has to weigh SPH’s robustness and simplicity against the higher spatial resolution and numerical accuracy of VPH. If the system under study is significantly influenced by density discontinuities that lead to hydrodynamical instabilities, VPH should however be the better choice. As it can be used as a kind of drop-in replacement for SPH, it is also particularly simple to switch from SPH to VPH, since the treatment of extra physics like cooling or feedback can be carried out in the same way.

We can also expect that employing VPH together with N-body approaches for the dark matter will be an equally successful combination as SPH plus N-body, because the ability to resolve vast density ranges remains. For example, an SPH simulation with dark matter and gravity by Hernquist et al. (1996) was able to reproduce the general distribution of Ly- $\alpha$  absorbers within the  $\Lambda$ CDM paradigm. Other simulations have been used to study the Sunyaev-Zel’dovich effect (da Silva et al. 2000) arising in clusters of galaxies. Yet another area where SPH-based simulations have played an important role is the investigation of galaxy formation and evolution, including the detailed study of merging galaxies (see e.g. Springel et al. 2005a). For all of these problems, VPH is readily applicable and promises to yield more accurate simulation results.

Especially where encounters between galaxies or the interaction of a galaxy with the intracluster medium play an important role, VPH’s more accurate treatment of fluid instabilities should help to significantly improve theoretical predictions in galaxy formation and evolution. VPH may even help to resolve some of the long-standing problems in our understanding of galaxy formation. For example, according to the general picture, galaxy formation starts when gas collapses to gaseous discs inside dark matter halos (see White and Rees 1978). During the collapse, the gas carries its angular momentum with it. Although this basic picture of galaxy formation is widely accepted, crucial aspects of it remain debated, for example the question to what extent the gas flows in as cold streams without ever being shocked, as opposed to gas cooling in a more or less spherically symmetric fashion from a hot, shock-heated halo. Another disputed topic are the massive bulges that are usually found in hydrodynamic simulations of galaxy formation, which could signify both, missing physics or inaccurate numerical techniques. These issues therefore need to be investigated not only by modifying the models for the included physics, but also by testing and refining the hydrodynamical simulation methods, which brings us back to the main goal of this thesis.



# Chapter 3

## Particle hydrodynamics with tessellation techniques

*S. Hess and V. Springel, 2010, MNRAS, 406, 2289*

### **Abstract**

Lagrangian smoothed particle hydrodynamics (SPH) is a well-established approach to model fluids in astrophysical problems, thanks to its geometric flexibility and ability to automatically adjust the spatial resolution to the clumping of matter. However, a number of recent studies have emphasized inaccuracies of SPH in the treatment of fluid instabilities. The origin of these numerical problems can be traced back to spurious surface effects across contact discontinuities, and to SPH's inherent prevention of mixing at the particle level. We here investigate a new fluid particle model where the density estimate is carried out with the help of an auxiliary mesh constructed as the Voronoi tessellation of the simulation particles instead of an adaptive smoothing kernel. This Voronoi-based approach improves the ability of the scheme to represent sharp contact discontinuities. We show that this eliminates spurious surface tension effects present in SPH and that play a role in suppressing certain fluid instabilities. We find that the new 'Voronoi Particle Hydrodynamics' described here produces comparable results than SPH in shocks, and better ones in turbulent regimes of pure hydrodynamical simulations. We also discuss formulations of the artificial viscosity needed in this scheme and how judiciously chosen correction forces can be derived in order to maintain a high degree of particle order and hence a regular Voronoi mesh. This is especially helpful in simulating self-gravitating fluids with existing gravity solvers used for N-body simulations.

### **3.1 Introduction**

Numerical simulations have become an important research tool in many areas of astrophysics, in particular in cosmic structure formation and galaxy formation. This is in part because the physical conditions involved cannot be reproduced in laboratories on Earth, so

that simulations serve as a replacement for experiments. Perhaps more importantly, simulations in principle allow a full modeling of all the involved physics. However, a significant problem in practice is that the equations one wants to solve first have to be numerically discretized in a suitable fashion. The accuracy of simulations depends strongly on the properties of this discretization, and it hence remains an important task to find improved numerical schemes for astrophysical applications.

In cosmic structure formation, matter is initially essentially uniformly distributed, but clusters with time under the action of self-gravity to enormous density contrasts, producing galaxies of vastly different sizes. Given the variety of involved geometries, densities and velocities, it is clear that a Lagrangian method, where the mass of a resolution element stays (roughly) constant, would be most convenient. This is because a Lagrangian method automatically concentrates the resolution in regions where the galaxies form, and hence focuses the numerical effort on the regions of interest. On the other hand, traditional mesh-based approaches to hydrodynamics, so-called Eulerian methods, discretize the volume in a set of cells and do not follow the clustering of matter, unless this is attempted with a suitable adaptive mesh-refinement strategy.

The by far most widely used Lagrangian approach in structure formation is smoothed particle hydrodynamics (SPH, as reviewed by Monaghan 1992, 2005; Rosswog 2009), a technique that dates back to particle-based approaches first developed in astronomy more than 30 years ago (Lucy 1977b; Larson 1978; Gingold and Monaghan 1977). In this method the fluid is discretized in terms of particles of fixed mass, which are used to construct an approximation to the Euler equations based on the adaptive kernel interpolation technique. SPH can be very easily coupled to self-gravity, it is remarkably robust (e.g. negative densities cannot arise), and the introduction of extra physics (e.g. feedback processes in the context of star formation) is intuitive. All of these properties have made it very popular for problems such as planet formation or galaxy mergers (e.g. Dolag et al. 2005; Robertson et al. 2004; Mihos and Hernquist 1996; Mayer et al. 2002), where spatially separated regions of the simulation volume feature widely different densities.

However, recent studies have highlighted a number of differences in the results of SPH-based calculations compared to more traditional grid-based Eulerian methods for hydrodynamics. For example, the two methods appear to disagree about the entropy produced in the central region of a forming galaxy cluster under non-radiative conditions, as first seen in the ‘Santa Barbara cluster comparison project’ (Frenk et al. 1999). It has been suggested that this problem may be caused by a suppression of the Raleigh-Taylor fluid instability in SPH (Mitchell et al. 2009) and the lack of mixing at the particle level (Tasker et al. 2008; Wadsley et al. 2008b). Indeed, Agertz et al. (2007) have shown that SPH tends to suppress Kelvin-Helmholtz fluid instabilities in shear flows across interfaces with sizable density jumps. In such a situation, SPH’s density estimate leads to spurious forces at the interface which produce an artificial ‘gap’ in the particle distribution and a surface tension effect that ultimately produces errors in the hydrodynamical evolution. To what extent these numerical artifacts negatively affect the global accuracy of simulations in practice is unclear, and this can in any case be expected to be problem dependent. However, an improvement of standard SPH that avoids these errors is obviously desirable.

First proposals in this direction have recently been made. Price (2008) suggests to introduce artificial heat conduction into SPH such that discontinuities in the temperature field are smoothed out, in analogy to the ordinary artificial viscosity that effectively smoothes out discontinuities in the velocity field occurring at shocks. This heat conduction produces a soft instead of an abrupt transition of the specific entropy across a contact discontinuity, which in turn helps to better represent the growth of Kelvin-Helmholtz instabilities at such interfaces. More recently, Read et al. (2009) have modified an idea by Ritchie and Thomas (2001) for a modified SPH density estimate that assumes that the local neighbours have similar pressures, and which is designed to avoid the ‘pressure blip’ in the standard approach at contact discontinuities. Together with a modified kernel shape and a drastically enlarged number of neighbours (by a factor of  $\sim 10$ , implying a similar increase in the computational cost), Read et al. (2009) obtained better growth of Kelvin-Helmholtz instabilities across density jumps.

In this work we follow a different approach that eliminates the ordinary SPH kernel altogether. Instead, we use the distribution of points with variable masses to construct an auxiliary mesh, which is then used to derive local density estimates. If the particle hydrodynamics is derived from a Lagrangian, it turns out that obtaining this density estimate is already sufficient to uniquely determine the equations of motion. The use of Delaunay tessellations to construct density fields from arbitrary point sets has been discussed in the literature (Schaap 2007; Icke and van de Weygaert 1987; van de Weygaert and Icke 1989; Pelupessy et al. 2003), but as we show in this chapter, its topological dual, the Voronoi tessellation, is actually preferable for our hydrodynamical application. In the Voronoi tessellation, to every particle a polyhedra is assigned which encompasses the space closer to this particle than to any other. Based on these volumes associated with each particle, local densities and hydrodynamical forces can be estimated, leading to an interesting alternative to SPH. In particular, it is immediately clear that unlike SPH this approach yields a consistent discretization not only of the mass but also of the volume, which should help to yield an improved representation of contact discontinuities. We note that a conceptionally similar approach to Voronoi based particle hydrodynamics was first discussed by Serrano and Español (2001) in the context of a mesoscopic fluid particle model. We here extend this idea to the treatment of the Euler equations in astrophysical systems.

We emphasize that the method we introduce in this study is radically different from to the one implemented in the new AREPO code (Springel 2009). Whereas the latter is also based on a (moving) Voronoi tessellation, it employs a finite volume scheme with a Riemann solver to compute hydrodynamical fluxes across mesh boundaries. This involves an explicit second-order reconstruction of the fluid throughout the volume, and allows for changes of the mass contained in each cell even if the mesh is on average moving with the flow. In contrast, we here derive a fluid particle model from a discretized Lagrangian in which the masses of each element stay strictly constant, and in which the motion of the particles is governed by pairwise pressure force exchanged between them. While AREPO is conceptually close to the techniques used in Eulerian hydrodynamics, the method we study here is conceptually close to SPH.

This chapter is structured as follows. In Section 3.2, we discuss how the equations of

motion can be derived for the Lagrangian particle approach to hydrodynamics discussed here. We will also present suitable formulations of artificial viscosity for our scheme. In Section 3.3, we discuss the role of the regularity of Voronoi cells and means to improve it. We briefly describe the implementation of our numerical scheme in a modified version of the GADGET code in Section 3.4, and then turn in Section 3.5 to a description of results for a suite of test problems with our new ‘Voronoi Particle Hydrodynamics’ (VPH) scheme. These tests range from simple shock-tube problems, to fluid instabilities, and three-dimensional stripping of gas in a supersonic flow. Finally, we summarize our conclusions in Section 3.6. In two Appendices, we discuss gradient operators for Voronoi meshes and give the derivation of correction forces that can be used to maintain very regular mesh geometries, if desired.

## 3.2 Particle based hydrodynamics

We begin by introducing our methodology for a particle-based fluid dynamics based on Voronoi tessellations. This method is close in spirit to SPH, but differs in important aspects. Where appropriate, we discuss these differences in detail.

### 3.2.1 A Lagrangian approach for particle based fluid dynamics

We discretize the fluid in terms of  $N$  mass elements of mass  $m_i$ . The discretized fluid Lagrangian can then be adopted as

$$L = \sum_i \left[ \frac{1}{2} m_i \vec{v}_i^2 - m_i u_i(\rho_i, s_i) \right] \quad (3.1)$$

This is simply the difference of the kinetic and thermal energy of the particles. The thermal energy  $u_i$  per unit mass depends both on the density  $\rho_i$  and the specific entropy  $s_i$  of the particle. In this work, we aim to approximate inviscid ideal gases, hence the equation of state (EOS) is that of a polytropic gas, where the pressure is  $P_i = s_i \rho_i^\gamma$ , and the entropic function  $s_i$  (or simply ‘entropy’ for short, since it depends only on the thermodynamic entropy) labels the adiabat on which this gas element resides.

When the specific entropy  $s_i$  and the mass  $m_i$  remain constant for a fluid element  $i$ , the internal energy  $u_i$  changes according to  $\frac{\partial u}{\partial \rho} = \frac{P}{\rho^2}$ . Using this result, we can readily write down the Lagrangian equations of motion of (reversible) fluid dynamics:

$$\begin{aligned} m_i \ddot{\vec{r}}_i &= - \sum_j^N m_j \frac{\partial u_j}{\partial \vec{r}_i} \\ &= - \sum_j^N m_j \frac{\partial u_j}{\partial \rho_j} \frac{\partial \rho_j}{\partial \vec{r}_i} \\ &= - \sum_j^N m_j \frac{P_j}{\rho_j^2} \frac{\partial \rho_j}{\partial V_j} \frac{\partial V_j}{\partial \vec{r}_i} \end{aligned} \quad (3.2)$$

We see that the primary input required for a more explicit form of the equations is a density estimate based on the particle coordinates, or alternatively, an estimate of the volume associated with a given particle.

SPH addresses this task with a kernel estimation technique to obtain the density, where an adaptive spherically symmetric smoothing kernel is employed to calculate the density based on the spatial distribution of an approximately fixed number of nearest neighbours. The Lagrangian then uniquely determines the equations of motion that simultaneously conserve energy and entropy (Springel and Hernquist 2002). However, we note that SPH does not achieve a consistent volume estimate, i.e. the sum of the effective volumes of the particles,  $V_i = m_i/\rho_i$ , is not guaranteed to be equal to the total simulated volume. Furthermore, the inherent smoothing operation in the density estimate is bound to be inaccurate at contact discontinuities and phase interfaces, where the density may discontinuously jump by a large factor. In the following, we therefore look for alternative ways to construct density estimates which improve on these deficits.

### 3.2.2 Density estimates with tessellation techniques

One promising approach for more accurate density and specific volume estimates lies in the use of an auxiliary mesh that is generated by the particle distribution. A mesh can readily yield a partitioning of the volume such that the total volume is conserved, and also allows multiple ways to ‘spread out’ the particle masses  $m_i$  in a conservative fashion such that an estimate of the density field is obtained.

There are two basic geometric constructions that suggest themselves as such mesh candidates. These are the Delaunay (Dirichlet 1850) and the Voronoi tessellations (Voronoi 1908), which are in fact mathematically closely related, as we discuss below. In the Voronoi tessellation, space is subdivided into non-overlapping polyhedra which each encompass the volume which is closer to its corresponding point than to any other point. The surfaces of these polyhedra are therefore the bisectors to the nearest neighbours. The Delaunay tessellation on the other hand decomposes space into a set of tetrahedra (or triangles in 2D), with vertices at the point coordinates. The defining property of the Delaunay tessellation is that the circumcircles of the tetrahedra do not contain any of the points in their interior. This property in fact makes this tessellation uniquely determined for points in general position.

It turns out that these two tessellations are *dual* to each other; to each edge of the Delaunay tessellation corresponds a face of the Voronoi tessellation, and the circumcircle centres of the Delaunay tetrahedra are the vertices of the Voronoi faces. One implication of this is that the Delaunay and Voronoi Tessellations can be easily transformed into each other. In practice it is typically simpler to always construct the Delaunay tessellation, even if one works with the Voronoi, because the former has more efficient and simpler algorithms for construction.

Both tessellations can in principle be used to derive density estimates. Schaap and van de Weygaert (2000) introduced the Delaunay Tessellation Field Estimator (DTFE) technique, and Pelupessy et al. (2003) showed that it offers superior resolution compared to

SPH-like density estimates for detecting cosmological large-scale structure (for a review see van de Weygaert and Schaap 2009). In this approach, the total volume of the contiguous set of Delaunay cells around a point is used to assign particle densities, and a full density field can be constructed by linearly interpolating the densities inside each Delaunay tetrahedron. As a possible application of this density estimate, Pelupessy et al. (2003) also suggested its use in a particle-based hydrodynamic scheme. However, we caution that a rather serious short-coming of the Delaunay tessellation in this context is that the tessellation may occasionally change *discontinuously* as a function of the particle coordinates. This happens whenever a particle moves over the circumcircle of one of the tetrahedra. An infinitesimal particle motion can hence be sufficient to create finite changes in the volume of its associated contiguous Delaunay cell (this is the union of all Delaunay tetrahedra of which the given point is one of the vertices) of a particle. As a result, the thermal energy of the point set is not a continuous function of the particle coordinates. This makes the DTFE technique ill suited to be the basis of a hydrodynamical particle method.

On the other hand, the volumes of the Voronoi cells always depend continuously on the particle coordinates, despite the fact that topological changes of the tessellation may occur as a result of particle motion. This is because flips of edges in the Delaunay tessellation happen precisely when the corresponding Voronoi faces have vanishing area. Another advantage of the Voronoi tessellation is that it is *always* uniquely defined for any distribution of the points, whereas for certain degenerate point sets (those where more than four points lie on a common circumsphere), more than one valid Delaunay tessellation may exist, which can then make Delaunay-derived density estimates non-unique. We remark that the uniqueness of the Voronoi tessellation does not hold in reverse, i.e. a given Voronoi tessellation can in general be produced by a number of different point distributions. This has important consequences for the stability of the scheme, as we discuss later on in more detail.

Based on the above, the Voronoi tessellation is a promising construction for a particle fluid model, hence we adopt it in the following. In particular, we shall associate the volume  $V_i$  of a Voronoi cell with its corresponding point, yielding a consistent decomposition of the total simulated volume. The simplest possible density estimate is then simply given by

$$\rho_i = \frac{m_i}{V_i} \quad (3.3)$$

which we shall use in this chapter. More involved higher-order density field reconstructions could be considered as well, an idea we leave for future work.

Based on this density estimate, and given the specific entropies of each particle, the local pressure and the thermal pressure per unit mass can be computed. Also, one may define a gradient operator for the Voronoi mesh (see our discussion in Appendix A.1.1), which could be used to estimate pressure gradients, and hence to yield discretizations of the Euler equations. However, a better approach is to start from the discretized Lagrangian, as this automatically gives equations of motion that satisfy the conservation laws. We shall adopt this strategy in the following.



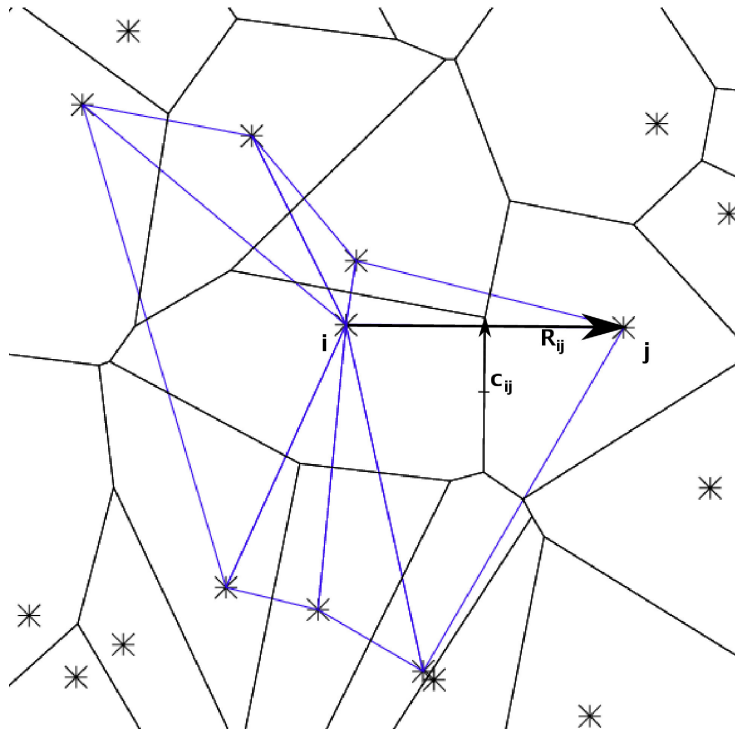


**Figure 3.1:** Section of a Voronoi diagram for a set of points marked with asterisks. All the triangles in the dual Delaunay tessellation that are shared by the point in the centre are marked in blue. The vectors  $\vec{c}_{ij}$  and  $\vec{e}_{ij}$  needed to calculate the derivative of the volume are also marked.

### 3.2.3 Equations of motion for Voronoi-based particle hydrodynamics

Since the volumes of the Voronoi cells depend only on the configuration of the points, we can readily obtain the equations of motion if we find the partial derivative of a cell volume with respect to any of the particle coordinates. We here adopt the result of Serrano and Español (2001), who showed that the relevant derivative is given by (see also De Fabritiis et al. 2006)

$$\frac{\partial V_j}{\partial \vec{r}_i} = -A_{ij} \left( \frac{\vec{c}_{ij}}{R_{ij}} + \frac{\vec{e}_{ij}}{2} \right) \quad \text{for } i \neq j \quad (3.4)$$

where  $\frac{\partial}{\partial \vec{r}_i}$  denotes the gradient operator with respect to  $\vec{r}_i$ . Here  $R_{ij}$  is the distance between two neighboring points,  $\vec{e}_{ij} = (\vec{r}_j - \vec{r}_i)/R_{ij}$  denotes a unit vector from  $i$  to the neighbour  $j$ , which is normal to the Voronoi face of area  $A_{ij}$  between cells  $i$  and  $j$ . Formally, we can define  $A_{ij}$  for any pair of different particles, but if  $i$  and  $j$  are not neighbours in the Voronoi tessellation (i.e. do not share a face), we set  $A_{ij} \equiv 0$ , implying that in sums that involve the factor  $A_{ij}$  only the direct neighbours contribute. Note that equation (3.4) holds only for  $j \neq i$ . But one can readily derive an expression for  $\partial V_i / \partial \vec{r}_i$  by invoking volume

conservation. This yields

$$\frac{\partial V_i}{\partial \vec{r}_i} = - \sum_{j \neq i} \frac{\partial V_j}{\partial \vec{r}_i} \quad (3.5)$$

As sketched in Figure 3.1, the vector  $\vec{c}_{ij}$  points from the midpoint between  $i$  and  $j$  to the centroid of the face  $A_{ij}$ , and is orthogonal to  $\vec{e}_{ij}$ . The term involving  $\vec{e}_{ij}/2$  can be easily understood geometrically from the change of the volumes of the pair of pyramids spanned by the face between  $i$  and  $j$  and the two points. But if the center of the face is displaced from the line connecting  $i$  and  $j$ , a second term involving  $\vec{c}_{ij}$  appears that stems from the turning of the face when the points are moved.

We are now in a position to write down the resulting equations of motion, based on equations (3.2), (3.4) and (3.5). This first yields

$$\begin{aligned} \frac{\partial \rho_j}{\partial \vec{r}_i} = & \frac{m_j}{V_j^2} \left[ (1 - \delta_{ij}) A_{ij} \left( \frac{\vec{c}_{ij}}{R_{ij}} + \frac{\vec{e}_{ij}}{2} \right) \right. \\ & \left. - \delta_{ij} \sum_{k \neq j} A_{jk} \left( \frac{\vec{c}_{jk}}{R_{jk}} + \frac{\vec{e}_{jk}}{2} \right) \right], \end{aligned} \quad (3.6)$$

which then gives rise to the equations of motion in the form

$$m_i \ddot{\vec{r}}_i = \sum_{j \neq i} A_{ij} (P_i - P_j) \left( \frac{\vec{c}_{ij}}{R_{ij}} + \frac{\vec{e}_{ij}}{2} \right) \quad (3.7)$$

This is a rather intuitive result, as it shows that motions are generated by the pressure differences that occur across faces of the tessellation. If the pressures are all equal, the forces vanish exactly, unlike in ordinary SPH.

In the form of equation (3.7), it is not obvious whether the forces between a given pair of particles are antisymmetric. However, noting the identity  $\sum_{j \neq i} A_{ij} \vec{e}_{ij} = 0$ , which follows from Gauss' theorem, we can restore manifest antisymmetry in the equations of motion, which is in general preferable for numerical reasons. To this end, we simply subtract  $P_i \sum_{j \neq i} A_{ij} \vec{e}_{ij} = 0$  from (3.7), yielding our final equations of motion as

$$\begin{aligned} m_i \ddot{\vec{r}}_i = & \\ & - \sum_{j \neq i} A_{ij} \left[ (P_i + P_j) \frac{\vec{e}_{ij}}{2} + (P_j - P_i) \frac{\vec{c}_{ij}}{R_{ij}} \right] \end{aligned} \quad (3.8)$$

which is now pairwise antisymmetric. Note that whereas formally the sums appearing in these equations are carried out over all particles, only the direct neighbours actually contribute, and these are known from the tessellation. In fact, the list of interacting particle pairs is exactly given by the list of edges of the underlying Delaunay tessellation, or equivalently, by the list of faces of the Voronoi tessellation.

We further note that since the equations of motion have been derived from the Lagrangian given in equation (3.1), these equations conserve energy, momentum and entropy

exactly. In the present form they are hence a description of the reversible, adiabatic parts of a flow, but they do not yet contain any dissipation, which is however needed to treat shocks. If no such dissipation is included, shocks will lead to unphysical ringing and oscillations in the fluid.

### 3.2.4 Artificial viscosity

We follow the standard SPH approach (e.g. Gingold and Monaghan 1977; Balsara 1995) and invoke an artificial dissipation in the form of an extra friction force that reduces the kinetic energy and transforms it into heat. There is great freedom in the form of this viscous force, but ideally it should only become active where it is really needed, i.e. in shocks, and should be negligible away from shocks, such that inviscid behavior is ensured there. The most widely used and tested formulation of the viscous acceleration in SPH schemes is given by

$$(\vec{a}_{\text{visc}})_i = - \sum_j m_j \Pi_{ij} \vec{\nabla}_i \bar{W}_{ij}, \quad (3.9)$$

$$\Pi_{ij} = \frac{\bar{f}_{ij}}{\bar{\rho}_{ij}} (-\alpha \mu_{ij} \bar{c}_{ij} + \beta \mu_{ij}^2), \quad (3.10)$$

$$\mu_{ij} = \frac{\bar{h}_{ij} \vec{v}_{ij} \cdot \vec{r}_{ij}}{r_{ij}^2 + \epsilon \bar{h}_{ij}^2}, \quad (3.11)$$

$$\bar{f}_{ij} = \frac{f_i + f_j}{2} \quad (3.12)$$

$$f_i = \frac{|\vec{\nabla} \cdot \vec{v}|_i}{|\vec{\nabla} \cdot \vec{v}|_i + |\vec{\nabla} \times \vec{v}|_i + \epsilon} \quad (3.13)$$

provided that  $\vec{v}_{ik} \cdot \vec{r}_{ik} < 0$ , i.e. the neighboring particles approach each other, otherwise the viscous force that is mediated by the viscous tensor  $\Pi_{ij}$  is set to zero. In this notation,  $q_{ij}$  represents the difference and  $\bar{q}_{ij}$  the average between the quantities  $q$  associated with particles  $i$  and  $j$ . The parameter  $\epsilon$  is a tiny value introduced to guard against numerical divergences. The parameters  $\alpha$  and  $\beta$  set the strength of the viscosity and are typically set to of order  $\sim 1$ . The factors  $f_i$  measure the strength of the local velocity dispersion relative to the local shear, and are introduced as so-called Balsara switch to reduce the viscosity if the local flow is dominated by shear (Balsara 1995).

The above formulation of a viscous force can be adopted to the Voronoi scheme in a number of ways. We first define the projected pairwise velocity as

$$w_{ij} = \frac{\vec{v}_{ij} \cdot \vec{r}_{ij}}{|\vec{r}_{ij}|} \quad (3.14)$$

and make the replacement  $\mu_{ij} \rightarrow w_{ij}$ . This is effectively yielding the ‘signal velocity’ form of the standard viscosity (Monaghan 1997). For simplicity, we shall also adopt the common choice  $\beta = 2\alpha$ . We next recognize that in SPH the viscous tensor is introduced

into the equations of motion as if it was an extra pressure of the form  $P_{\text{visc}} = \frac{1}{2}\rho_{ij}^2\Pi_{ij}$  (Springel 2005b). Using this analogy, and guiding ourselves by the form of the Voronoi-based equations of motion (3.9), we can readily write down a parameterization of the viscous force acting on a particle as

$$m_i(\vec{a}_{\text{visc}})_i = - \sum_j A_{ij}\bar{\rho}_{ij}^2\Pi_{ij}\frac{\vec{e}_{ij}}{2} \quad (3.15)$$

Here we have only introduced a viscous force component parallel to the line connecting the two particles, since we assume that the ‘viscous extra pressure’ is the same for a pair of interacting particles, i.e.  $(P_{\text{visc}})_i = (P_{\text{visc}})_j$ . A more explicit form of the viscous acceleration is given by the following expression:

$$(\vec{a}_{\text{visc}})_i = \alpha \sum_j \frac{\bar{f}_{ij}}{m_i}\bar{\rho}_{ij}A_{ij}(w_{ij}\bar{c}_{ij} - 2w_{ij}^2)\frac{\vec{e}_{ij}}{2} \quad (3.16)$$

Note that the viscous force is pairwise antisymmetric, and will only become active if two particles approach each other. We also want to stress that artificial viscosity parameterizations different from that of equation (3.16) are of course possible. We here simply adopt this form as a first best guess, based on the analogy with the widely tested SPH formulation.

It is interesting to compare the artificial viscosity with the viscosity terms of the Navier Stokes equation,

$$m\frac{D\vec{v}}{Dt} = -\vec{\nabla}P + \eta\Delta\vec{v} + \lambda\vec{\nabla}(\vec{\nabla}\vec{v}) \quad (3.17)$$

Neglecting the shear viscosity  $\eta$  and approximating the gradient operator with its Voronoi discretized form (see Appendix A), this becomes

$$\left(\lambda\vec{\nabla}(\vec{\nabla}\vec{v})\right)_i \simeq \lambda\frac{1}{V_i}\sum_j A_{ij}\frac{\vec{e}_{ij}}{2}(\vec{\nabla}\vec{v})_j \quad (3.18)$$

Additionally approximating

$$(\nabla\vec{v})_j \approx \frac{\vec{v}_{ij}\cdot\vec{r}_{ij}}{|\vec{r}_{ij}|} = w_{ij} \quad (3.19)$$

yields a term like the one linear in  $w$  in equation (3.16), adding some further justification to this form of the viscous force, which has the form of an artificial bulk viscosity.

In order to maintain energy conservation, heat must be produced at a rate  $dE/dt$  that exactly balances the loss of kinetic energy due to the extra friction from the artificial viscosity. We inject this energy symmetrically into the specific entropies of the two particles. Defining the pairwise viscous forces as

$$(\vec{f}_{\text{visc}})_{ij} = -A_{ij}\bar{\rho}_{ij}^2\Pi_{ij}\frac{\vec{e}_{ij}}{2} \quad (3.20)$$

the heating is given by

$$\frac{du_i}{dt} = \frac{1}{2} \sum_j (\vec{f}_{\text{visc}})_{ij} \cdot \vec{v}_{ij} \quad (3.21)$$

With  $u_i = s_i \rho_i^{\gamma-1} / (\gamma - 1)$  this yields for the rate of entropy production

$$\frac{ds_i}{dt} = \frac{\gamma - 1}{2 \rho_i^{\gamma-1}} \sum_j (\vec{f}_{\text{visc}})_{ij} \cdot \vec{v}_{ij} \quad (3.22)$$

In this form, the equations still conserve total energy and momentum, while the change of the total entropy is positive definite.

The artificial viscosity is necessary to capture shocks and to damp postshock oscillations in the vicinity of shocks, but everywhere else in the fluid it can induce spurious dissipation that distorts the physics of an inviscid gas. In order to reduce the influence of the viscosity in regions away from shocks, the prefactor  $\alpha$  that sets the strength of the viscosity can be chosen adaptively (Morris 1997; Dolag et al. 2005). The idea of this dynamic viscosity is that every particle gets an individual viscosity strength  $\alpha$  which is evolved in time according to the differential equation

$$\frac{d\alpha}{dt} = -\frac{\alpha - \alpha^*}{\tau} + S \quad (3.23)$$

Here  $\alpha$  is decaying to a minimum  $\alpha^*$  on a timescale  $\tau$ , and is increased by the source term  $S$ . One possible choice for this source term is

$$S = \bar{f}_{ij} \zeta \vec{\nabla} \cdot \vec{v} \quad (3.24)$$

which we adopt in our implementation of a time-variable artificial viscosity, using the discretized estimate of the divergence described in Appendix A. Here both the response coefficient  $\zeta$  and the timescale  $\tau$  have to be calibrated empirically. When a shock arrives in an unperturbed area,  $\alpha$  is at its minimum and needs to jump very quickly to a higher level in order to capture the shock and prevent post shock oscillations, whereas behind the shock, the viscosity should quickly return to a low value. However, a too large value for  $\zeta$  may trigger high viscosity due to the often noisy estimates of the  $\vec{\nabla} \cdot \vec{v}$  term, and if  $\tau$  is too small, the viscosity may decay too quickly to capture the shock properly. Finally, the minimum viscosity  $\alpha^*$  can be set to a non-zero value to improve particle order and thereby reduce noise, at the cost of introducing some minimum viscosity.

### 3.2.5 Treatment of mixing

Hydrodynamic simulations are able to follow the advection of fluids only down to the resolution scale. But especially Lagrangian schemes do not include mixing processes of the fluid on sub-resolution scales. In Eulerian codes, such mixing is implicit whenever a new averaged thermodynamic state for a cell is computed after fluxes of gas have entered or left it. This mixing keeps the total energy fixed, but will in general raise the entropy of the system. In the Lagrangian particle approach of SPH and in the Voronoi approach

developed here, such mixing effects are, however, entirely suppressed. The specific entropies of neighbouring particles stay constant, except when a shock is present. While this reliably eliminates unwanted entropy production from advection errors, it also prevents the proper subresolution production of entropy when small-scale fluid instabilities should mix the fluid on the resolution scale and produce homogeneous thermodynamic properties.

We have therefore tried to model this subgrid mixing with a heuristic model which conjectures that small-scale fluid instabilities, if present, equalize the local temperature field by mixing. This will then smooth out sharp contact discontinuities and also tend to equilibrate the specific entropies of the cells. Similar ideas have recently been discussed by Price (2008), Wadsley et al. (2008b) and Shen et al. (2009) in the context of SPH, but our approach differs in detail. In particular, we restrict the averaging to shearing layers, and motivate the timescale for mixing directly with the growth timescale of the Kelvin-Helmholtz instability on the resolution scale.

The linear theory growth timescale of a perturbation across a contact discontinuity with densities  $\rho_i$  and  $\rho_j$  that exhibits a jump in the tangential velocity of size  $v_{ij}^{\parallel}$  (a shear layer) is given by

$$t_{\text{KH}} = \frac{\rho_i + \rho_j}{2k v_{ij}^{\parallel} \sqrt{\rho_i \rho_j}} \quad (3.25)$$

Here  $k = 2\pi/L$  is the wavenumber of the Kelvin-Helmholtz mode. We shall assume that  $L$  is of order the cell dimension, which is in turn of order the particle separation, i.e. we will set  $L = R_{ij}$  when a particle pair of separation  $R_{ij}$  is considered. Similarly, the relevant velocity jump is simply the velocity difference projected onto the face between two particles, which is normal to their separation vector, hence

$$v_{ij}^{\parallel} = |\vec{v}_{ij} - (\vec{v}_{ij} \cdot \vec{e}_{ij}) \vec{e}_{ij}| \quad (3.26)$$

We further assume that the fluid mixing on scales below the particle cells can be approximately described as a diffusion process, operating with diffusion constant  $D = \chi L^2/t_{\text{KH}}$ , where  $\chi$  is a dimensional efficiency that controls the strength of the mixing (and which needs to be determined empirically). We hence effectively model the mixing with heat diffusion of the form  $\partial u/\partial t = D\nabla^2 u$ .

Using the SPH discretization of thermal conduction as a guide (Jubelgas et al. 2004), we can readily find a discretization of the heat diffusion for the Voronoi particle discretization. We obtain

$$m_i \frac{du_i}{dt} = 2\pi\chi \sum_j A_{ij} (1 - \bar{f}_{ij}) |v_{ij}^{\parallel}| \sqrt{\rho_i \rho_j} (u_j - u_i) \quad (3.27)$$

Here we introduced a further factor  $(1 - \bar{f}_{ij})$  in a similar manner as in (3.13). This Balsara-like factor is used to restrict the diffusion only to areas where the compression (as measured by  $|\vec{\nabla} \cdot \vec{v}|$ ) is clearly negligible compared to the shear (as measured by  $|\vec{\nabla} \times \vec{v}|$ ).

Note that this equation preserves the total thermal energy, and heat energy only flows from hotter to colder particles. The corresponding rates of entropy change for each particle can be obtained by multiplying with  $(\gamma - 1)/\rho_i^{\gamma-1}$ . While the specific entropy of individual

particles may go down if they give up some of their heat energy, the total entropy of the system increases due to this process, which can be interpreted as providing the necessary mixing entropy.

One important difference of our parameterization of ‘artificial heat conduction’ to the model of Price (2008) is that the mixing only occurs in shear flows, and that contact discontinuities without shear are hence not affected.

We note that due to the parabolic character of the diffusion problem, it can be problematic to integrate equation (3.27) with an explicit time integration scheme, since the von Neumann criterion imposes relatively small timestep limits.

$$\Delta t \leq \frac{(\Delta x)^2}{D} \approx \frac{(\Delta x)}{2\pi\chi|v_{ij}^{\parallel}|} \quad (3.28)$$

where we estimated  $\min\left(\frac{\rho_i+\rho_j}{2\sqrt{\rho_i\rho_j}}\right) = 1$  and assumed  $\Delta x \approx L$ . The CFL criterion is more restrictive than this timestep as long as

$$|v_{ij}^{\parallel}| \ll \frac{1}{2\pi\chi} c_{\text{sound}} \quad (3.29)$$

which is usually the case and hence not too restrictive. Indeed, so far we have not encountered problems with the explicit time integration scheme that is implemented for the mixing at present. If needed, an implicit scheme with perfect stability could however be easily adopted, like the one discussed in Petkova and Springel (2009).

### 3.3 Issues of cell regularity

A common feature of particle hydrodynamic schemes is their ability to automatically provide an adaptive resolution. As a result, dense regions are modelled with better accuracy thanks to their smaller mean distance of particles. But besides the particle number density the regularity of the Voronoi cells is an important factor in determining the achieved precision, as shown in Appendix A.1.3, where we give quantitative results for the accuracy of our gradient estimates as a function of the shape distortions of cells. Highly irregular, sliver-like Voronoi cells may also lead to very small, computationally costly timesteps, because the permissible timestep size is effectively proportional to the distance to the nearest neighbour.

Connected to this problem is the issue of how to safely prevent inter-particle penetrations, which is required for a proper representation of the fluid with its single valued velocity field. If two particles approach each other rapidly, it is possible that the particles pass through each other unless this is prevented with a sufficiently strong artificial viscosity. If the Voronoi mesh is very irregular and features a large number of close particle pairs, it becomes more difficult to ensure this, simply because rather large viscous forces that act over short timescales are required to prevent the small particle separations from becoming

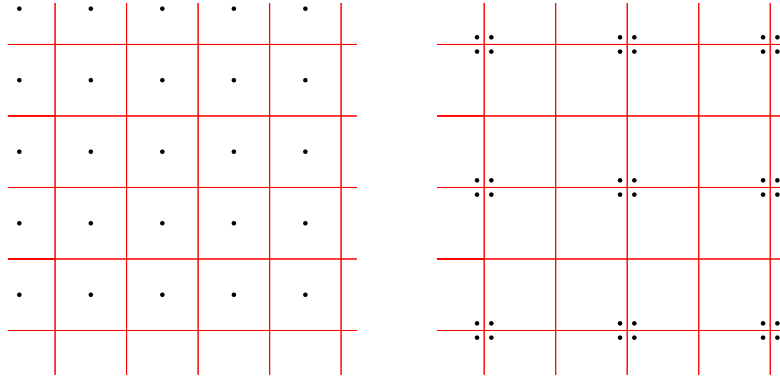


**Figure 3.2:** Two point distributions and their corresponding Voronoi tessellations. The important point illustrated by this example is that *different* point distributions may have *identical* Voronoi tessellations.

still smaller. These problems are significantly alleviated if the tessellation is relatively ‘regular’, i.e. if cells have a small aspect ratio, and if their generating points lie close to the centroids of the corresponding cells.

Figure 3.2 illustrates another important feature of Voronoi meshes, which we may perhaps call ‘mesh degeneracy’. In this example, the mesh for two different point distributions is shown, but in both cases an identical Cartesian Voronoi mesh results, hence the density and pressure estimates are both equal. In fact, one can continue to move the groups of four points around the mesh vertices in a mirrored fashion arbitrarily close towards the corners of the mesh, without changing the situation. If one now imagines adding some random velocity field to the points when they are very close, it is clear that it will be much harder to prevent an erroneous particle crossing in the case where the points are far from the centres of their associated cells than in the case where they sit right at these centres.

One might argue that situations as shown in Figure 3.2 are artificial and hence do not affect the simulation of flows where Voronoi diagrams are seldom that regular. But situations occur where the volume is only slightly increased when particles approach. Also considering a finite timestep these particles’ resistance against a clumping or even interpenetration is then uncomfortably weak.

If possible, it would therefore be desirable to formulate the dynamics such that the mesh automatically maintains a certain degree of regularity. We note that this cannot be expected to happen by itself for the density estimation scheme we implemented thus far. This is again made clear by the example in Figure 3.2, where the pressure gradient vanishes in both cases if the specific entropies and masses of all particles are the same. Below we therefore consider two possible approaches to introduce small correction forces into the dynamics with the goal to rearrange the points to achieve a more regular tessellation.



### 3.3.1 Viscous forces that help to improve order

Experience with our new VPH scheme shows that especially in highly irregular, turbulent flows and in situations with strong gravitational forces some cells can become quite irregular. In this context, we loosely define an irregular cell as one whose generating point is substantially displaced from the centroid of the cell and/or whose aspect ratio is quite high, i.e. a cell with a comparatively large ratio of surface area to volume. In this subsection we consider a scheme where the artificial viscosity is modified such that it serves a second purpose, namely to have the tendency to make cells ‘rounder’.

To this end we introduce the notion of a ‘partial pressure’ for each of the pyramids that make up a Voronoi cell. These pyramids are spanned by the Voronoi faces and the defining point of the cell, which acts as their apex. We define the ‘partial pressure’ of the pyramid of cell  $i$  facing cell  $j$  in terms of its volume  $V_{ij} = A_{ij}R_{ij}/6$  (or  $V_{ij} = A_{ij}R_{ij}/4$  in 2D) and by assigning a share  $m_{ij} = m_i A_{ij} / \sum_k A_{ik}$  of the cell’s mass to the pyramid, i.e. its mass fraction is taken to be proportional to its contribution to the total surface area of the cell. This yields

$$P_{ij} = s_i \rho_i^\gamma = s_i \left( \frac{6 m_i}{R_{ij} \sum_k A_{ik}} \right)^\gamma \quad (3.30)$$

The idea is now to define an additional viscous force between a pair of particles arising from the difference of this partial pressure to the full pressure of the cell. This will lead to rearrangements of the points until the differences in the partial pressures of each pyramid to that of the cell become small, which happens when the point is approximately equidistant to all the faces of its cell, implying a regular cell shape.

We hence make the ansatz

$$(\vec{f}_{\text{order}})_{ij} = -\kappa A_{ij} (P_{ij} - P_i + P_{ji} - P_j) \frac{\vec{e}_{ij}}{2} \quad (3.31)$$

for ‘ordering forces’ between a pair of particles, with the total force on particle  $i$  being given by

$$m_i (\vec{a}_{\text{order}})_i = \sum_{j \neq i} (\vec{f}_{\text{order}})_{ij} \quad (3.32)$$

Here  $\kappa$  is a dimensionless parameter describing the strength of the effect. These forces are antisymmetric, and in general can be both of repulsive and attractive nature. In order to maintain total energy conservation, the work of these forces needs to be balanced in the evolution of the entropies of the particles, similar to what is done for the ordinary artificial viscosity. This yields an additional contribution to the entropy change of the form

$$\frac{ds_i}{dt} = \frac{(\gamma - 1)}{\rho_i^{\gamma-1}} \frac{1}{2} \sum_j (\vec{f}_{\text{order}})_{ij} \cdot \vec{v}_{ij} \quad (3.33)$$

Note that a small local decrease of the entropy sum can result in principle if order is restored in the particle distribution, but this effect is small and has played no role in all our tests. In refinements of the above scheme, it is also possible to make  $\kappa$  spatially and

temporarily variable. For example, we have typically used this scheme in a combination with a switch that only sets  $\kappa > 0$  if there is a strong local compression, because that is where cell shapes distort the most.

When discussing results, we will refer to this method as ‘partial pressure ordering’ or PPO, whereas the method for improved cell regularity discussed in the next subsection will be referred to as ‘shape correction forces’. If none of these additional schemes to regularize cell shapes is employed, we simply refer to the method as the ‘plain Voronoi scheme’.

### 3.3.2 Imposing regularity through the fluid Lagrangian

If irregular cell shapes occur, we ideally would like that small adjustment forces appear naturally that tend to make the mesh more regular again. These adjustment forces should preserve the energy and momentum conservation of the scheme. This will automatically be the case if they are derived from a suitably defined Lagrangian or Hamiltonian. We are hence led to modify the fluid Lagrangian slightly to include factors that penalize highly distorted cell shapes. The idea is that such distorted cells should raise the estimate of the inner energy slightly, such that they become energetically disfavored.

We consider two ways to measure shape distortions of cells, which may either be used individually, or combined. One is based on the displacement of a point from the centroid of its associated cell. The idea here is that it is advantageous if a point stays close to the center of a cell. In particular, as we will discuss in more detail in Section 3.5.3, it turns out that the ordinary VPH scheme is not able to support waves in regular Cartesian grids at the Nyquist frequency, a deficit that could be cured if there is always a (weak) restoring force if a point is displaced from the centre of its Voronoi cell.

The other is to measure the shape directly, and to steer the particle motion such that high aspect ratios are avoided. We construct a shape measure based on the second moment of the cell, which we compare to a suitably defined cell radius. This measure will have a minimum for ‘round cells’, while severe distortions from roundness (like highly elongated cells) should trigger restoring forces.

Both of the above measures of cell regularity can be introduced into the fluid Lagrangian by multiplying the thermal energy with correction factors that increase the energy slightly if a point is displaced from the centroid, or if a cell is elongated. Specifically, we adopt as Lagrangian

$$L = \sum_k \frac{1}{2} m_k \dot{\vec{r}}_k^2 - \quad (3.34)$$

$$\sum_k \frac{P_k V_k}{\gamma - 1} \left[ 1 + \beta_0 \frac{(\vec{r}_k - \vec{s}_k)^2}{V_k^{2/d}} \right] \left\{ 1 + \beta_1 \left( \frac{\vec{w}_k^2}{V_k^{2/d}} - \beta_2 \right) \right\} \quad (3.35)$$

Here  $\vec{r}_k$  is the coordinate of a point,  $V_k$  is the volume of its corresponding Voronoi cell, and

$\vec{s}_k$  is the cell's centroid.  $P_k$  is the ordinary pressure of the cell, where we set  $\rho_k = m_k/V_k$  as usual. The coefficients  $\beta_0$  and  $\beta_1$  are introduced to measure the strength of the correction forces associated with offsets from cell centres, or with high aspect ratios, respectively. For  $\beta_0 = \beta_1 = 0$ , the ordinary fluid Lagrangian of the VPH scheme is recovered.

We define the centroid of a cell as

$$\vec{s}_k \equiv \langle \vec{r} \rangle_k = \frac{1}{V_k} \int \vec{r} \chi_k(\vec{r}) d\vec{r} \quad (3.36)$$

where  $\chi_k$  is the characteristic function of cell  $k$ , i.e.  $\chi_k(\vec{r}) = 1$  if the point  $\vec{r}$  lies in the cell  $k$ , and  $\chi_k(\vec{r}) = 0$  otherwise. The shape of a cell is measured via the second moment

$$\vec{w}_k^2 \equiv \langle (\vec{r} - \vec{s}_k)^2 \rangle_k = \frac{1}{V_k} \int (\vec{r} - \vec{s}_k)^2 \chi_k(\vec{r}) d\vec{r} \quad (3.37)$$

The factors in squared and curly brackets in the Lagrangian of equation (3.34) are the adopted energy correction factors that raise the energy of distorted cells. Here  $d$  counts the number of dimensions, i.e.  $d = 2$  for 2D and  $d = 3$  for 3D. The factor  $V_k^{2/d}$  is hence proportional to the ‘radius’  $R_k = V_k^{1/d}$  of a cell squared.  $\beta_0$  measures the strength of the effect of displacements of points from the centroid of a cell, while  $\beta_1$  is the corresponding factor for the aspect-ratio factor. The constant  $\beta_2$  is only introduced to prevent that even round cells lead to a significant enhancement of the thermal energy. For perfectly round cells, we expect in 2D approximately circles for which  $w_k^2 = V^{2/d}/(2\pi)$ , hence we pick  $\beta_2 = 1/(2\pi)$ . In 3D, we have spherical shapes instead and we pick  $\beta_2 = 3/5(3/4\pi)^{2/3}$ .

The equations of motion for the Lagrangian (3.34) can be derived in closed form for the Voronoi mesh, but due to the length of the resulting expressions we give their derivation in Appendix A.2. The advantage of using the Lagrangian to obtain the cell-shaping forces is that the scheme then still accurately conserves total energy, momentum and entropy, while at the same time remaining translational and rotationally invariant. Also, the correction forces are ‘just right’ to achieve the desired regularity of the mesh, something that is difficult to achieve with any heuristic scheme to derive such forces, like the one we tried in the previous subsection.

In our results section, we show that this method is indeed capable of maintaining nicely regular meshes in the sense described above. However, we also caution that the stronger the extra forces are, the more unwanted features start to appear as well. First of all, the extra forces may introduce subtle deviations from the dispersion relation of an ideal gas, and may lead to spurious motions in situations with pressure equilibrium. The second, probably more serious side effect of this method may occur when the cells cannot easily relax to the desired regular cell structure, for example along a strong jump in density. In this case a pressure anomaly may develop due to the cell-shaping forces, similar to what is found in SPH across contact discontinuities. Still, we find that moderate values of  $\beta_0$  and  $\beta_1$  help to improve the accuracy of the VPH scheme without distorting the inviscid dynamics of an ideal gas too much.

## 3.4 Implementation

We have implemented the above hydrodynamical particle model into the cosmological TreeSPH simulation code GADGET-3, an updated version of GADGET-2 (Springel 2005b; Springel et al. 2001). This code is parallelized for distributed memory machines, and offers high-performance solvers for self-gravity as well as individual and adaptive timestepping for all particles. Our strategy in our modifications has been to implement Voronoi-based particle hydrodynamics as an alternative to SPH within the GADGET-3 code. This is, in particular, ideal for facilitating comparisons between SPH and our Voronoi-based scheme, and it also allows us to readily use all the non-standard physics already implemented in GADGET-3 (e.g. radiative cooling and star formation) for calculations with Voronoi-based fluid particle dynamics.

The primary new code needed in GADGET-3 is an efficient mesh construction algorithm. To this end we adapted and modified the parallel Delaunay triangulation engine from the AREPO code (Springel 2009), and turned it into an optional module of the SPH code GADGET-3. In brief, the tessellation code uses an incremental construction algorithm for creating the Delaunay tessellation. Particles are inserted in turn into an already existing, valid tessellation. To this end, in a first step the tetrahedron in which the new point falls is located, and then it is split into several new tetrahedra, such that the inserted point becomes part of the tetrahedralization. However, some of the new tetrahedra may then not fulfill the empty-circumsphere property, i.e. the tessellation is not a Delaunay triangulation any more. Delaunayhood is restored in a second step by local flip operations that replace two adjacent tetrahedra with three tetrahedra, or vice versa, until all tetrahedra fulfill again the empty-circumsphere property. At this point, the next particle can be inserted. We have implemented the mesh construction both for 3D and 2D within the GADGET-3 code and parallelized it for distributed memory machines.

At the beginning, a large tetrahedron is constructed that encloses the full computational domain. The boundary conditions (always adopted as periodic at the moment) of the rectangular computational domain as well as the boundaries arising from the domain decomposition are treated with ‘ghost particles’. One technically difficult aspect is to make the tessellation code completely robust even in the case of the existence of degenerate particle distributions, where more than 4 points lie on a common circumsphere (or more than 3 points are on a common circumcircle). Detecting such a case robustly and correctly in light of the finite precision of floating point arithmetic is a non-trivial problem. However, the incremental insertion algorithm requires consistent and correct evaluations of all geometric predicates, otherwise it will typically fail in situations with degeneracies or near-degeneracies. We solve this problem by monitoring the floating point round-off in geometric tests, and by resorting to exact arithmetic in case there is a risk that the result of a geometric test may be modified by round-off error.

## 3.5 Test results

In this section, we discuss a number of test problems carried out with our new hydrodynamical particle method, focusing in particular on regimes where differences with respect to SPH can be expected. An application of the method in full cosmological simulations of galaxy formation will be presented in future work.

### 3.5.1 Surface tension

In standard entropy-conserving SPH with particles, there is a subtle surface tension effect across contact discontinuities with a large jump in density. This can be understood as a result of the desire of SPH to suppress mixing of the two phases, because this is energetically unfavorable for fixed particle entropies. For the mixed state, approximately the same average density would be estimated for each particle, which leads to a higher estimate of the thermal energy, unless the thermodynamic entropies are averaged between the particles as well, which is an irreversible process in which entropy is in fact produced if the total energy stays constant.

To demonstrate the existence of the surface tension effect, we have prepared (in 2D for simplicity) an overdense ellipse in a thin background medium, at pressure equilibrium. For definiteness, the density of the ellipse was set to  $\rho_2 = 4$ , that of the background medium to  $\rho_1 = 1$ , with a pressure of  $P = 2.5$ . 3854 equal mass particles in a periodic box of unit length on a side were used to set up the experiment. The particles have been arranged on a coarse Cartesian grid in which an ellipsoidal region was excised. This region has then be filled with a finer Cartesian grid. The specific entropies of the two sets of particles were initialized differently such that an equal pressure for the two phases results. No attempt was made to somehow soften the transition between the two phases. Figure 3.3 shows the initial configuration, as well as the particle distribution after a time  $t = 7$ , both for SPH and for the Voronoi-based fluid particle approach.

Even though the pressures of the particles are formally equal for all particles in the initial conditions, the ellipse transforms to a circle when SPH is used. In contrast, for the VPH scheme, the same experiment maintains the initial shape of the ellipse, modulo some small rearrangements of the points near the boundary, since the initial set-up was not in perfect equilibrium (due to the fact that the point distributions of the two Cartesian grids used to set up the two phases do not match seamlessly at the boundary). Clearly, the numerical realization of the contact discontinuity in SPH gives rise to a spurious surface tension, and this in turn will suppress Kelvin-Helmholtz instabilities below a certain critical wavelength. The VPH approach does not have this problem and can in principle accurately support a contact discontinuity at each face boundary between individual cells. It needs to be stressed however that also in the Voronoi scheme no mixing of the entropies at the particle level happens. If the particles of two phases were simply spatially mixed while keeping their specific entropies constant, the resulting medium would not be at a single temperature or density. We note that the effect is also present for a set-up with unequal particle masses. In this case, the variationally derived entropy-conserving version of SPH

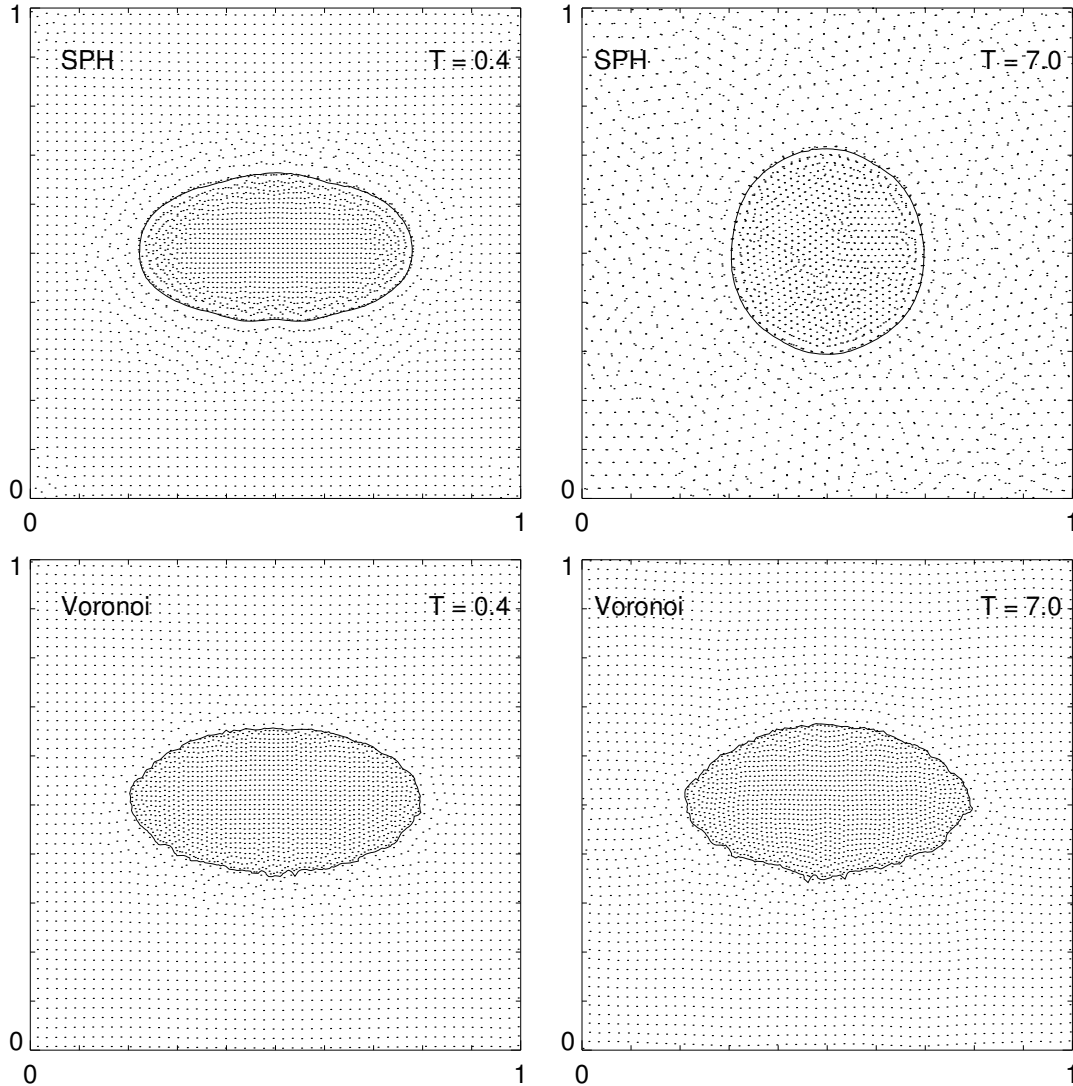


**Figure 3.3:** Surface tension effect in SPH. The left column shows an overdense ellipsoidal region shortly after it is set-up at  $t = 0$  in pressure equilibrium within a thinner background. When evolved with SPH, the ellipsoid slowly transforms into a sphere, as shown by the state of the system after time  $t = 7$  (top left). In contrast, the Voronoi scheme can preserve the shape much better (bottom panels) and shows no sign of surface tension effects.

will however lead to a change of the effective number of neighbours across the contact discontinuity, because it keeps the mass in the kernel volume constant.

### 3.5.2 Sod shock tube

The classic Sod shock tube tests examine the ability of a hydrodynamic scheme to reproduce the basic wave structure that appears in the Riemann problem, namely shock waves, contact discontinuities and rarefaction waves. Also, comparison to the analytic solution gives a useful quantitative benchmark for the accuracy of a scheme.

We consider gas that is initially at rest. In the left half-space, the pressure is  $P_1 = 1.0$  and the density is  $\rho_1 = 1.0$ , whereas in the right half-space we adopt  $P_2 = 0.1795$  and  $\rho_2 = 0.25$ . The adiabatic index is set to  $\gamma = 1.4$ . The same sod shock parameters have previously been used in a number of code tests (e.g. Hernquist and Katz 1989; Rasio and Shapiro 1991; Wadsley et al. 2004; Springel 2005b). When the evolution begins, a shock wave of Mach number  $M = 1.48$  travels into the low-pressure region, and a rarefaction fan moves into the high pressure region. In between, a moving contact discontinuity develops.

In our numerical test of this problem with the VPH scheme we use a 3D setup in a box with dimensions  $(20, 1, 1)$ , where the left and right halves are filled with particles arranged on a Cartesian grid. Altogether 8370 particles with equal masses were used as initial condition. The evolution was then carried out with our default settings for the artificial viscosity until  $t = 3$ . In Fig. 3.4, we compare the numerical result to the analytical solution at this time. Reassuringly, we find quite good agreement of the VPH scheme with the analytical solution. In comparison to SPH, the rarefaction wave in the Voronoi simulation shows a slight dip at the low density end, but not the hump at the high density end that is typical of SPH. Another difference is that the contact discontinuity is sharper and better preserved in the VPH approach. All of the described features appear to be largely independent of how the points are distributed initially as long as the gas is relaxed on both sides. In particular, the arrangement on a Cartesian grid does not lead to any noticeable artifacts compared with simulations where the initial point distribution is less ordered and has a glass-like configuration. However the results are somewhat less accurate for irregular grids (see also A.1.3) when the plain Voronoi scheme is used.

We have also examined the influence of the extra forces that can be enabled to improve the regularity of the mesh (see Sections 3.3.1 and 3.3.2). To this end we tested the effect of the PPO scheme as well as the shape correction method with parameters up to  $\beta_0 = 1.2$ ,  $\beta_1 = 0.1$ . When these ordering forces are invoked, the results for the sod-shock test are in general not influenced much, but the particle noise around the analytical solution is reduced. We also found that the extent of postshock oscillations for weaker artificial viscosity settings tends to be reduced if these ordering methods are used.

### 3.5.3 Dispersion relations

Even though this may seem like a simple test, it is actually important to check how well our new method can simulate small-amplitude<sup>1</sup> acoustic waves, especially at low resolution when few points per wavelength are available. We are especially interested in how accurately the expected dispersion relation is reproduced in this regime, i.e. whether such

---

<sup>1</sup>The amplitude needs to be small in order to prevent wave steepening.

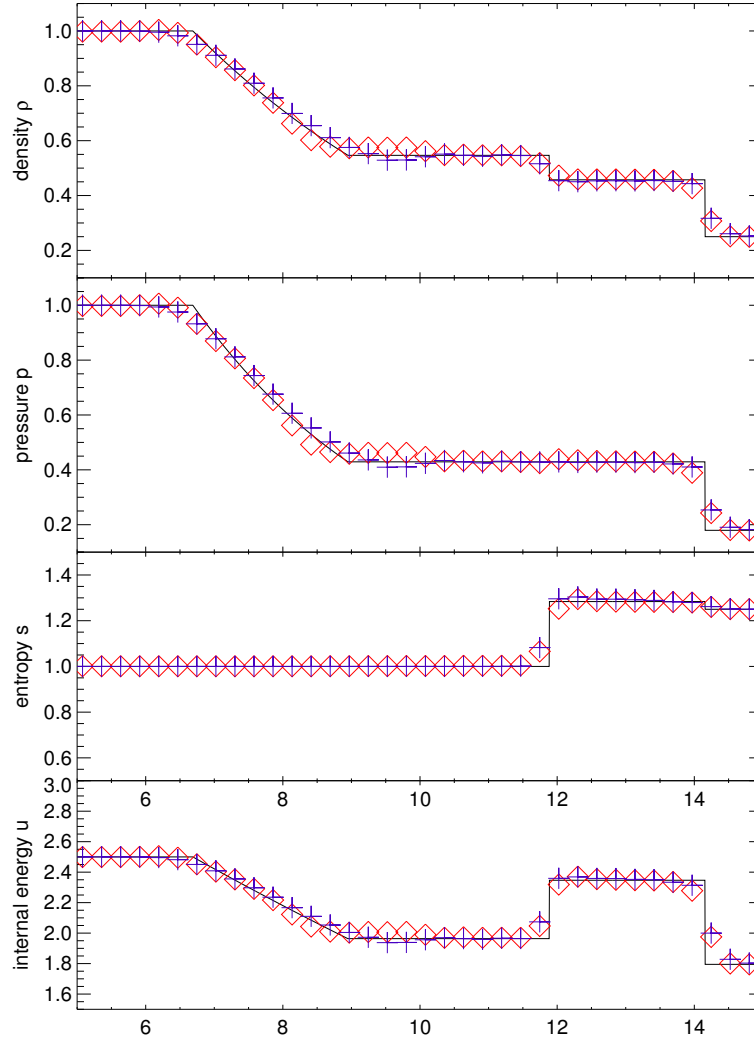


**Figure 3.4:** 3D Sod shock tube simulation at  $t = 3.0$ . We compare results from our Voronoi particle scheme (blue crosses) and the SPH result with 32 neighbours (red diamonds) with the analytical solution (solid lines) in terms of the density, pressure, entropy profiles and internal energy.

waves propagate with the correct speed of sound. A secondary question is how strongly such waves are damped by the artificial viscosity in the scheme.

To measure the dispersion relation, we set up small-amplitude standing waves in a periodic box and measure their oscillation frequency. In Figure 3.5, we compare results for SPH with our Voronoi-based fluid particle model, with and without shape correction forces, as a function of wavenumber. The wavenumber is normalized to the Nyquist frequency of the initial particle grid, such that  $k/k_{\text{Nyquist}} = 1$  corresponds to the shortest wave that can



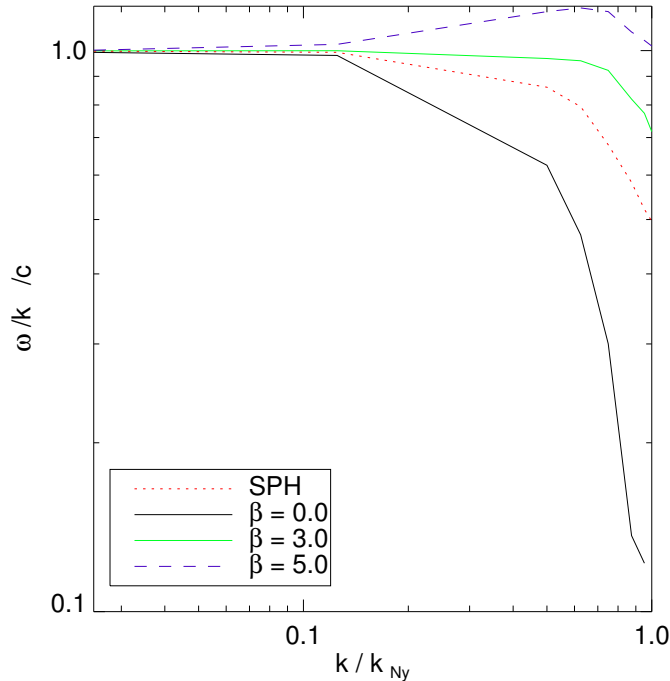


**Figure 3.5:** Dependence of the numerical sound speed on wavenumber, expressed in units of the Nyquist frequency of the underlying particle grid. For the standard VPH scheme, waves at the Nyquist frequency are not propagated properly (hence no frequency can be measured at  $k = k_{Ny}$ ), but this is remedied by the shape correction forces. If they are invoked, the resulting dispersion relation becomes more accurate than that of SPH for all  $k$ .

be represented by the particles. In this standing wave, neighbouring particles oscillate 180 degrees out of phase ‘opposite’ to each other.

A first important result made clear by Figure 3.5 is that for the standard VPH scheme the oscillation frequency for  $k/k_{Nyquist} = 1$  drops to zero, or in other words, such waves are not supported by the scheme at all. This is readily understood from the degeneracy effect pointed out in Figure 3.2. If particles are set-up such that they ‘collide’ in a pairwise fashion, then there is nothing in the reversible part of the dynamics of the VPH scheme that can prevent an interparticle penetration, simply because the pressure gradient stays zero in this case. However, this situation is exactly the one encountered if we prepare a standing wave at the Nyquist frequency of an initially regular particle grid. The wave will not oscillate since the pressure gradient will remain zero, and therefore particle crossings would be inevitable (unless prevented by the artificial viscosity). This is potentially a serious shortcoming of the VPH scheme in its standard form, as it means that it cannot treat waves at around the Nyquist frequency properly.

However, the shape correction force due to  $\beta_0$  has exactly the right property to make

these small waves oscillate again. In fact, we can calculate what value of  $\beta_0$  is required to reproduce the dispersion relation at  $k/k_{\text{Nyquist}} = 1$  exactly. For this value of  $\beta_0 \simeq 5.5$ , we however also get slightly too stiff behaviour of the fluid for somewhat longer wavelengths, as shown by Figure 3.5. A value of around  $\beta_0 \sim 3$  represents a good compromise, and in particular yields a more accurate dispersion relation than SPH for all  $k$ . We also note that for certain numbers of neighbours, the SPH result is inaccurate at *all* wavelength; here the numerical soundspeed shows an offset relative to the expected sound speed, which is presumably a result of a bias in the density estimate for the background density.

### 3.5.4 Density noise and regularity in a settled particle distribution

In this subsection we want to examine the level of noise present in a relaxed region of gas of constant specific entropy, as it may arise somewhere within a larger, self-consistent simulation. To mimic this situation, we start from a distribution of points arranged on a Cartesian grid and impose a random Gaussian velocity field with dispersion  $\langle v^2 \rangle = 0.05 c_s^2$  and zero mean. The idea is that these velocity fluctuations break the initial grid symmetry and will then get damped away by the artificial viscosity, which is here set to a high value to speed up the process of settling to a new pressure equilibrium. Since we want to retain the initially equal values of the specific entropies per particle, we disable the entropy source term for the viscosity in this experiment. Once the new equilibrium for an irregular particle distribution is achieved, we can then examine the noise properties of this particle representation of a constant density, constant pressure gas.

For SPH with  $N = 16$  neighbours, we find that the particles settle into several domains in which the points are quite regularly distributed, based on visual inspection. The estimated density values  $\rho_i$  for the particles are *not* all equal though, instead they show a distribution with rms-scatter equal to  $\sim 1.4\%$ , and also a small *bias* relative to the expected value equal to the mean density  $\langle \rho \rangle = Nm/V$  of the full volume.

In contrast, the standard VPH approach creates a distribution in which the density values are essentially single-valued, and are all very close to  $\langle \rho \rangle$ . This means that the cells have all equal volume, and the residual pressure fluctuations, if any, are extremely small. However, the geometry of the Voronoi tessellation is quite irregular and features numerous cells with relatively large aspect ratios, or with points close to cell boundaries. This can be seen in Figure 3.6, where we show a plot of the final mesh for a test case carried out in 2D.

It is now interesting to repeat the test for the case when shape correction forces according to Section 3.3.2 are included. As desired, the final mesh becomes much more regular in this case, as seen in the corresponding example included in Figure 3.6. However, even in the final equilibrium state the correction forces do not necessarily completely vanish in this case. Instead, they are compensated by small residual pressure (and hence also density) fluctuations. This is demonstrated in the distribution functions of the density values for the three cases we considered, which we give in Figure 3.7. Here the shape correction case

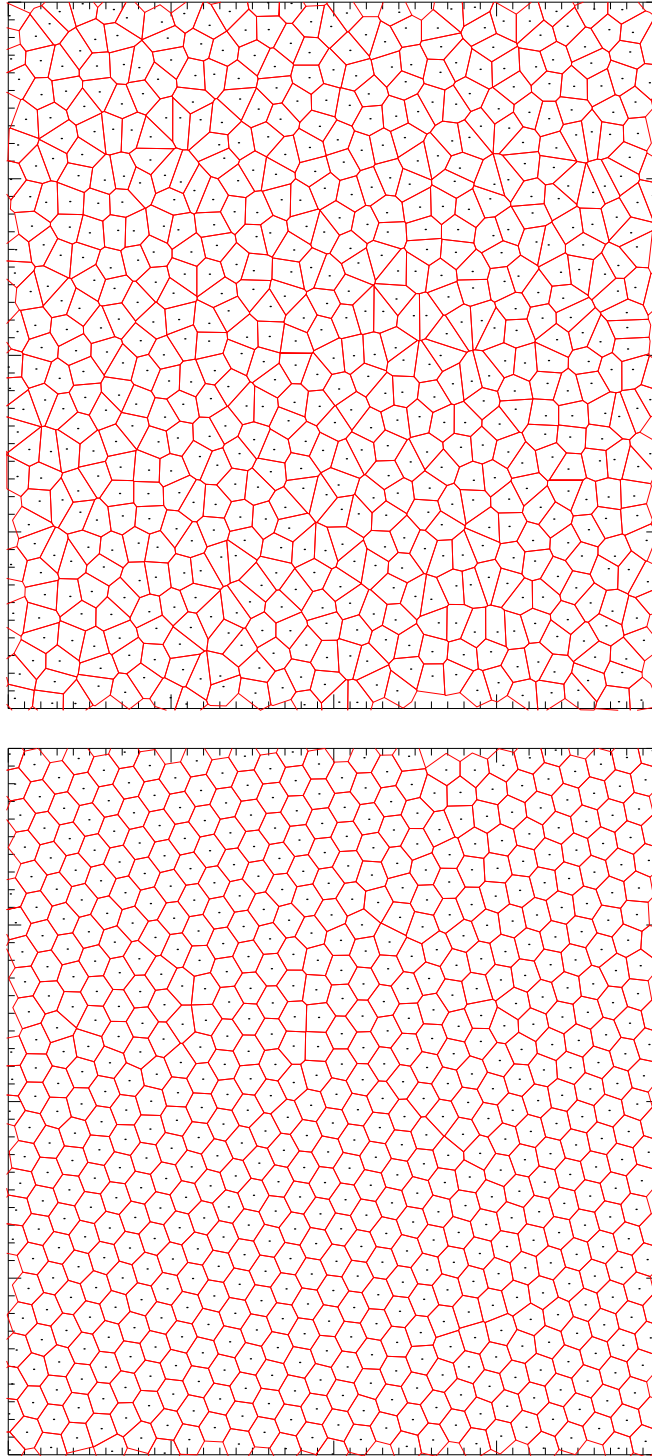


**Figure 3.6:** Final mesh geometry in VPH in a 2D settling test, carried out without (top) or with shape correction forces (bottom) based on  $\beta_0 = 1.0$  and  $\beta_1 = 0.01$ .

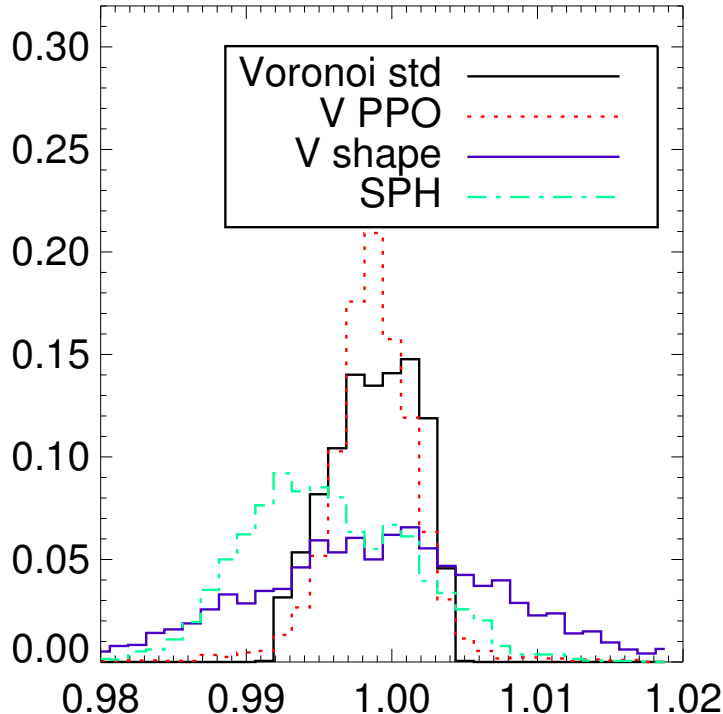


**Figure 3.7:** Density distribution functions of the particles in a settling test for constant entropy gas, carried out with different schemes. We compare SPH (red), ordinary VPH (black), the PPO version of VPH (blue), and VPH with shape correction forces based on  $\beta_0 = 1.0$  and  $\beta_1 = 0.01$  (in green). The distributions were measured at a time when the initial kinetic energy had decayed to  $E_{\text{kin}} \approx 0.001 E_{\text{kin}}(t = 0)$ .

yields a somewhat broader distribution, similar to SPH, but without showing a bias.

In Figure 3.8, we give a quantitative measure for the cell-regularity (here taken as the distribution function of the normalized displacement of points from the centres of their cells) of the final meshes in the Voronoi-based simulations. Even moderate values of the coefficients  $\beta_0$  and  $\beta_1$  can drastically improve the regularity of the particle distribution while introducing less noise in the density estimate than anyway present in SPH.

### 3.5.5 Point explosion

If energy is injected at a point into a cold gas at constant density, a spherical blast wave will develop. The Taylor-Sedov solution provides an analytic solution for this self-similar problem, which is a useful test involving very strong shocks. We have set-up this problem in 3D, using unit background density (represented with a Cartesian mesh),  $\gamma = 5/3$  and

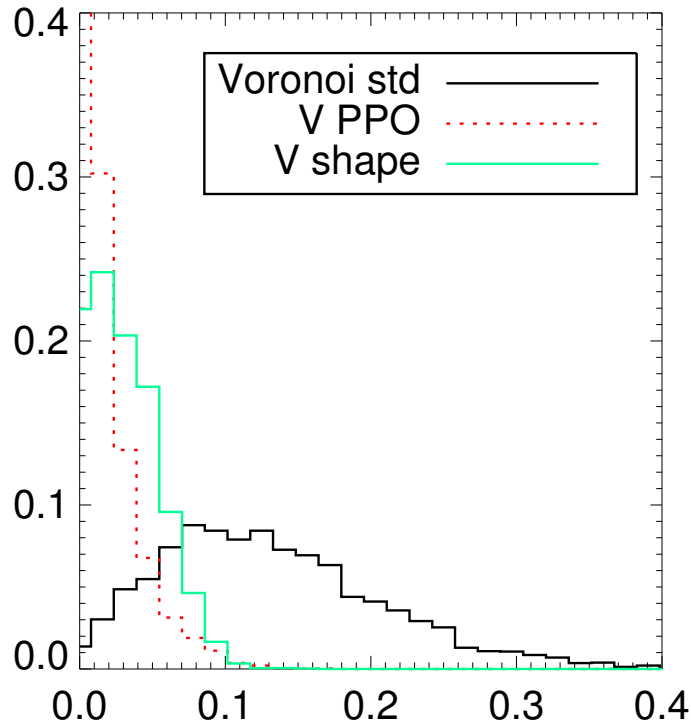


**Figure 3.8:** Cell-regularity of a noisy flow after relaxation. To characterize the regularity of the cells, we simply consider the distribution of the distance of the points to their cell’s centroids, in units of the 2D cell radius  $r = \sqrt{V/\pi}$ . The black histogram shows the distribution for the ordinary Voronoi scheme, blue shows the PPO version, and green lines give the result for the Voronoi with shape correction forces derived from the Lagrangian. The distributions were measured at a time when the initial kinetic energy had decayed to  $E_{\text{kin}} \approx 0.001E_{\text{kin}}(t = 0)$ .

vanishingly small initial specific entropy compared to the injected energy of  $E = 1$ . We inject the energy into the centre of the domain at time  $t = 0$ . To avoid that the evolution is strongly affected by the non-spherical geometry of the central Voronoi cell, we have spread out the energy with a Gaussian kernel with a radius of about 4 mean particle spacings.

We note that this set-up can be especially sensitive to the problem of particle crossing when a too low viscosity and individual timesteps are used. In the latter case, the local Courant timestep of particles outside of the explosion is initially very big. When the supersonic shock front arrives, such particles may then still live on a too large timestep, such that they are effectively overtaken by the shock, creating severe artifacts in the evolution of the shock front. We have addressed this in our test by imposing a low enough maximum timestep for all particles, but more sophisticated schemes to set the timesteps, which guarantee that it is reduced before the shock arrives, can of course be implemented in

principal (see Saitoh and Makino 2009; Springel 2009).

In Figure 3.9, we show the radial density profile at  $t = 0.04$  for different resolutions corresponding to  $2 \times 32$ ,  $2 \times 64$  and  $2 \times 128$  particles, and compare to the expected analytic solution. The expected solution is captured reasonably well, with a similar quality as in SPH codes, which is shown for comparison in the low-resolution case. The VPH result converges nicely to the analytic solution as the resolution is increased. In particular, the shock location is well reproduced, albeit with a small pre-shock increase of the density. When shape correction forces are added as described in Section 3.3.2, only negligible differences in the overall quality of the result are found, but the scatter around the azimuthally averaged solution is reduced. In Figure 3.10, we check the energy conservation in the blast wave problem, both for the VPH and SPH simulations at the  $32^3$  resolution. The energy error is negligibly small, as desired. The high-frequency oscillations in the total energy of the SPH run stem from the small but finite jumps of the SPH smoothing lengths from timestep to timestep, an effect that is absent in the VPH simulation.

### 3.5.6 Kelvin-Helmholtz instabilities

Kelvin-Helmholtz (KH) instabilities occur in regions of strong shear, which is especially common at contact discontinuities between two fluid phases. An initially small transverse perturbation along the interface becomes amplified and grows in linear theory according to  $\propto \exp(t/t_{\text{KH}})$ . After a few characteristic timescales

$$t_{\text{KH}} = \frac{\rho_1 + \rho_2}{2 k v \sqrt{\rho_1 \rho_2}} \quad (3.38)$$

an initially wave-like perturbation becomes large and non-linear, developing the typical KH-rolls. Here  $\rho_1$  and  $\rho_2$  are the densities of the two media,  $v$  is the velocity jump parallel to their common interface, and  $k = 2\pi/\lambda_{\text{pert}}$  is the wavenumber of the perturbation with wavelength  $\lambda_{\text{pert}}$ . For an ideal gas, all wavelengths are unstable, and the smallest wavelengths grow fastest.

The KH instability is especially important for the development of turbulence, and is thought to play a prominent role in stripping and mixing processes occurring during galaxy formation. Recently, a number of studies have pointed out that standard SPH has problems to correctly capture the KH instability when the initial conditions contain sharp density gradients (Agertz et al. 2007; Price 2008). In certain cases, the instability is suppressed completely and does simply not grow. This can in part be understood in terms of the surface tension effect present in SPH, as described earlier, because surface tension suppresses the growth of KH instabilities below a critical wavelength (Landau and Lifshitz 1966). Furthermore, the asymmetric particle density at the interface causes a rearrangement of the points in SPH, such that a ‘gap’ in the sampling appears that causes relatively large errors in the pressure forces at the interface (Agertz et al. 2007).

It is therefore very interesting to test how well the VPH approach does in this respect. Since VPH does not exhibit a surface tension effect, it offers the prospect of a better treatment of the KH instability. In Figure 3.11, we show results for a KH test calculation,

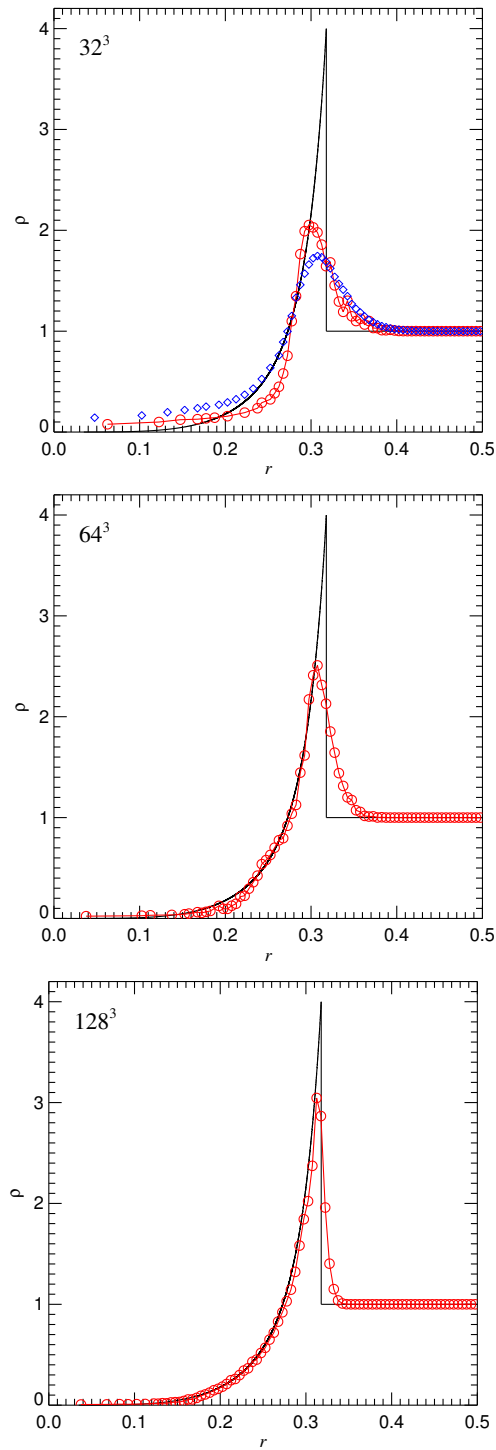


**Figure 3.9:** Sedov-Taylor point explosion problem, calculated in 3D with the basic VPH scheme. From top to bottom, we compare the radial density profile at  $t = 0.04$  with the analytical solution (solid line), calculated with  $32^3$ ,  $64^3$ , or  $128^3$  particles, as labeled. In the top panel, we also compare the VPH results (circles) with SPH (diamonds).

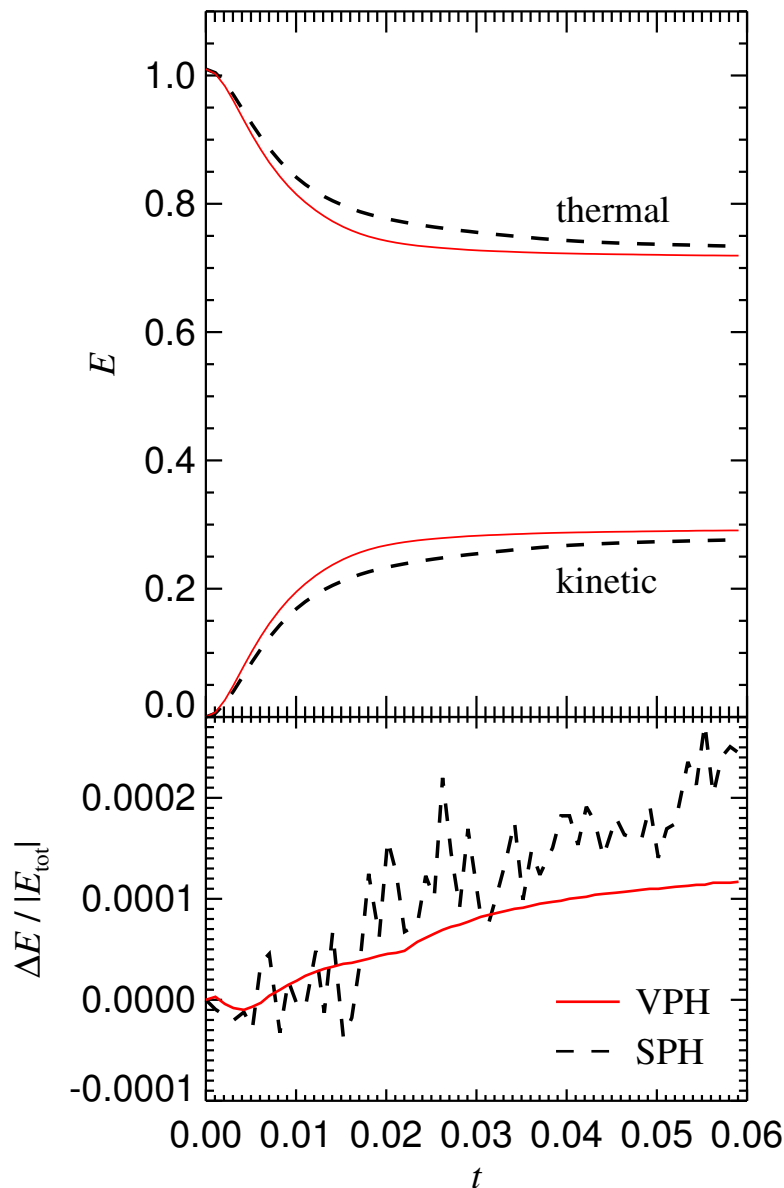


**Figure 3.10:** Time evolution of the thermal and kinetic energies in the Sedov-Taylor point explosion problem, simulated with SPH (black dashed line) and the Voronoi scheme with shape correction forces (red solid line). The bottom panel compares the total energy error in the two schemes.

carried out with different particle-based hydrodynamic schemes. Our two-dimensional initial conditions consist of  $\gamma = 5/3$  gas with density  $\rho_1 = 2$  in the stripe  $|y - 0.5| < 0.25$ , moving to the right with velocity  $v_1 = 0.5$ , and of gas with density  $\rho_2 = 1$  and velocity  $v_2 = -0.5$  in the region  $|y - 0.5| \geq 0.25$ . The pressure was initialized everywhere to  $P = 2.5$ , and a periodic domain of unit length on a side was used. In total 261760 points



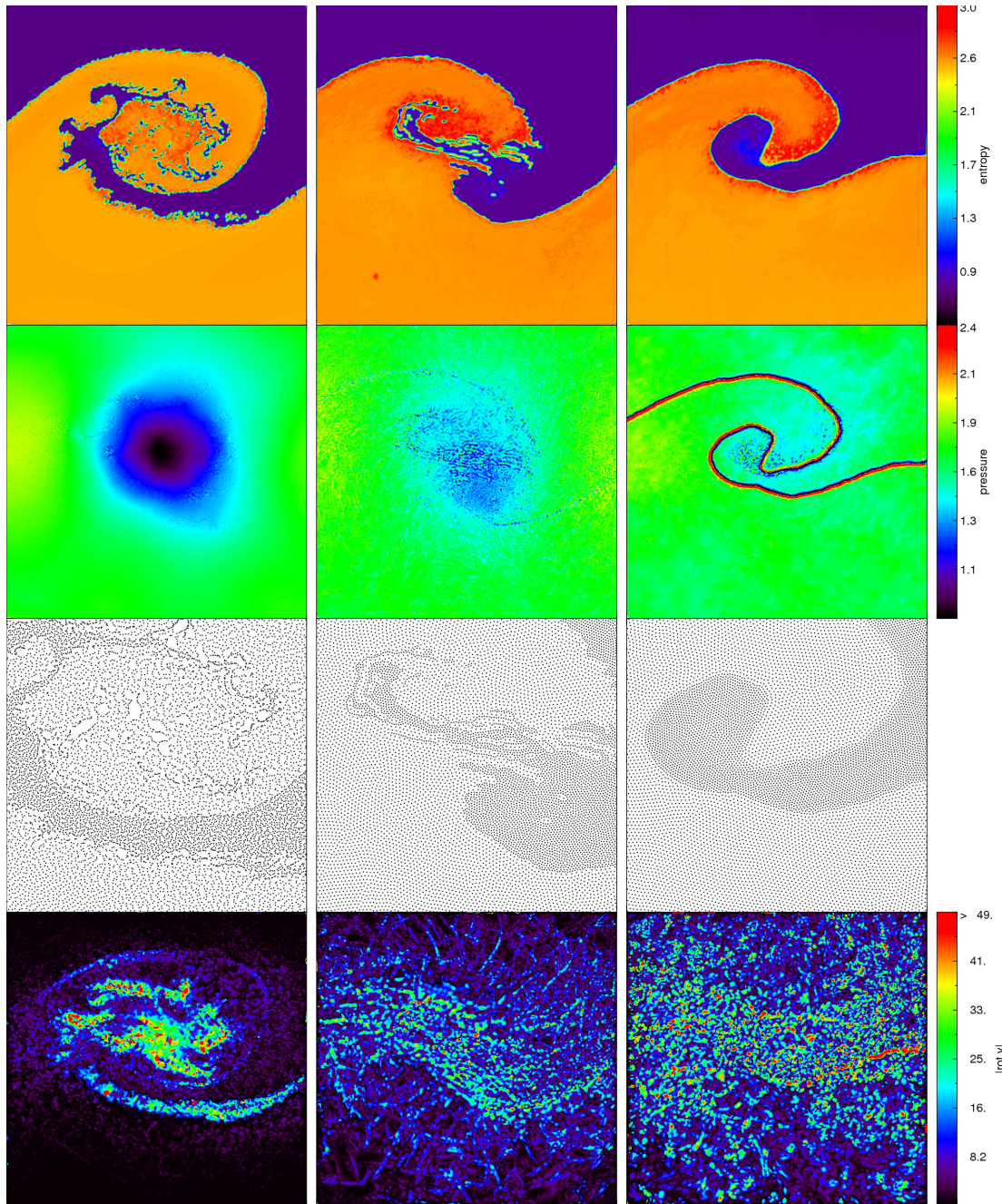


**Figure 3.11:** Simulations of the KH-instability with different particle-based methods. The left column shows the plain Voronoi scheme, the middle column Voronoi with PPO, and the right column SPH. From top to bottom, we show maps of specific entropy, maps of the pressure, the point distribution, and maps of the differential rotation  $\nabla \times \vec{v}$ . The maps show  $x = [0.18, 0.58]$ ,  $y = [0, 0.4]$  of the periodic simulation domain, while for clarity the particle distribution is shown only for  $x = [0.28, 0.48]$ ,  $y = [0.1, 0.3]$ .

sample the gas distribution, with a mean spacing of 0.0023 for the low-density gas, and 0.0017 for the high density gas. Hence the two phases were represented with approximately equal mass particles. Note that the initial discontinuity was imposed as a perfectly sharp jump in these initial conditions, following previous studies of this problem. We remark however that it is somewhat questionable whether such sharp jumps are not introducing an inconsistency with the basic premises of SPH calculations, which can only represent smoothed density fields. In order to seed an initial perturbation, we imposed a vertical perturbation on the  $y$ -positions of the form

$$\delta y(x) = a_0 \sin(4\pi x/L), \quad (3.39)$$

where  $L$  is the boxsize, and  $a_0 = 0.006$  is the amplitude of the initial perturbation.

The three columns of Figure 3.11 compare the results for the ordinary VPH scheme (left), the VPH method with the additional ordering viscosity of the PPO scheme (middle), and SPH (right), at time  $t = 1.2$ . From top to bottom, we show specific entropy maps, pressure maps, the particle distribution, and vorticity maps. All maps were here generated by linearly interpolating a Delaunay tessellation of the points, allowing to extend the points' properties as read from the simulation files to continuous fields. In addition to the maps, we show in Figure 3.12 the growth of the instability until time  $t = 1.2$ , quantified in terms of the amplitude of the seeded velocity mode as measured in the Fourier-transformed  $v_y$ -field.

We see right away that the VPH scheme captures the KH instability best. Its primary KH billow has evolved furthest, and it triggered the growth of smaller-scale secondary billows. In contrast, the SPH result shows only an anemic growth of the instability. In the SPH pressure map a strong pressure anomaly is visible at the interface. This surface effect effectively suppresses all small-scale KH-instabilities, and the two phases stay separate because the associated surface tension suppresses a breaking up of the interface. As a result, the instability cannot cascade down to smaller scales. The PPO scheme shown in the middle column lies literally in the middle in this respect. The growth of the primary KH mode is very similar to that found in the VPH scheme. However, the additional viscosity introduced in this scheme to produce highly regular cells substantially attenuates the growth of secondary small-scale KH instabilities. The same effect can be seen Figure 3.12 for the case with shape correction terms, whereas additional heat diffusion (according to Section 3.2.5) does not affect the growth rate of the excited mode in this simulation. We note however that the smaller growth depends on the strength of the additional ordering forces that are invoked. The result shown here was calculated with  $\kappa = 1$ , which we consider the maximum that one may ever want to use. For more reasonable smaller values, intermediate results that are close to that of the plain VPH scheme are obtained.

Interestingly, the vorticity  $\nabla \times \vec{v}$  in the ordinary VPH scheme is clearly largest overall, especially for the larger modes and in the central region of the primary KH billow. Here the rotation is so fast that the pressure shows a noticeable depression, which counteracts the centrifugal forces from the rotation with pressure gradients. Unfortunately, the ability of the pure Voronoi simulation to sustain vortices comes at the expense of a larger particle irregularity. As the enlargement with the particle distribution shows, the particles tend

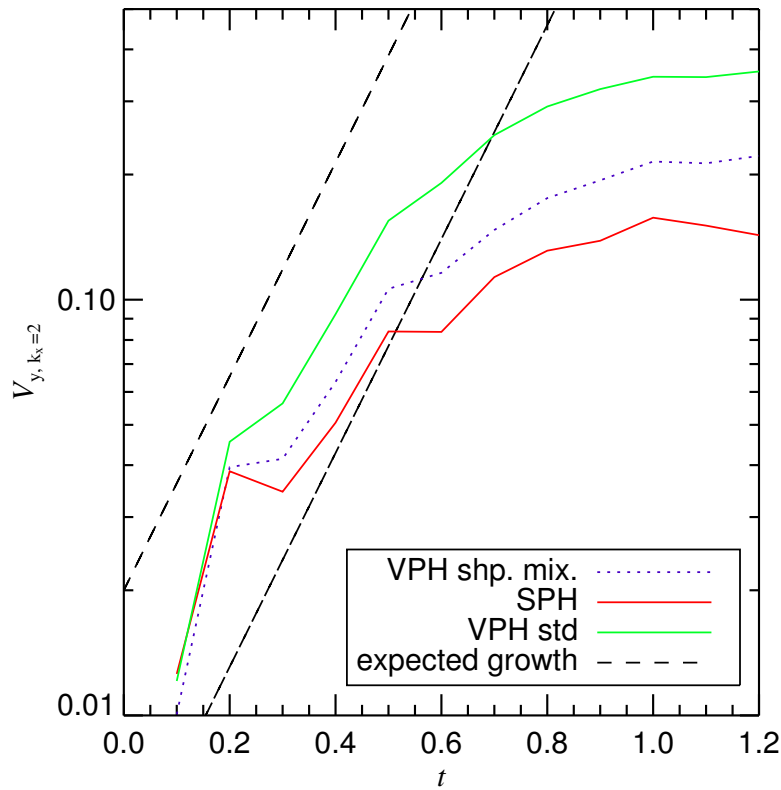


**Figure 3.12:** Growth rate of the KH-instability for the same initial conditions as in Figure 3.11. We show the amplitude of the seeded mode in the velocity field, measured by Fourier-transforming the  $v_y$  field. We give results for standard VPH (green), for the Voronoi scheme with additional shape correction forces and the prescription for mixing discussed in Section 3.2.5 (dotted blue), and for SPH (red). The dashed black lines indicate the slope expected for an exponential growth of the instability according to linear theory.

to form Voronoi cells with quite high aspect ratios, reducing the accuracy of the gradient estimates and requiring relatively large settings for the artificial viscosity to prevent inter-particle penetrations. In contrast, the PPO variant of the Voronoi scheme produces highly regular particle spacings, and in this respect resembles SPH. However, in this example calculation with  $\kappa = 1$ , the scheme then develops effectively a much higher intrinsic shear viscosity, which tends to transform the differential rotation into a rotation of numerous ordered domains. The shear of these domains shows up in the differential vorticity maps in a distributed fashion. Once the damping of the differential rotation gets too strong, the primary vortex is affected as well, as seen in the reduction of the central pressure gradient in the PPO scheme.

Finally, we test the shape correction forces discussed in Section 3.3.2, and our scheme for the treatment of subresolution mixing introduced in Section 3.2.5 with the same initial

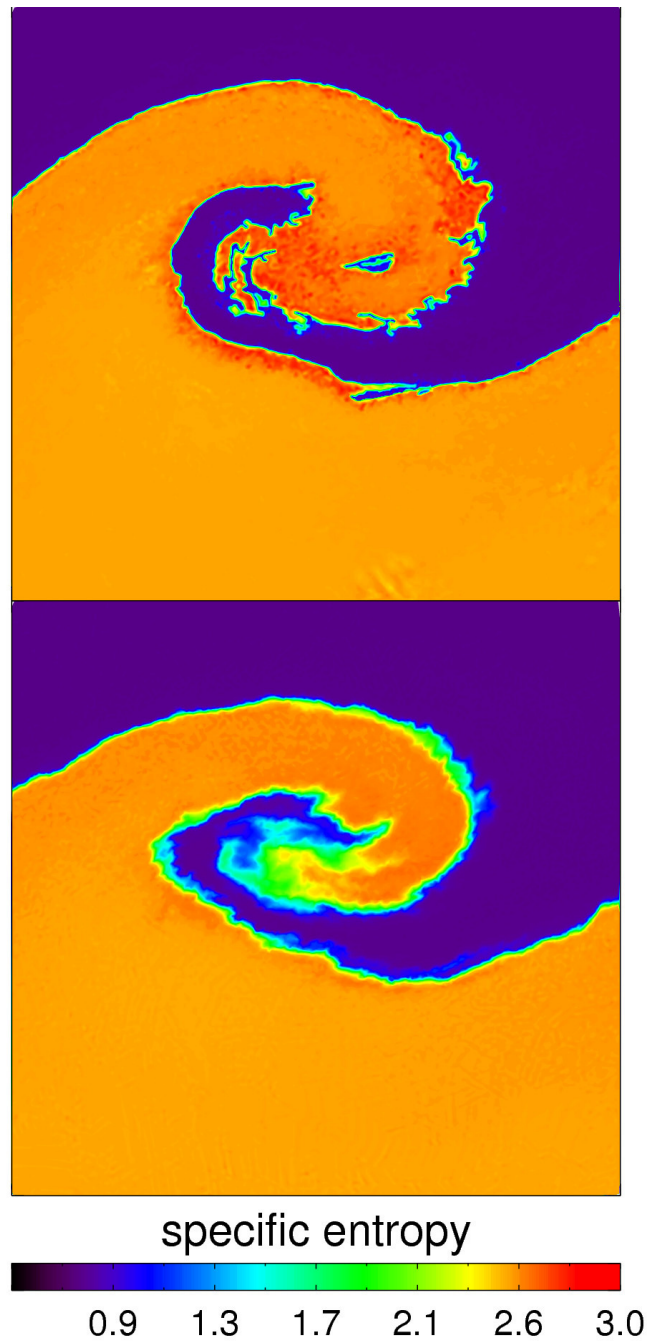


**Figure 3.13:** KH-instability test simulated with the Voronoi scheme with additional shape correction forces, based on the same initial conditions as in Figure 3.11 and again at time  $t = 1.2$ . The maps show the entropy distribution without (top) and with (bottom) additional heat diffusion terms to model subresolution mixing, as described in Section 3.2.5.

conditions. We show in Figure 3.13 the resulting entropy maps of two further calculations of the KH instability test. In both panels, we show runs of the VPH scheme that make use of the shape correction forces derived from the Lagrangian, with  $\beta_0 = 1.2$  and  $\beta_1 = 0.1$ . In the bottom panel, we have in addition activated the artificial heat conduction due to local shear with  $\chi = 0.25$ , which models mixing of the fluids at the scale of the resolution. The two variants are qualitatively similar, but the artificial heat conduction has clearly washed out the sharp discontinuity in the entropy at the fluid interface. This resembles more closely the results of mesh-based finite-volume hydro codes. Compared to the results of pure VPH in Figure 3.11, we see that the scheme with shape correction forces has also an effectively enlarged viscosity, quite similar to the PPO approach. Overall, it is clear that even without a subresolution mixing model the Voronoi based particle hydrodynamics does significantly better in the KH test than standard SPH.

### 3.5.7 The ‘blob test’: mass loss of a gas cloud in a supersonic wind

A challenging test problem for hydrodynamical codes has been proposed by Agertz et al. (2007). The setup consists of an overdense spherical cloud in pressure equilibrium with the surrounding hot medium. This background gas is given a large velocity, so that the cloud feels it as a supersonic head wind. The test is motivated by astrophysical situations such as the stripping of gas out of the halos of galaxies as they fall into larger systems. It is a three-dimensional problem that involves many different non-linear hydrodynamical phenomena, including shocks, Kelvin-Helmholtz instabilities, mixing, and the generation of turbulence. Because of this complexity, an analytical solution for the problem is not known. The general expectation is that the wind will compress the cloud, accelerate it, and strip some of its gas by developing fluid instabilities as it streams past the cloud.

Interestingly, in the test calculations of Agertz et al. (2007), substantial differences were found in the mass loss rates of the cloud when calculated with Eulerian mesh codes and with SPH. Whereas the mesh codes led to an eventual complete destruction of the cloud, the mass loss rate was in general smaller in SPH, such that some cloud material still remained once the partially destroyed cloud was accelerated to the wind speed and the mass loss stopped. Given these qualitatively different outcomes, it is interesting to test how the VPH scheme performs on this problem.

We used the same initial conditions as employed by Agertz et al. (2007), in the version with  $10^6$  particles. The setup consists of a periodic box with extension  $[0, 2000] \times [0, 2000] \times [0, 8000]$  kpc. The background ‘wind’ gas has density  $\rho_{\text{wind}} = 4.74 \times 10^{-34} \text{ g cm}^{-3}$ , temperature  $T_{\text{wind}} = 10^7 \text{ K}$ , and a velocity  $v_{\text{wind}} = (0, 0, 1000) \text{ km s}^{-1}$ . The cloud has a radius  $R_{\text{cloud}} = 197 \text{ kpc}$ , and is placed initially at  $\vec{r}_{\text{cloud}} = (1000, 1000, 1000) \text{ kpc}$ . Its density is 10 times higher than the background,  $\rho_{\text{cloud}} = 10 \rho_{\text{wind}}$ , while at the same time being 10 times colder,  $T_{\text{cloud}} = 10^6 \text{ K}$ . This yields a sound speed of  $c_{\text{wind}} = 371 \text{ km s}^{-1}$  for the wind, and an expected characteristic timescale of order  $\tau_{\text{KH}} \simeq 2 \text{ Gyr}$  for the development of large KH instabilities in the shear-flow around the cloud.



In Figure 3.14, we show the time evolution of density slices through the central plane of the simulation box, calculated with our new Voronoi scheme. In agreement with both grid-based and SPH codes, a bow shock is produced ahead of the cloud. The cloud gets compressed and accelerated under the ram pressure of the wind, and the wind that streams past the deformed and slowly accelerating cloud induces Kelvin-Helmholtz instabilities at its surface which strip material and produce a turbulent wake. At the stagnation point of the flow in front of the cloud, the pressure eventually breaks through along the axis of symmetry. The resulting “smoke ring” is then still exposed to Kelvin-Helmholtz induced turbulence while it is being accelerated to the velocity of the background stream. Due to the periodic boundary conditions we note that the bow shock extends past the domain boundary and then back inwards again from the other side, reaching the cloud at about  $t \approx 3 \tau_{\text{KH}}$ . This leads to a recompression of the remainder of the cloud which can temporarily raise the number of particles that are still counted as cloud members.

The mass loss as a function of time is displayed in Figure 3.15, for different particle-based hydrodynamical schemes. We follow Agertz et al. (2007) and consider a particle to be still part of the cloud when its density is still larger than  $\rho > 0.64 \rho_{\text{cloud}}$ , and its temperature fulfills  $T < 0.9 T_{\text{wind}}$ . We show results for four different calculations in total. The standard VPH scheme is shown in blue. Interestingly, it leads to a complete destruction of the cloud at time  $t \approx 3 \tau_{\text{KH}}$ , a result which is actually surprisingly close to the high-resolution mesh-based calculations reported in Agertz et al. (2007). On the other hand, the two SPH-based results (shown in red and black) calculated with the GADGET2 code do not result in a destruction of the cloud. Instead at time  $t = 5 \tau_{\text{KH}}$ , still about half the mass of the original cloud can be characterized as residual cloud material. This is even slightly larger than what was reported by Agertz et al. (2007) for the GASOLINE code. We have however found that the formulation and the strength of the artificial viscosity can influence this result significantly. Also, we confirmed that integration of the entropy as independent thermodynamic variable (which is the default in GADGET2) results in less stripped material than when the thermal energy is integrated as done in GASOLINE. This is however probably largely a result of the particular initial conditions used here; the contact discontinuity in the ICs of Agertz et al. (2007), that we employ here, has been relaxed using the traditional SPH formulation of GASOLINE, creating a pressure blip. When this is then used to initialize the entropies integrated in GADGET2, a spurious entropy blip is created that further amplifies the initial sampling ‘gap’.

When strong shape correction forces are introduced into the VPH formalism, we find an intermediate result between plain VPH and SPH. In this case, a small 10% remnant of the cloud remains at time  $t = 5 \tau_{\text{KH}}$ . This is consistent with our earlier findings for the KH instabilities. While standard SPH can be expected to suppress the KH-instabilities significantly at the cloud interface, it tends to underestimate the rate of stripping. Our new VPH method does not show this problem, but if viscous forces are introduced that guarantee very regular mean particle separations, some small-scale suppression of fluid instabilities can be reintroduced.

We finally note that the use of a time variable viscosity as presently implemented in our code has not changed the mass-loss curves significantly. The reason is that the relevant

particle viscosities are pushed to a large value as they pass through the bow shock, and stay at large values in the complicated flow around the cloud surface. Only at late times the mass loss tends to become faster as a result of the effectively lower viscosity.

### 3.5.8 Gravitational collapse of a gas sphere

Finally, we consider a three-dimensional problem with self-gravity, the so-called ‘Evrard-collapse’ (Evrard 1988). It consists of an initially cold gas cloud, with a spherically symmetric density profile of  $\rho(r) \propto 1/r$ . The total mass, outer radius and gravitational constant are all set to unity,  $M = R = G = 1$ , and the initial thermal energy per unit mass is set to  $u = 0.05$ . In this configuration the sphere is significantly underpressurized. It hence collapses essentially in free-fall, until it bounces back at the centre, with a strong shock running through the infalling material. The sphere then settles into a new virial equilibrium. As this problem involves large conversions of potential gravitational energy into kinetic energy and thermal energy (and back), as well as strong shocks, it is a challenging and useful test for hydrodynamic codes that are applied to structure formation problems. For this reason, it has been widely used as a test for a number of SPH codes (e.g. Evrard 1988; Hernquist and Katz 1989; Steinmetz and Mueller 1993; Dave et al. 1997; Springel et al. 2001; Wadsley et al. 2004; Springel 2005b).

For our test we create a realization of the sphere by stretching a Cartesian grid appropriately, such that the desired initial density profile is obtained. Because the Voronoi scheme needs to tessellate a well-defined total volume, we cannot impose vacuum boundaries in the same way as in SPH. Instead, we embed the sphere in a box and use a background grid of particles with a rapidly falling density profile outside of the sphere, such that the total mass in the background can still be ignored in the evolution of the system. We calculate the gravity with the same tree algorithm used in the GADGET2 code, simply using the N-body approach with the masses and positions of the VPH particles. It turns out however that particles sometimes tend to pair up under their pairwise gravitational forces in the plain VPH scheme. This is related to the same defect discussed in the context of Figure 3.2. If two particles are very close to a Voronoi wall, they can be moved still closer together without increasing the hydrodynamic pressure force, so that a residual gravitational attraction (if not damped out by the gravitational softening) can move the particles very close together, with problematic consequences for the stability and accuracy of the scheme. A time-dependent gravitational softening (Price and Monaghan 2007), where the softening is somehow tied to the size of the cell associated with a particle, may ease the problem, but is unlikely to cure it completely. However, the shape correction forces we introduced in Section 3.3.2 can nicely solve this problem. This effect is illustrated in Figure 3.16, where we show the central mesh geometry for a two-dimensional version of the Evrard collapse problem. In the following we consider therefore a calculation of the 3D Evrard collapse with our usual choice of  $\beta_0 = 1.2$  and  $\beta_1 = 0.1$ .

In Figure 3.17, we show radial profiles of gas density, radial velocity and entropy for the Evrard collapse at time  $t = 0.8$ , calculated with 24464 particles inside the initial sphere. We compare the VPH result (shown by blue circles) to results obtained with SPH (red

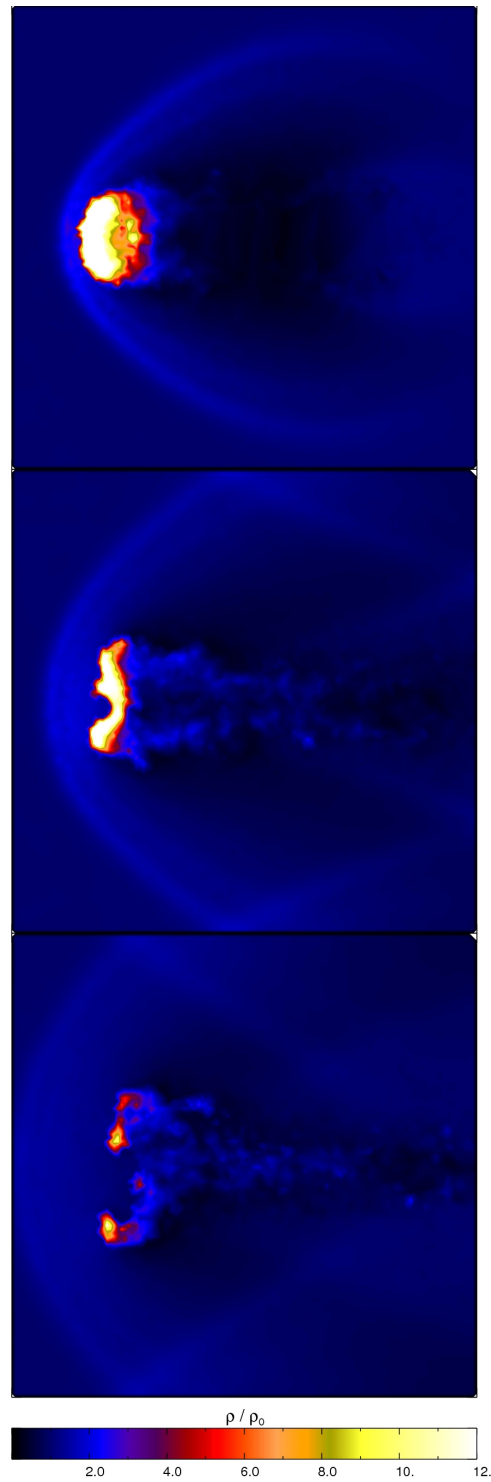


**Figure 3.14:** Time evolution of the density for a gas cloud in a supersonic wind. From top to bottom, we show density maps normalized to the initial wind density at times  $t = 0.75 \tau_{KH}$ ,  $t = 1.5 \tau_{KH}$ , and  $t = 2.25 \tau_{KH}$  in the central plane of the simulation box. Here the standard Voronoi scheme with  $10^6$  particles was used.



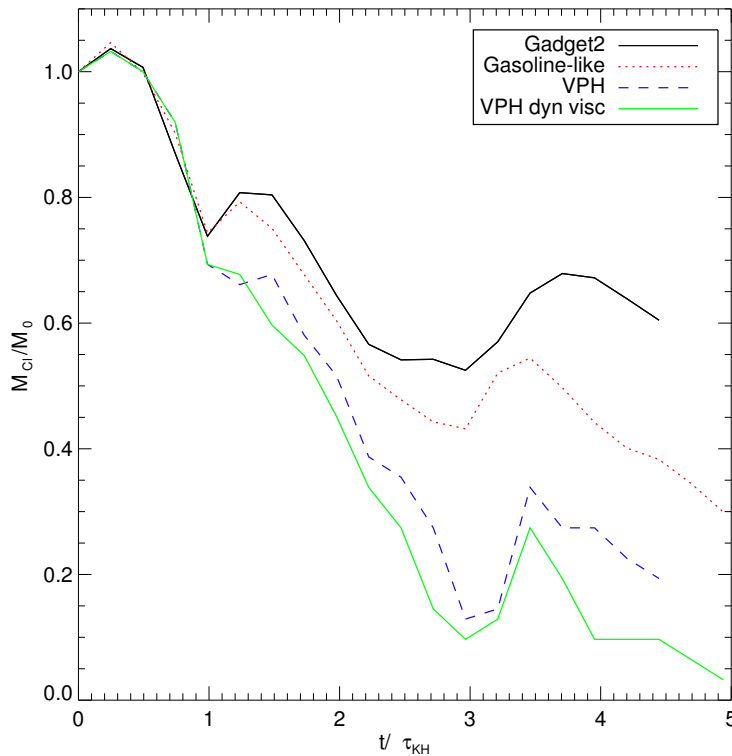


**Figure 3.15:** Mass loss of a gas cloud in a supersonic wind (the ‘blob test’), simulated with  $10^6$  particles and different hydrodynamical schemes. We show the remaining mass associated with the cloud (particles that fulfill  $\rho > 0.64\rho_{\text{cloud}}$  and  $T < 0.9T_{\text{wind}}$ ) as a function of time (in units of  $\tau_{\text{KH}}$ ) for different hydrodynamical schemes. The different colors refer to the SPH codes GADGET2 (black), modified GADGET2 with an GASOLINE-like integration scheme (red), standard VPH (green), VPH with dynamic viscosity (see Equation 3.23) (light blue) and VPH with heat diffusion according to Section 3.2.5 (dark blue)

diamonds), and compare these to results of a 1D high-resolution PPM calculation of the problem (solid black line) provided to us by Steinmetz and Mueller (1993). We find that the collapse is essentially equally well described with VPH as with SPH, with a slight advantage for VPH, which more accurately resolves the central density and captures the shock more sharply. However, these differences lie well in the range of changes one obtains for different viscosity prescriptions, and therefore do not seem to be particularly significant. We also note that the extra viscous forces needed to maintain a regular particle distribution in VPH do not introduce any unphysical features in the solution. In particular, the radial profile of the specific entropy shows no signs of extra cooling or heating.

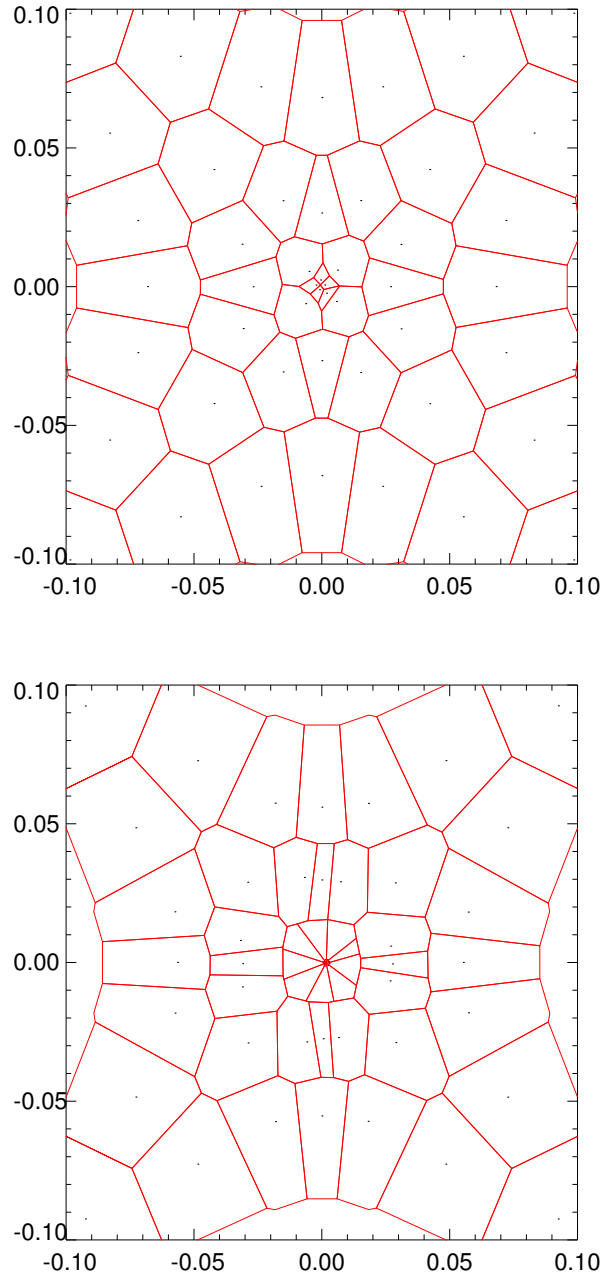


**Figure 3.16:** Cell regularity without (bottom) and with cell regularization forces (top) in a simulation of a sphere of gas collapsing under self-gravity (Evrard collapse problem). In the bottom panel, the group of points clusters together close to the origin under their mutual gravitational attraction, producing a quite irregular mesh there. This effect is prevented when additional shape correction forces are invoked, as shown in the top panel.

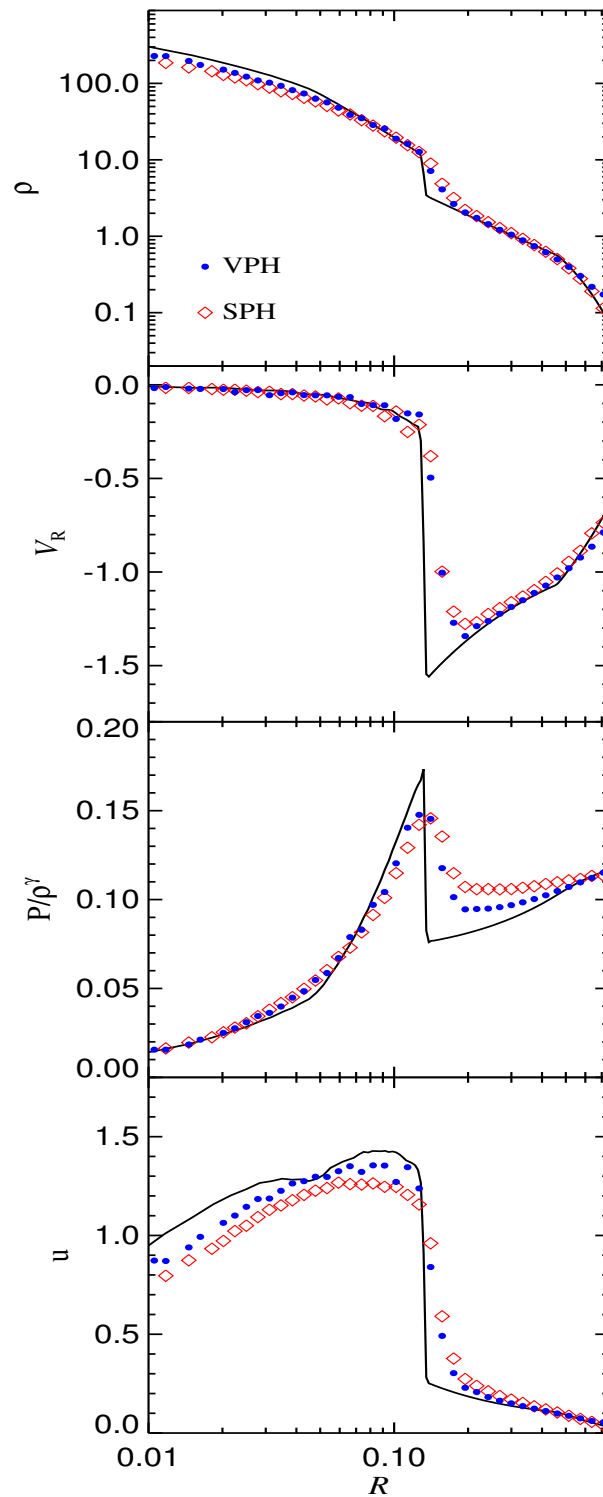


**Figure 3.17:** Evrard collapse at time  $t = 0.8$  simulated with SPH (red diamonds) and the Voronoi scheme with shape correction forces (blue circles). The black line shows the results of a 1D high-resolution PPM calculation of the problem provided to us by Steinmetz and Mueller (1993). From top to bottom, we show radially averaged profiles of gas density, radial gas velocity, specific entropy, and internal energy.

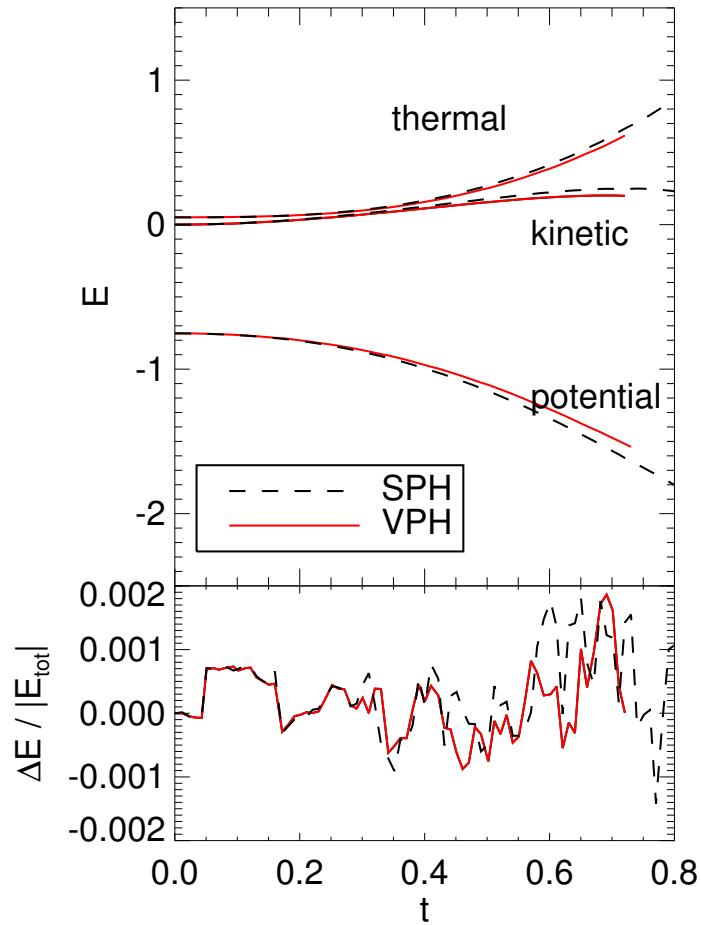


**Figure 3.18:** Energy evolution for the “Evrard collapse” simulated with SPH (black dashed line) and the Voronoi scheme with shape correction forces (red solid line). The small fluctuations in the total energy arise primarily as a result of the finite accuracy of the tree code used to calculate self-gravity, and are of similar magnitude for both cases.

### 3.6 Conclusions

We have discussed a new fluid particle model where the density is estimated with the Voronoi tessellation generated by the particle positions. Unlike in SPH, there is an auxiliary mesh, which adds complexity to the scheme. However, the use of this fully adaptive mesh offers a number of advantages. It offers higher resolution for a given number of particles, since fluid features are not inherently smoothed as in SPH. In fact, the tessellation techniques are probably close to an optimum exploitation of the density information contained in the particle distribution (Pelupessy et al. 2003). When even higher resolution is needed the method could be extended by an adaptive particle refinement or splitting technique, for example similar as suggested in (Springel 2009).

As a result, contact discontinuities can be resolved with one cell, and surface tension

effects present in standard SPH across contacts with large density jumps are eliminated. This has further implications for the growth rate of fluid instabilities in inviscid gases. Furthermore, the free parameters in the density estimate of SPH, involving both the number of neighbours as well as the kernel shape, are eliminated, which can be viewed as a good thing since the optimum values for them are not known, and incorrect choices can invoke the well-known clumping instability in SPH.

One somewhat problematic aspect of Voronoi-based particle hydrodynamics is that the noise in the scheme is quite sensitive to the level of mesh regularity. Flows with a lot of shear can readily develop Voronoi meshes with points that lie close to the surfaces of their Voronoi cells. In this case the noise in the gradient estimates increases, and, more importantly, it becomes difficult to safely prevent particle interpenetration, since closeness to a wall of the tessellation always implies that there is a second point on the other side of the wall which is also close, i.e. in other words, that a close particle pair is present.

Higher order density estimates might solve this problem, but they would have to be introduced already into the Lagrangian, leading to much more complicated equations of motion that may be intractable. We therefore explored two different approaches for keeping the mesh relatively regular. One is simply based on trying to formulate additional artificial viscosity terms such that the viscosity tries to make cells ‘rounder’. Whereas this shows some success, it does not succeed in all situations, particularly in strong shear flows where the artificial viscosity needs to be very low. A more radical approach also explored is to add correction terms to the underlying fluid Lagrangian with the aim to penalize strong deviations from regular mesh geometries. Our goal was to impose small, non-dissipative correction forces that maintain a proper mesh geometry. Thanks to the Lagrangian formulation, the required form of the correction forces to retain fully conservative behaviour can readily be derived, and the fluid motion under these forces shows the desired properties. However, if the correction terms are too large, one risks deviations from the proper hydrodynamic solution. Further experimentation will be required to identify the optimum setting of these parameters.

The Voronoi-based fluid particle approach can be relatively seamlessly integrated into an existing SPH code, provided a tessellation engine can be added in an appropriate fashion. Other aspects of the physics (in particular self-gravity, an additional collisionless component, radiative cooling, star formation, and feedback processes) can be treated in essentially identical ways as in SPH. This makes it possible to readily apply Voronoi particle hydrodynamics to problems of interest in cosmological structure formation. In general, our first results suggest that VPH is superior to SPH, albeit at much increased complexity. However, it is at present still unclear whether it is competitive with finite volume hydrodynamics carried out on a similarly constructed Voronoi mesh, as realized in the AREPO code (Springel 2009). To elucidate this point further, we are in the process of carrying out galaxy collision simulations as well as cosmological structure formation simulations with our new technique and will report the results in forthcoming work.



# Chapter 4

## Gas stripping and mixing in galaxy clusters

*S. Hess and V. Springel, 2011, MNRAS, to be submitted*

### **Abstract**

The ambient hot intrahalo gas in clusters of galaxies is constantly fed and stirred by infalling galaxies, a process that can be studied in detail with cosmological hydrodynamical simulations. However, different numerical methods yield discrepant predictions for some of the crucial hydrodynamical processes, leading for example to different entropy profiles in clusters of galaxies. In particular, the widely used Lagrangian smoothed particle hydrodynamics (SPH) scheme is suspected to strongly damp fluid instabilities and turbulence, which are both crucial to establish the thermodynamic structure of clusters. In this study, we test to which extent our recently developed Voronoi particle hydrodynamics (VPH) scheme yields different results for the stripping of gas out of infalling galaxies, and for the bulk gas properties of cluster. We consider both the evolution of isolated galaxy models that are exposed to a cluster wind or are dropped into cluster models, as well as non-radiative cosmological simulations of cluster formation. We also compare our particle-based method with results obtained with a fundamentally different discretization approach as implemented in the moving-mesh code AREPO. We find that VPH leads to noticeably faster stripping of gas out of galaxies than SPH, and to elevated core entropies. Both of these findings are qualitatively in better agreement with the mesh-code than with SPH, confirming that VPH is an attractive alternative to SPH, even though it exhibits a comparable level of particle noise.

### **4.1 Introduction**

In the hierarchical structure formation model, interactions or mergers of galaxies with other galaxies are common processes, and depending on the environment, a diverse set of physical processes can become important. For example, when a galaxy falls into a cluster of galaxies, gravity may also affect its integrity through gravitational tidal forces. The

closer the galaxy gets to the cluster the more it is exposed to the hot intra-cluster medium (ICM). This is experienced as a headwind by the galaxy that compresses its own gas, and may lead to the formation of a bow shock in front of the galaxy if it supersonically plows through the ICM.

Whereas the gas at the front of the galaxy is primarily compressed by ram pressure in this situation, the sides are exposed to strong shear flows which may trigger fluid instabilities, leading to stripping and mixing of the gas with the ICM. This in turn crucially determines how rapidly star formation is turned off in an infalling galaxy, and how metals are mixed into the group or cluster ICM. The hydrodynamical interaction processes between galaxies and groups/clusters may thus influence important observational effects, such as the density morphology relation, or the existence of a tight red cluster galaxy sequence. However, modeling these processes reliably is a considerable challenge, as direct hydrodynamic simulations of the relevant processes are very difficult due to the large dynamic range, and the uncertainties associated with the modeling of star formation and feedback processes. Furthermore, it is not clear whether the hydrodynamical techniques presently in use are strongly affected by systematic errors in this regime. Indeed, previous studies of galaxy-cluster interactions with different numerical schemes disagreed strongly about how fast a galaxy loses its gas to the cluster. For example, a grid-based simulation of Quilis et al. (2000) predicted a much higher stripping rate than SPH-based work by Abadi et al. (1999).

In this paper, we concentrate on the numerical aspects of the stripping of a galaxy's gas as it interacts with the ICM. Agertz et al. (2007) has recently shown that the popular smoothed particle hydrodynamics (SPH) technique has problems to properly account for fluid instabilities, prompting significant concerns about a possible unphysical suppression of stripping processes. In a recent study (Heß and Springel 2010) we have therefore proposed a new 'Voronoi particle hydrodynamics' (VPH) method that improves on the widely used SPH technique (Lucy 1977b; Gingold and Monaghan 1977; Larson 1978) in several respects. By employing a Voronoi tessellation for the local density estimate, a consistent decomposition of the simulation volume is achieved, contact discontinuities can be resolved much more sharply, and a 'surface tension' effect across them is avoided. Our preliminary tests of VPH based on the 'blob-test' of Agertz et al. (2007) already suggested that stripping is more efficient in VPH compared with SPH. Here we shall investigate this in more detail using more realistic set-ups that mimic galaxy evolution processes. In addition to the two particle-based Lagrangian schemes for hydrodynamics, SPH and VPH, we will also carry out comparison simulations with the moving-mesh code AREPO (Springel 2010a). Whereas AREPO uses a Voronoi tessellation as well, this code employs an entirely different methodology for fluid dynamics, based on a finite volume Godunov scheme that calculates hydrodynamical fluxes with a Riemann solver across mesh boundaries. The comparison of this diverse set of three numerical methods is useful to understand and quantify the systematic uncertainties of the different methods.

Another interesting aspect besides the stripping is the generation of turbulence by galaxies infalling into clusters. Numerical simulations (Dolag et al. 2005; Vazza et al. 2006; Iapichino and Niemeyer 2008; Dolag et al. 2009) indicate that turbulence can be generated



in the wake of an infalling galaxy. This interesting phenomenon may play an important role in determining the dynamics of the cluster gas and could in principle be detected through X-ray observations of the broadening of sharp metal lines (Sunyaev et al. 2003). We will hence briefly investigate the degree to which VPH improves on SPH’s ability to represent fluid turbulence in the context of galaxy-ICM interactions.

In our tests simulations, we ideally want to investigate as realistic conditions as possible, including a full treatment of gravity and dark matter, as well as star formation and cooling. This in principle calls for simulations in which a well-resolved galaxy model is dropped into an equally well represented cluster of galaxies. Because the substantial computational cost of such a set-up severely limits the resolution that can be achieved, we base part of our study on a number of more idealized simulations, for example by placing galaxy models into a ‘wind tunnel’ that mimics the impinging flow of gas onto a galaxy in orbit in a cluster. Finally, we also carry out cosmological simulations of the formation of the ‘Santa Barbara cluster’ (Frenk et al. 1999), primarily to study how well VPH performs in non-radiative cosmological simulations of cluster formation compared to the other techniques. Already in past studies, the Santa Barbara cluster comparison project has led to important insights into how numerical effects impact the thermodynamic structure of simulated clusters, and for this test problem, there is already a considerable body of results in the literature.

This chapter is structured as follows. In Section 4.2, we introduce the numerical methods we will use in our numerical comparison study. In Section 4.3, we check how well the different numerical schemes represent the evolution of an isolated galaxy, and whether there are already significant differences at this level. We then consider in Section 4.4 wind-tunnel experiments in which we expose the isolated galaxy models to a supersonic wind, allowing a detailed examination of the stripping process. In Section 4.5, we follow up on these experiments by studying the behaviour of a galaxy model that falls into an isolated spherical cluster, comparing the VPH results with those obtained with SPH and AREPO. Finally, in Section 4.6, we investigate the performance of VPH in cosmological simulations of cluster formation, using re-simulations of rich clusters identified in the Millennium Simulation as well as the Santa Barbara cluster initial conditions. We summarize our conclusions in Section 4.7.

## 4.2 Methodology

We begin by introducing the different codes and computational methods we use in this study. In the interests of brevity, we shall only describe the most important characteristics of the codes; full details can be found elsewhere (Springel 2005a; Heß and Springel 2010; Springel 2010a).

### 4.2.1 Smoothed particle hydrodynamics

Smoothed particle hydrodynamics (SPH) is a particle based approach to fluid dynamics that has seen widespread use in astronomy since it was first introduced more than three

decades ago (Lucy 1977b; Gingold and Monaghan 1977). SPH discretizes the mass of the fluid in terms of particles, whose dynamics is governed by a fluid Lagrangian of the form

$$L = \sum_i \left[ \frac{1}{2} m_i \vec{v}_i^2 - m_i u_i(\rho_i, s_i) \right]. \quad (4.1)$$

Here  $u_i$  describes the thermal energy per unit mass, which for an ideal gas depends only on density  $\rho_i$  and specific entropy  $s_i$ . An adaptive, spherically symmetric smoothing kernel is employed to estimate the density based on the spatial distribution of an approximately fixed number of nearest neighbours. The Lagrangian in Eq. (4.1) then uniquely determines the equations of motion in a form that simultaneously conserves energy and entropy (Springel and Hernquist 2002; Price and Monaghan 2007; Springel 2010b). However, an artificial viscosity needs to be added to allow for dissipative shock capturing and to produce a damping of postshock oscillations.

Among the primary advantages of SPH are its very good conservation properties, the manifest Galilean invariance at the discretized level of the equations, and the absence of preferred spatial directions. However, it has recently become clear that contact discontinuities, in particular, are challenging for the method. For example, they are associated with a spurious surface tension effect in SPH (Springel 2010b), and fluid instabilities such as the Kelvin-Helmholtz instability are suppressed across them (Agertz et al. 2007).

### 4.2.2 Voronoi particle hydrodynamics

Because of the accuracy problems of SPH in certain situations, we have recently developed another particle-based hydrodynamic method that differs from SPH in important ways, while still sharing a number of similarities. In this ‘Voronoi Particle Hydrodynamics’ (VPH) method (Heß and Springel 2010), the fluid is also discretized in terms of mass elements  $m_i$ , and the same fluid Lagrangian as in Eq. (4.1) is used. However, the kernel estimation technique of SPH is replaced by a very different approach to calculate the gas density. This is done by constructing a Voronoi tessellation for the point set, in which to each of the particles the volume of all the space which is closer to this point than to any other point is assigned. The density can then be obtained as the particle mass divided by the volume of the associated Voronoi cell. We note that such a tessellation technique allows a close to optimum exploitation of the density information contained in the particle distribution (Pelupessy et al. 2003), and in particular, very sharp discontinuities can be resolved over the distance of a single cell.

With the density computed, and given specified entropies  $s_i$  for every particle, we can use the ideal gas Lagrangian to derive unique equations of motion for VPH. The key quantity that is needed in doing this is the derivative of the particle volume with respect to the coordinates of the surrounding particles, but thanks to the mathematical properties of the Voronoi tessellation, the corresponding geometric factors can be computed relatively easily (Serrano and Español 2001; Heß and Springel 2010) and have a clear geometric meaning. For example, the primary force between two VPH particles is their pressure

difference times the area of their common tessellation face. Because the dynamics in VPH is derived from the Lagrangian given in Eqn. (4.1), energy, momentum and entropy are conserved exactly, just like in SPH. However, there is no surface tension effect, and the VPH particle volumina add up to the total simulated volume exactly, something that is not the case in SPH in general. One can hence hope that VPH provides an interesting improvement over SPH. Indeed, in Heß and Springel (2010) we have shown that this is the case for several test problems, such as the growth of Kelvin-Helmholtz instabilities at contact discontinuities with a large density jump. It is one of the primary goals of this chapter to see whether these improvements are also relevant in cosmological structure formation problems.

In VPH, we need to rely on an artificial viscosity to treat shocks, similarly to SPH. We here follow the standard SPH approach by Gingold and Monaghan (1977) and Balsara (1995) in introducing an extra friction force that reduces the kinetic energy and transforms it into heat in regions of rapid compression. In addition, in VPH we can also add some weak, non-dissipative “shape forces” that are designed to maintain a reasonably regular mesh geometry, which tends to improve the overall accuracy of the VPH dynamics. As discussed extensively in Heß and Springel (2010), there are different possibilities to introduce such extra forces. We derive them by adding extra terms to the Lagrangian which penalize highly distorted mesh cells. However, the optimum choice for the strength of these terms is unfortunately not (yet) clear. For this reason, we have typically carried out all our tests with several different settings for the strength of the artificial viscosity and the shape forces, finding in most cases that our results are quite insensitive to the detailed choices over a broad range of parameter settings.

Both the SPH and VPH simulations we study here have been carried out with GADGET-3, an improved version of the publicly available cosmological code GADGET-2 (last described in Springel 2005a). The code is parallelized for distributed memory machines and uses a hierarchical tree algorithm for calculation the self-gravity of the gas. A collisionless stellar or dark matter component can be optionally included as well.

### 4.2.3 Hydrodynamical moving-mesh code

Finally, the third numerical technique for hydrodynamics we examine is implemented in the moving-mesh code AREPO (Springel 2010a). It uses an entirely different approach in which the *volume* is discretized. The hydrodynamical equations are solved in terms of a Godunov scheme where at each mesh interface a Riemann problem is calculated and the resulting fluxes are used for an exchange of conserved fluid quantities between the cells. For higher spatial accuracy, this is combined with a piece-wise linear reconstruction of the gas distribution and a second-order time integration scheme, yielding overall second-order integration accuracy in smooth parts of the flow.

The particular mesh used by AREPO is given by the Voronoi tessellation of a set of mesh-generating points. The use of this particular type of mesh allows the method to be formulated such that the mesh can move along with the gas, continuously adjusting its topology to the fluid motion. The method exploits the property of a Voronoi tessellation

that the mesh changes continuously when the generating points are moved, without showing problematic mesh-tangling effects. If the points are moved with the local flow velocity (which is the standard way to operate the code), the method then has a similar Lagrangian character as SPH/VPH. However, unlike in SPH and VPH, the masses of AREPO's resolution elements (the cells) are not required to remain strictly constant. In fact, if the mesh-generating points are arranged on a static Eulerian grid, then AREPO is equivalent to the MUSCL-Hancock scheme, a popular method for second-order Eulerian gas dynamics on structured grids. AREPO should hence be viewed as being closely related to ordinary Eulerian mesh-based hydrodynamics, except that its ability to move the mesh along with the flow considerably reduces advection errors.

### 4.3 Isolated galaxies and their evolution

Before we analyze the interaction of individual galaxies within a cluster environment, we here study galaxy models in isolation to see how well the different numerical schemes treat them and whether our initial conditions are sufficiently stable. This is also intended to identify possible subtle systematic differences between the numerical schemes that may be difficult to detect in more complicated set-ups. We hence try to use identical initial conditions for the three codes as far as possible such that differences introduced by the startup procedure are minimized. We point out however that even for identical particle positions, masses, and temperatures, there can be variations in density (and hence specific entropy since we start with a prescribed temperature) directly after the start of a simulation, as a result of the different density estimation methods. We are in fact especially interested in the question whether these small differences have any bearing on the further evolution of isolated galaxy models.

To set-up compound galaxies in isolation, we construct dark matter halo models and stellar disks in dynamical equilibrium through an approximate solution of the the Jeans equations (Hernquist 1993; Springel and White 1999; Springel et al. 2005a). The primary assumption made is that the local velocity dispersion can be approximated reasonably well with a triaxial Gaussian. For the models considered here, a dark matter halo with a Hernquist profile is used, but alternatively a truncated NFW profile could be used as well, with no difference to our results. The baryonic matter is represented with a central stellar bulge, an exponential stellar disk, and an exponential gaseous disk. In a variant of this method, we shall later on also construct models of isolated galaxy clusters by adding a gaseous halo component and omitting the bulge and disk.

For definiteness, we have chosen a virial velocity of  $V_{200} = 207 \text{ km s}^{-1}$ , yielding a total mass of  $M_{\text{total}} = V_{200}^3 / (10 GH_0) = 2.1 \times 10^{12} M_{\odot}$  for the system, of which a fraction  $M_{\text{disk}}/M_{\text{total}} = 0.041$  is assumed to be in the disk, a fraction  $M_{\text{bulge}}/M_{\text{total}} = 0.01367$  of the mass is in the bulge and the rest is distributed in a halo with a concentration of  $c = 9.0$  and a spin parameter of  $\lambda = 0.033$ . Since we want to concentrate on the gas dynamics, we make the disk very gas-rich by giving it a gas fraction of 50%. We include radiative cooling (for a primordial composition), and model star formation and supernova feedback

with a simple multi-phase model for the ISM (Springel and Hernquist 2003).

In our default resolution, the gas in the disk is represented by 20000 particles, and an equal number of collisionless particles is used for the stellar disk. The bulge is represented by 10000 particles, and the dark matter halo by 30000 heavier particles that are given a larger gravitational softening length. Additionally, we introduce in the VPH simulation a few hundred gas particles with a distance of at least 600 kpc to prevent that the Voronoi cells at the surface of the isolated gas distribution become extremely large and cause technical problems in our mesh construction algorithm, which requires cells to be smaller than half the size of the box in which the VPH calculation is carried out. For the latter we use a periodic box with a sidelength of 1 Mpc.

For the AREPO simulations, we first map the given SPH gas density field to an adaptively created Cartesian mesh. The latter is composed of the set of leave cells of the Barnes and Hut (1986) oct-tree corresponding to the spatial distribution of SPH particles, with the additional requirement that the tree is refined everywhere at least to a background grid with a spacing of 62.5 kpc. We then distribute the SPH gas particles with their adaptive kernels onto the grid, in a conservative fashion. For this procedure we use  $N_{\text{ngb}} = 256$  neighbours. The resulting density field is used as the initial mesh for our moving-mesh calculation. This procedure ensures that the initial mesh geometry is unaffected by the Poisson noise inherent in the original particle set, and that the outside vacuum region around the galaxy is still covered by at least a coarse mesh. At the same time, the created mesh-based density field faithfully represents the SPH density field.

### 4.3.1 Gas density maps and structure of the disk

As we have discussed above, identical particle positions and masses do not imply equal densities in our different codes. To illustrate this further, we consider in Figure 4.2 each method’s estimate of the initial density profile in the  $z$ -direction, perpendicular to the disc. The plotted curves represent averages of the densities estimated for the individual particles/cells as a function of distance from the disk plane. We see that there is a substantial positive bias in the density estimate of SPH when a comparatively low number of neighbours of  $N_{\text{ngb}} = 33$  is used. We note that this number has often been employed in 3D simulations in practice, both to maximize the resolution and computational efficiency for a given number of particles, and to avoid particle clumping.

In Figure 4.1, we show face-on maps of the galaxy’s gas density distribution in a thin slice through the disc, after a brief period of evolution of  $t = 0.13$  Gyr. It is not surprising that the overall morphology is extremely similar as the gravity from the DM halo and the stellar disk are the primary driving force of the disc dynamics. However, upon close inspection, one can identify the higher effective resolution of VPH that produces crispier but noisier looking features compared with the more blurry appearance of the SPH result, as a result of SPH’s larger smoothing. The gas distribution of the mesh-based AREPO looks a bit sharper and less noisy than both particle based schemes, but it should be noted that due to the transformation to grid-based initial conditions there are slightly more resolution elements in this case, which will tend to reduce noise.

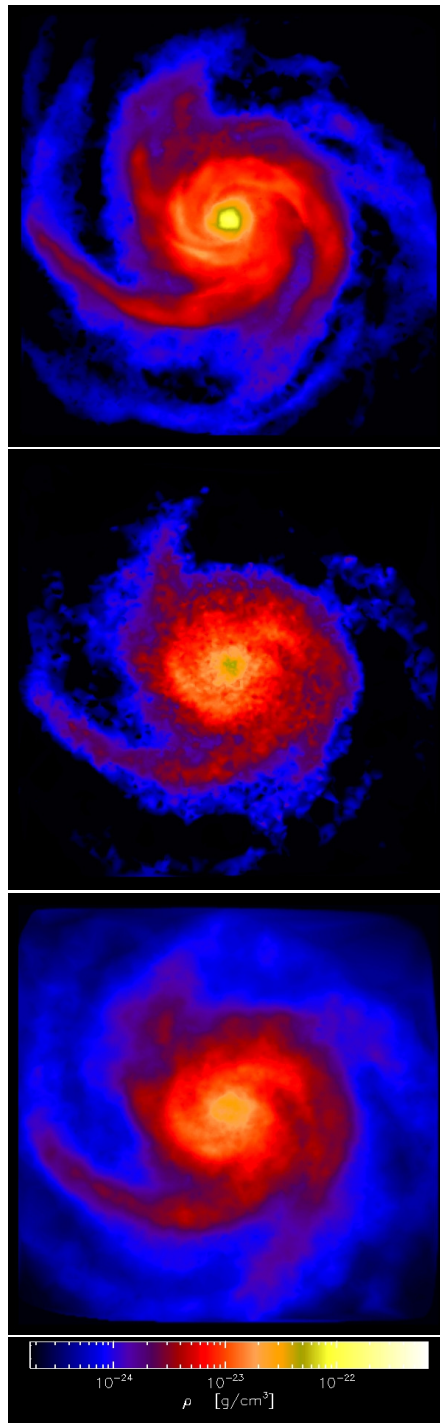


**Figure 4.1:** Projected gas density maps at  $t = 0.13$  Gyr of an isolated galaxy model simulated with SPH (bottom), VPH (middle) and AREPO (top). Each map measures 20 kpc on a side, and is based on a three dimensional Delaunay-based interpolation which has been smoothed in the  $z$ -direction.

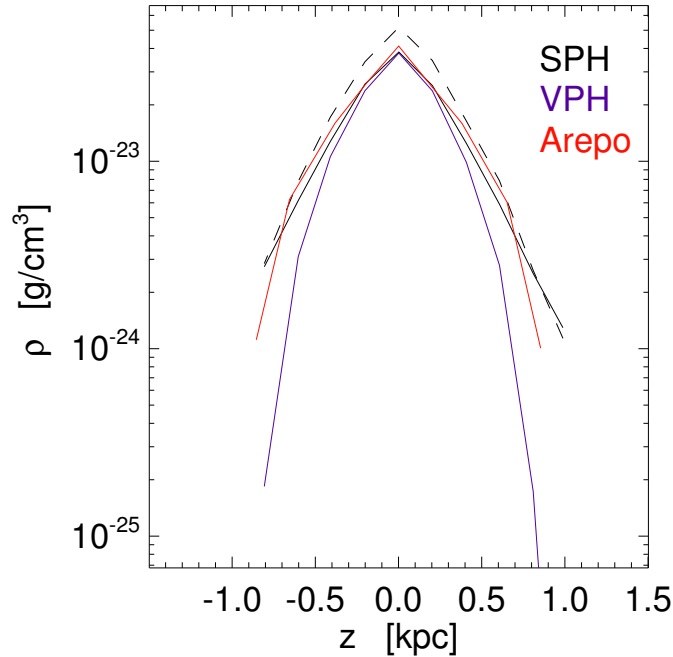


**Figure 4.2:** Vertical structure of an isolated galaxy model, initialized with different simulation methods. We here show the average (mass-weighted) density estimates of the particles/cells within 5 disk scale lengths. The black lines correspond to SPH with 64 (solid) or 33 (dashed) smoothing neighbours, respectively. The blue line is for VPH, while the red line is for AREPO.

Overall, however, the gas distribution is reassuringly similar. In Figure 4.3, we show maps of the projected stellar mass density in the disks, checking that this is also the case for the collisionless mass components. In fact, here an excellent agreement is found, confirming that the gravitational dynamics of collisionless particles is followed with equal quality in all three codes, as expected. This verifies that differences in the evolution of our galaxy models are expected to arise only from the different treatment of the hydrodynamics, and not from differences in the way the collisionless dynamics of stars and dark matter is followed.

It is also interesting to check how the vertical structure of the gaseous disk changes after some time as elapsed. In Figure 4.4, we show the density and pressure profiles for the same regions as displayed in Figure 4.1, but this time at time  $t = 0.03$  Gyr. We see that the SPH result produces comparatively wide wings in the  $z$ -profile, while VPH and AREPO tend to avoid this flaring effect. Also, there are some mild differences in the peak density reached in the midplane of the disk, which tends to be highest in AREPO, and lowest in SPH. In general, however, all three methods are clearly able to retain the initial structure of the galaxy model to a similar degree, yielding only very minor differences after some time.

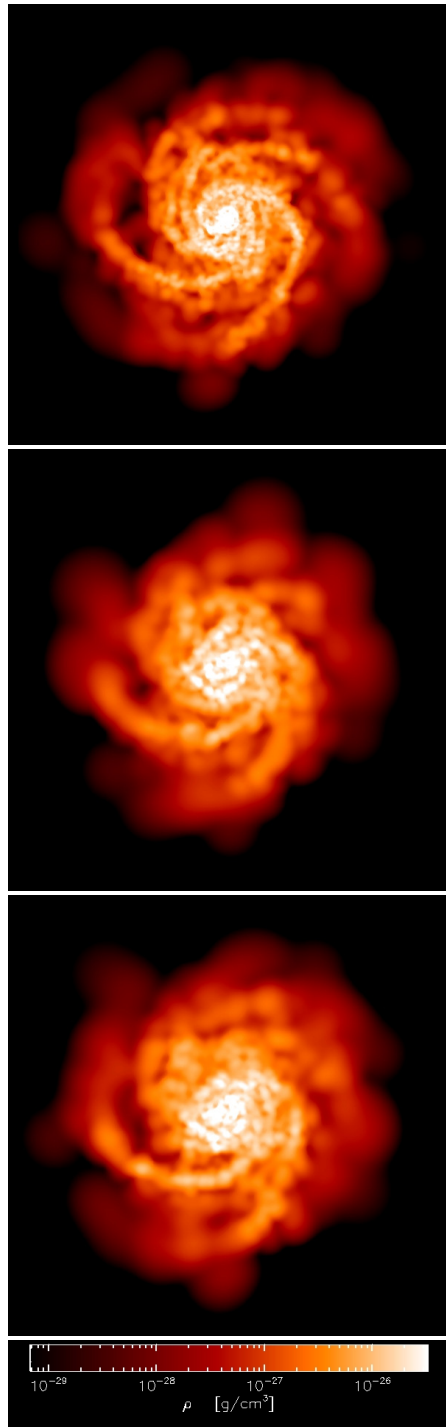


**Figure 4.3:** Projected mass density of newly formed stars (omitting stars that have been initialized in the stellar disk) in a galaxy model evolved to time  $t = 0.13$  Gyr with three different numerical schemes, AREPO, VPH, and SPH, from top to bottom, respectively. The maps measure 30 kpc on a side.



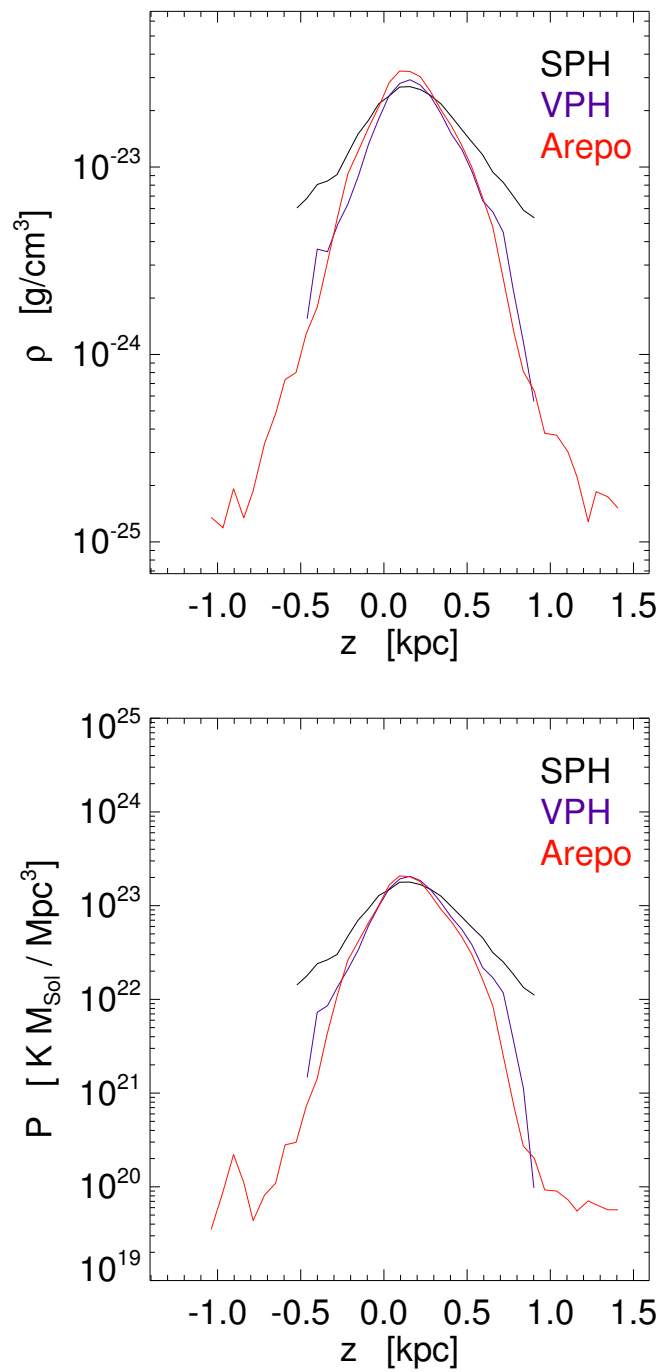


**Figure 4.4:** Vertical profiles of density and pressure in an evolved ( $t = 0.03$  Gyr) model of an isolated galaxy, simulated with either SPH (black), VPH (blue) or AREPO (red).

### 4.3.2 Star formation rate evolution

Despite the good agreement between the different methods noted above, some interesting discrepancies are revealed when looking in detail at the time evolution of the star formation rate, as shown in Figure 4.5. Here SPH shows a star formation rate that is about  $\sim 10$  per cent higher than that of VPH and AREPO, and this difference persists with time. We think this is probably caused by two effects. First, SPH shows a somewhat higher density estimate in regions above and below the disk (see Figure 4.2), and this ‘flaring’ effect due to the stronger smoothing inherent in this scheme leads to a somewhat larger volume-integrated star formation rate. Second, there is also a bias in the average SPH density estimates for the set of all particle coordinates, because for these positions one always includes a particle at zero lag in the kernel sums. This tends to lead to a spurious increase of the SPH density estimates above the expected mass-weighted mean. For the same reason, the sum of the individual SPH volume estimates,  $V_i = m_i/\rho_i$ , will typically not add up to the total simulated volume, instead yielding a slightly larger value. In any case, it is reassuring that VPH and AREPO produce very similar star formation rates as a function of time, except for a brief period after start-up, where AREPO exhibits a downward fluctuation in the star formation rate. The exact nature of this minor relaxation effect is unclear at the moment.

## 4.4 Galaxy in a wind tunnel

Simulating the interaction of a galaxy with the sparse intra-cluster gas of a galaxy cluster at high-resolution is computationally challenging, especially with the particle-based methods SPH and VPH, which do not easily lend themselves to adaptive refinement techniques. In fact, they basically require particles of equal or very similar mass to work well. Hence, if one simply wants to let a galaxy model fall into a massive cluster, the latter needs to be represented with very high particle number (because it is so massive), such that one ends up spending only a tiny fraction of the computational effort onto the galaxy and the surrounding gas, where the actual interaction takes place. A further complication is that some of the stripped gas mass may be distributed over a large region across the cluster, corroborating the need to simultaneously account for the whole cluster at high resolution.

We will nevertheless consider such simulations later on in Section 4.5, but here we first investigate an alternative, more idealized set-up, which makes it much easier to reach an adequate resolution. In this approach, we effectively put a galaxy model into a ‘wind tunnel’, i.e. a rectangular box in which we let gas stream onto the galaxy with prescribed density, velocity and temperature, matched to what we expect during a cluster passage. The much smaller volume that needs to be simulated around the galaxy in this situation drastically lowers the computational expense, and even more importantly, the simplification brought about by such a controlled set-up makes it much easier to distinguish between different numerical effects.

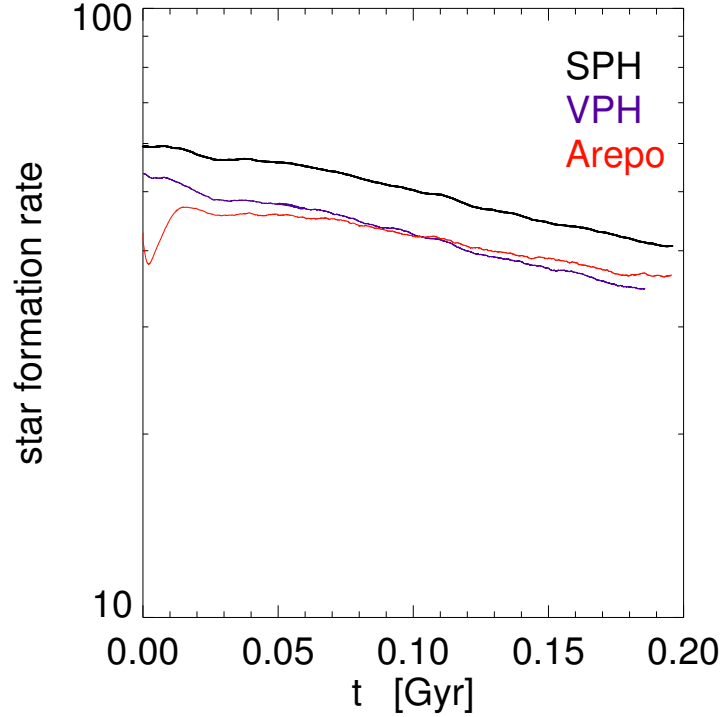


**Figure 4.5:** Time evolution of the star formation rate of an isolated galaxy model, simulated with SPH (black), VPH (blue), and AREPO (red).

#### 4.4.1 Initial conditions

For definiteness, we put our model galaxy into a rectangular box of side-length 80 kpc. At one side of the box, gas is constantly injected, which we realize in the case of SPH and VPH by creating new particles in a suitable fashion, mimicking an infinitely extended grid of particles that moves into the simulation domain. On the opposite side of the box, we effectively implement outflow boundary conditions by removing particles once they start moving out the box. Since we here focus on supersonic winds, the removal of particles at the outflow side does not lead to the propagation of perturbations upstream to the inflowing gas. In the case of the AREPO code, the inflow and outflow regions are realized in an equivalent, yet technically different fashion. We here use the on-the-fly refinement and derefinement features of the AREPO code to produce new mesh-generating points in the inflow region, and to remove them near the outflow side. The net result is identical to the SPH and VPH cases, i.e. the galaxy at the centre of the box is hit by a wind of particles/cells with prescribed density and velocity. This impinging wind has the same gas mass resolution as our target galaxy model.

For all faces of the box that form the enclosing sides of our wind tunnel, we adopt peri-

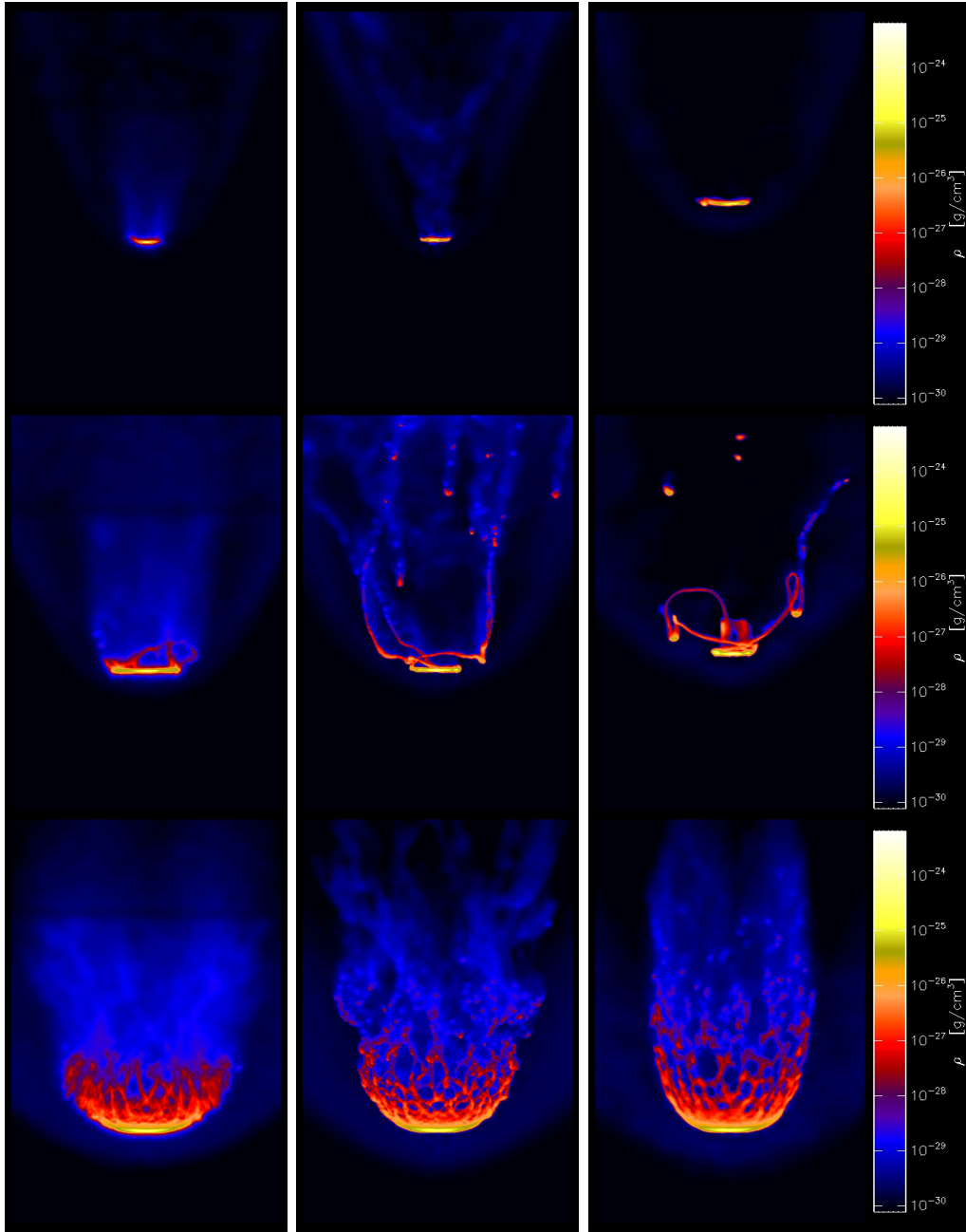


**Figure 4.6:** Projected gas density maps of a galaxy (seen edge-on) that experiences a supersonic wind from below. The different panels show the logarithm of the density field at different times, from  $T = 0.04$  Gyr (bottom row),  $T = 0.35$  Gyr (middle row) to  $T = 0.65$  Gyr (top row), and for different numerical techniques, AREPO (left column), VPH (middle column) and SPH (right column). All maps are generated with the same adaptive smoothing algorithm and have an extension of  $30 \text{ kpc} \times 45 \text{ kpc}$ .

odic boundary conditions for the gas as far as the hydrodynamics is concerned. However, periodic boundary conditions are not imposed for self-gravity, which we fully include (note that our galaxy is held together by gravity). Since the mass of the gas in the wind is quite small, most of it is unbound to the galaxy, and our restricted treatment of self-gravity to the region of the box is still a good approximation. We note that a number of similar wind tunnel experiments have previously been carried out (Agertz et al. 2007; Iapichino and Niemeyer 2008), but without a treatment of self-gravity. Note that while our setup is not capable of accounting for the tidal forces that arise when an extended galaxy travels through the gravitational potential of a cluster, these forces can be expected to be subdominant compared to the hydrodynamical forces in the outer parts of a cluster, which is the region we are most interested in. However, gravitational forces between dark matter, stars and gas inside the galaxy are very important, and our approach is the first that allows a detailed study of the response of the gravitationally coupled disk-halo system to the ram-pressure of the impinging wind. In particular, this allows a realistic measurement of the acceleration of the whole galaxy due to the ram-pressure force exerted by the wind.

In our default set-up, we have chosen a constant density of  $\rho = 1.90 \times 10^{27} \text{ g cm}^{-3}$  and a velocity of  $v = 3000 \text{ km s}^{-1}$  for the wind, letting it flow onto the galaxy in a face-on orientation. A density and velocity of this magnitude would be typical close to apocentre for a galaxy that has fallen into a large cluster. Of course, in reality the strength of the wind will be a function of the orbital phase and of parameters such as cluster size and angular momentum of the galaxy orbit. Changing these values should however not change our results at a qualitative level. For the galaxy model studied in our simulations, we have adopted structural properties identical to those described in Section 4.3. We place the galaxy suddenly into the supersonic wind, refraining from any attempt to impose a more gradual start-up in which the wind would somehow be slowly turned on.

#### 4.4.2 Stripping

Hydrodynamically, the galaxy represents an obstacle in the supersonic wind, causing a bow shock in the upstream region ahead of the galaxy. Inside the bow shock and ahead of the front side of the galaxy, the compressed wind is slowed down and exerts significant ram-pressure onto the galaxy (Gunn and Gott 1972), whereas around the sides, a region of strong shear flow is produced as the wind streams around the galaxy. In this region, the formation of Kelvin-Helmholtz instabilities is expected, which accelerate the stripping of gas from the galaxy's disk and mix it with the downstream flow. Agertz et al. (2007) has previously investigated the simpler case of a spherical, non-selfgravitating gaseous obstacle, and found substantial discrepancies between different hydrodynamical methods for the rate of gas stripping and the time until eventual complete disruption of the obstacle. Here, we are particularly interested to see whether such differences also occur between SPH, VPH and AREPO, when the more realistic disk-wind setup we are investigating here is considered.

Let us first compare the galaxy's gaseous mass loss as a function of time. We consider a gas particle (or cell) to be part of the ISM of the galaxy when it is sufficiently dense and

cold. Specifically, we require the conditions

$$\rho > 2000 \rho_{\text{wind}} \quad \text{and} \quad T < 0.5 T_{\text{wind}} \quad (4.2)$$

to be met, where  $\rho_{\text{wind}}$  and  $T_{\text{wind}}$  are the density and temperature of the wind. Furthermore, we impose an additional condition on the maximum allowed separation  $r$  of a particle from the centre-of-mass of all gas that fulfills the criterion of Eq. (4.2). Only for

$$r < 8 \text{ kpc} \quad (4.3)$$

the gas particle is considered to be part of the ISM of the primary galaxy. This condition is introduced in order to discard cold clumps of gas that have been stripped out of the galaxy but have still stayed cold and dense.

Indeed, it turns out that this secondary criterion is quite important in our SPH simulations, where the galactic disk tends to shed dense clumps under the action of the ram pressure. These fragments can still fulfill Eqn. (4.2) despite being stripped, but as they separate from the main galaxy, they eventually violate Eqn. (4.3) and are then counted as stripped gas.

This behaviour can clearly be seen in Figure 4.6, which shows projected gas density maps of the galaxy in an edge-on orientation, with time evolving from bottom to top. While the morphology of the stripping process looks similar at early times, significant differences develop over time. Both of the particle-based methods loose small clumps of gas and exhibit string-like features of quite dense gas. This effect is particularly strong in SPH. In contrast, the AREPO disk stays comparatively coherent, with all of the stripped gas moving to lower densities quickly. Hence there remains no dense debris in the downstream flow. At the latest time shown in the figure (top row), the residual gas disks of AREPO and VPH are visually significantly smaller than in SPH, suggesting that more gas has been stripped.

This impression is born out by a quantitative measurement of the gas mass that is still in the ISM phase of the galaxy model. Figure 4.7 shows the ratio of the remaining ISM gas mass to the initial mass a function of time, comparing wind tunnel simulations carried out with the three different numerical techniques. Clearly, the mass loss in SPH is smallest overall, with a tendency for about 10% of the initial mass remaining after 1 Gyr, whereas at this time the ISM of the VPH and AREPO runs is almost stripped completely.

It is interesting to note that the stripped dense gas in the SPH simulation, and to a lesser extent in the VPH run, can continue to form stars at some level. This is particularly evident in Figure 4.8, which shows maps of the projected star formation rate density in an edge-on projected, at time  $t = 0.34 \text{ Gyr}$ . This highlights that in the case of the SPH simulations the stripped gas clumps are not only very concentrated, they also continue to form stars at a quite high rate. This phenomenon is still present in VPH, albeit at a much weaker level. In contrast, AREPO does not show such a behaviour. In SPH, there are at least two effects that can help to explain the enhanced star formation in the stripped clumps. First, it is known that spurious surface tension forces in SPH exist that will slightly compress the gas of the clumps and keep them coherent. Second, there is the issue of a potential

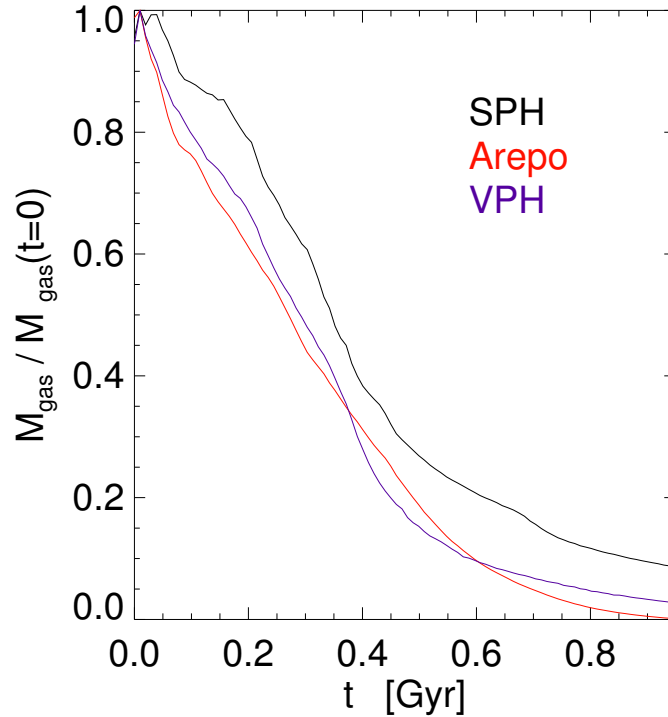


**Figure 4.7:** Loss of star-forming ISM gas as a function of time due to stripping through a supersonic wind. The gas remaining in the ISM of the galaxy is here measured according to the criteria of Eq. (4.2) and Eq. (4.3). The three solid lines show the measurements for our simulations with SPH, VPH and AREPO, as labelled. We find that the stripping is quite similar in VPH and AREPO, but significantly less efficient in SPH.

artificial suppression of gas mixing in the turbulent wake behind the galaxy. Both SPH and VPH, by construction, prevent that the low entropy gas of the ICM is mixed at the particle level with the high entropy gas of the impacting wind. This imposed Lagrangian behaviour ignores any small-scale mixing processes that could happen on scales below the spatial resolution limit. In contrast, the mesh-based approach of AREPO implicitly allows for such processes. Here, the mixing manifests itself in terms of mass exchanges between the cells, giving rise to a much more diffuse wake behind the galaxy (left column in Figure 4.6) where no gas remains that is still dense enough to support star formation. In the mesh-based approach, one may have in fact an opposite problem compared to the particle schemes. Here the need to advect the fluid over mesh interfaces can easily lead to excessive numerical mixing. However, the moving-mesh technique of AREPO should reduce such errors significantly compared to more traditional Eulerian methods.

Another interesting view on the different behaviour with respect to stripping is provided by Figure 4.9, which shows the time evolution of the sum of the star forming gas mass

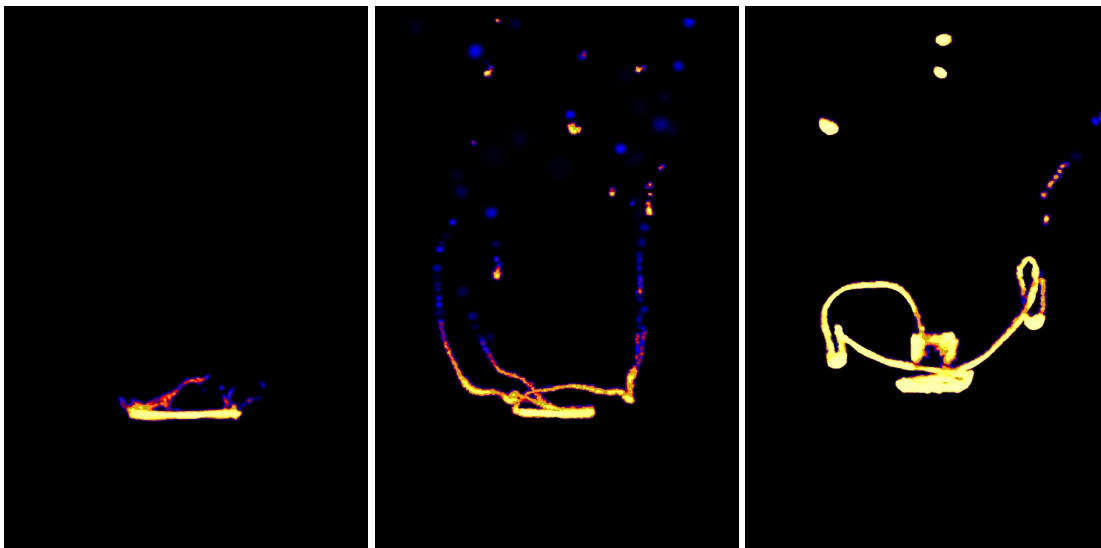


**Figure 4.8:** Maps of the projected star formation rate density in a galaxy model (seen edge-on) that encounters an IGM wind in the upwards direction. We show results at  $T = 0.34$  Gyr for our wind tunnel experiments, carried out with AREPO (left), VPH (middle) and SPH (right). Each panel extends over  $36 \text{ kpc} \times 48 \text{ kpc}$ .

(which is just the total gas mass above the star formation threshold) plus the stellar mass formed since the beginning of the simulation. Interestingly, this quantity is nearly constant in time in the case of SPH, showing that essentially none of the initially dense and star forming gas is dragged to low enough density to stop star formation. This is consistent with our earlier findings, but also makes it quantitatively evident that essentially no mixing of this low entropy gas with higher entropy material occurs. In contrast, the sum of star forming gas mass plus stellar mass declines significantly in AREPO, by more than a factor of 2 over the timescale of 1 Gyr that is shown here. The results for VPH are intermediate, showing some evidence for gas moving to higher entropy during the stripping process and thus reducing the amount of total gas available for star formation. We will investigate the entropy distribution more in Section 4.4.4.

Interestingly, the different stripping rates also lead to different accelerations of the whole galaxies, because they experience different ram pressure forces as a result of the different areas of the remaining gas disks. Since the gas in the disk is gravitationally coupled to the stellar disk and the dark matter halo, it is important to note that the wind not only strips the gas component of the galaxy, instead it accelerates the *whole* galaxy. In Figure 4.10, we show maps of the projected stellar densities of the stellar disk in SPH and VPH at an identical time, corresponding to  $T = 0.35$  Gyr. Clearly, the *whole* SPH galaxy has been pushed more into the downstream direction, demonstrating that it has experienced a higher effective ram pressure, as a consequence of the reduced stripping rate of its disk. In real galaxy clusters, this will in turn lead to a larger dynamical friction force and a somewhat faster decay of the orbit of the galaxy. An additional effect is that in the



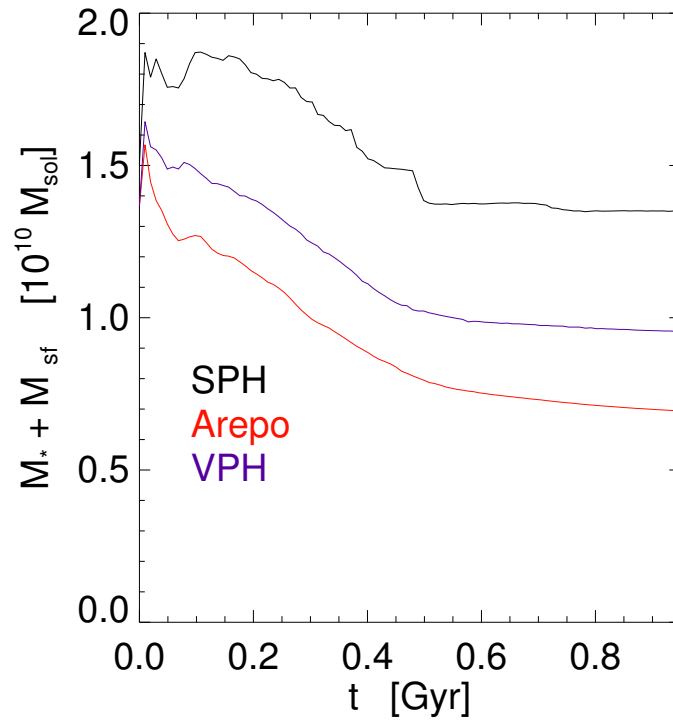


**Figure 4.9:** Time evolution of the sum of the mass of star-forming gas and the mass of all stars formed since the beginning of the simulations of a galaxy exposed to an impinging IGM wind in a wind tunnel. We show results for different simulation techniques, including an SPH-based simulation (black solid), VPH (blue solid), and AREPO (red).

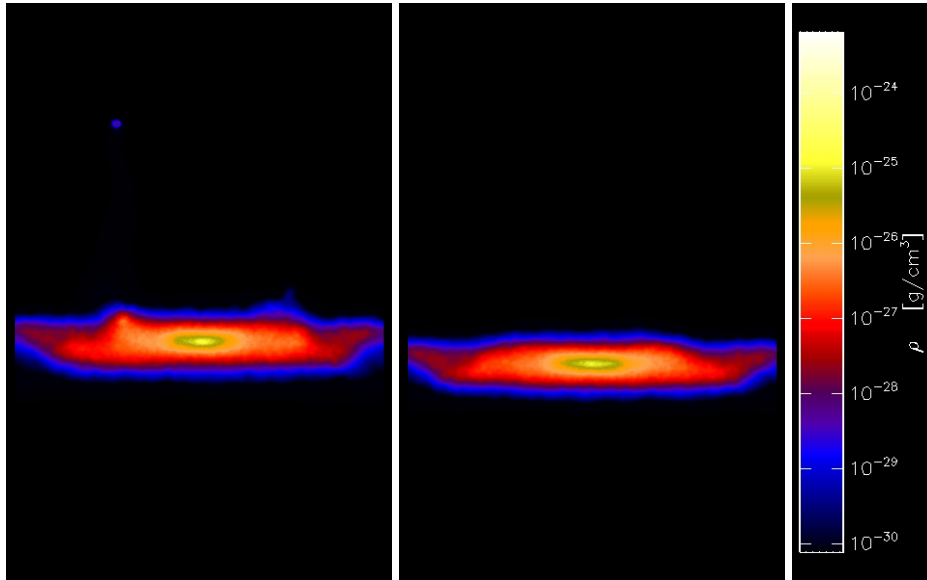


**Figure 4.10:** Stellar density maps of model galaxies (seen edge on) exposed to a supersonic IGM wind, at  $T = 0.35$  Gyr. The two panels show results for SPH (left) and VPH (right), respectively. Interestingly, the SPH galaxy is accelerated more strongly in the downstream direction, as a result of a larger effective ram pressure force due to slower stripping of its gaseous disk. The SPH simulation also shows signatures of the wind imprinted onto the morphology of the stellar disk, a behaviour that is not seen in VPH or AREPO. The two maps show the same spatial region of the wind tunnel and have an extension of  $30 \text{ kpc} \times 45 \text{ kpc}$ .

SPH case we see small features emanating in the downstream direction from the stellar disk. Figure 4.10 shows two small humps in the stellar disk, as well as a faint stellar blob at some distance further downstream. These are in fact stars of the original stellar disk that were gravitationally pulled out of the disk by dense gas. Both effects are absent in the equivalent VPH and AREPO calculations, showing again how much more (artificial) ‘coherence’ the dense gas phase shows in the SPH case, where comparative massive gas clumps are removed from the disk that stay coherent afterwards.

#### 4.4.3 Dependence on resolution and artificial viscosity

In order to examine the quantitative robustness of our wind tunnel results with respect to numerical resolution, we repeated our simulations with SPH, VPH and AREPO using both a lower and a higher resolution than in our default runs discussed thus far, where the galaxy is resolved with 80000 gas particles in the initial gas disk. With respect to this intermediate resolution, our low resolution simulations have 4 times fewer particles in each component, whereas the high resolution runs have 4 times more particles.

In Figure 4.11, we show a resolution study for the gas stripping out of the ISM as a

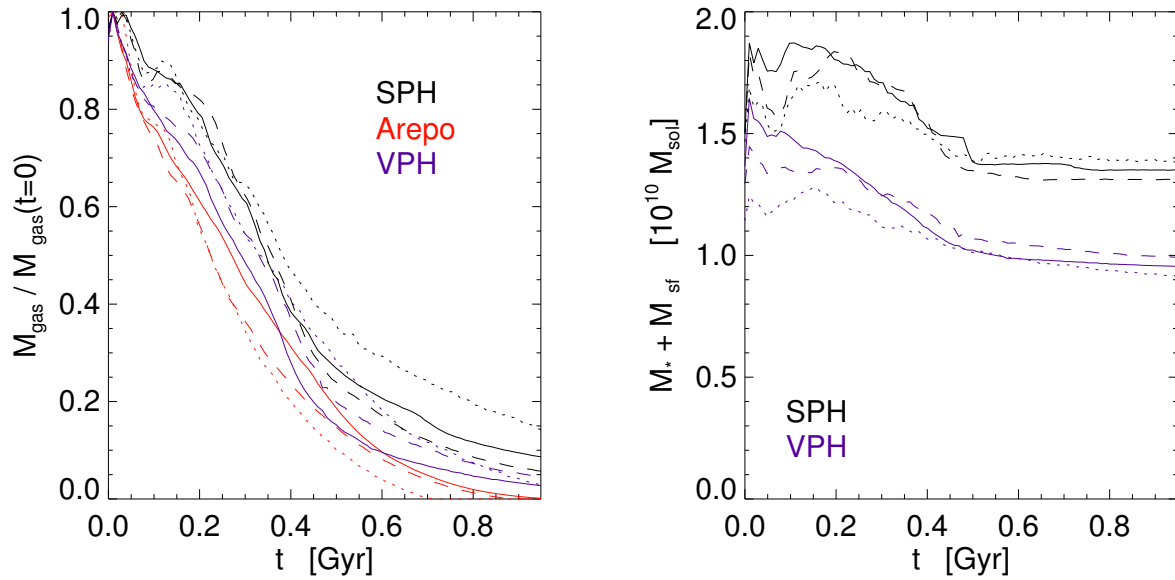


**Figure 4.11:** Resolution study of the mass loss of a galaxy in a wind tunnel. The left panel measures the gas remaining in the ISM (defined through Eq. 4.2) as a function of time, for simulations carried out with VPH, SPH, and AREPO, as labelled. In each case, three resolutions are shown, corresponding to 20000 gas particles (low resolution, dotted), 80000 gas particles (intermediate resolution, dashed), and 320000 particles (high resolution, solid) in the initial galaxy model. The panel on the right compares the sum of the remaining star forming gas plus the newly formed stellar mass as a function of time in VPH and SPH, using the same simulation set. Here a quite good convergence can be observed for the different particle-based techniques, but SPH is offset relative to VPH and has a significantly smaller amount of stripped gas.

function of time, and for the sum of remaining star forming gas and newly formed stellar mass. We find that the general trends remain very similar at all three resolution levels. That is, gas is stripped the fastest in AREPO, and slowest in SPH, with VPH taking on an intermediate role. Interestingly, in the two particle codes, the stripping proceeds more slowly when the resolution is poorer, whereas in AREPO the opposite trend is observed, the stripping tends to accelerate slightly for better resolution. We hence find that the results become more similar for better resolution. In particular, in the high resolution case, VPH is in fact very close to AREPO. When the sum of the star forming gas mass and the newly formed stars is considered, we see that this quantity is very robust for SPH and VPH as a function of resolution. This also means that the offset between VPH and SPH at late times is a manifestation of a systematic numerical difference between the two methods.

Both SPH and VPH rely on an artificial viscosity to capture shock waves and to damp out small scale numerical noise. The choice of the artificial viscosity parameterization and the associated strength of the viscous forces are crucial for the overall robustness and accuracy of the scheme. Using a large viscosity leads to more robust shock capturing, but on the other hand it may produce substantial viscous effects in regions where the gas really ought to flow without dissipation. In particular, a too high viscosity may suppress the growth of fluid instabilities that are important in gas stripping processes. We have therefore checked how our wind tunnel results for VPH depend on the viscosity setting. To this end we have reduced the viscosity parameter from our default value of  $\alpha = 1$  (high viscosity) to  $\alpha = 0.5$  (intermediate) and  $\alpha = 0.25$  (low artificial viscosity). In Figure 4.12, we compare the corresponding results for the stripping as a function of time in our low-resolution wind tunnel set-up. We see that for reduced viscosity, the gas is actually stripped a bit faster in VPH than for the high viscosity setting. This is consistent with our expectation that the numerical viscosity will tend to damp small-scale fluid instabilities and turbulence, which as a side effect reduces the stripping rate.

Another numerical nuisance parameter in VPH lies in the strength of the shape correction forces that can be introduced into the technique in order to regularize the mesh and encourage a quasi-regular particle distribution. As explained in Heß and Springel (2010), this is accomplished by adding a small term to the Lagrangian that penalizes large aspect-ratio distortions of cells and large offsets between the generating point of a cell and its center-of-mass. While not strictly necessary for VPH to work, we have found the technique to be considerably less noisy in certain conditions when such weak shape correction forces are used. In our standard implementation, their strength is controlled by two dimensionless parameters  $\beta_0 = 0.2$  and  $\beta_1 = 0.01$  (see Heß and Springel 2010, for the exact definition of these parameters). In Figure 4.13, we have included two additional lines that show our results when instead stronger correction forces described by  $\beta_0 = 0.6, \beta_1 = 0.03$  or even  $\beta_0 = 1.8, \beta_1 = 0.09$  are invoked. In both cases, this has only a very weak influence on the results, as desired.

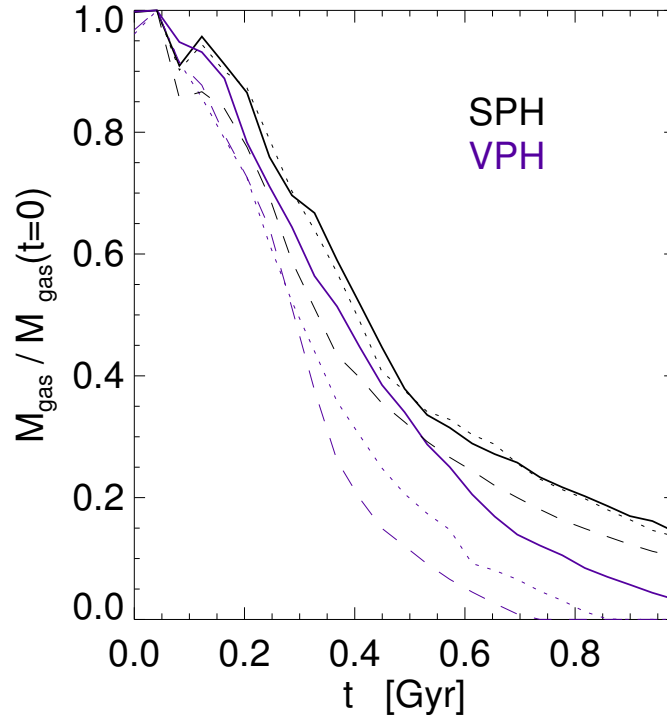


**Figure 4.12:** Dependence of the wind tunnel stripping efficiency in VPH (blue lines) and SPH (black lines) on the artificial viscosity. We show the loss of star-forming gas mass (defined as in Eq. 4.2) of our default galaxy model as a function of time, for high artificial viscosity  $\alpha = 1$  (solid lines), for intermediate strength  $\alpha = 0.5$  (dotted lines) and for low artificial viscosity  $\alpha = 0.25$  (dashed lines).

#### 4.4.4 Structure of the wake

As an extension of our analysis of the dependence of the VPH results on the artificial viscosity, we here study in more detail the structure of the wake behind the galaxy, at a fixed time of  $T = 0.35$  Gyr. We also consider a variant of VPH where an additional ‘mixing’ of the specific entropies is introduced in case a strong local shear flow is detected, as described in Heß and Springel (2010). We shall in particular look at the temperature field and the properties of the velocity field in the wake behind the disk.

First, in Figure 4.14 we show a simple profile of the density and entropy structure along the  $z$ -direction, through the centre of the galaxy and along the symmetry axis of the problem. We see that all the simulations produce a qualitatively similar structure, where density and entropy in front of the galaxy rise towards the front edge of the galaxy’s ISM, which features a very strong contact discontinuity at which both quantities jump by large factors. Interestingly, in the wake behind the galaxy, there are some noteworthy differences between the simulations. Here the SPH run shows a much reduced entropy relative to all

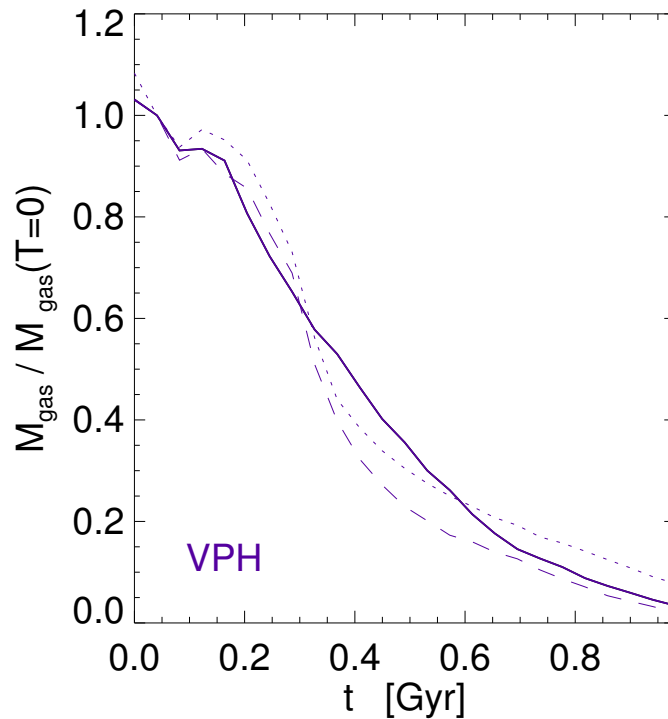


**Figure 4.13:** Dependence of the stripping efficiency in VPH on the strength of mesh shape correction forces, which consist of small, non-dissipative forces that tend to steer mesh cells towards a ‘rounder’ shape in case they have become highly asymmetric. We show the loss of star-forming gas mass (defined as in Eq. 4.2) of our default galaxy model as a function of time, for our standard choice of  $\beta_0 = 0.2, \beta_1 = 0.01$  (solid line) for parameterizing the shape correction forces. We also show results for two different settings, for  $\beta_0 = 0.6, \beta_1 = 0.03$  (dashed line) and for the somewhat extreme choice of  $\beta_0 = 1.8, \beta_1 = 0.09$  (dotted line), respectively.

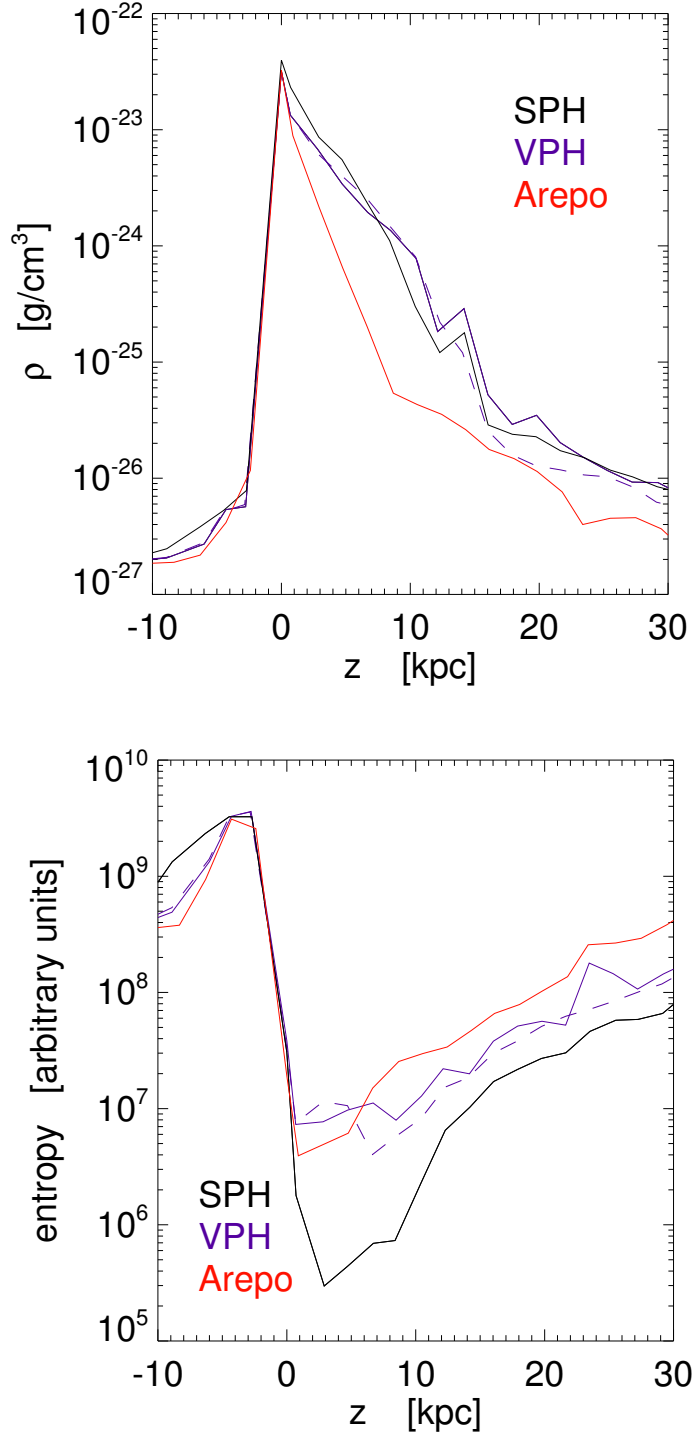


**Figure 4.14:** Profiles of gas density (top panel) and specific entropy (bottom panel) at  $t = 0.04\text{Gyr}$  along the  $z$ -direction in our wind tunnel simulations, for simulations carried out with VPH, SPH, and AREPO. The individual lines shows the averaged gas quantities in a cylinder of radius 10kpc around the  $z$ -axis. The dashed blue line is a variant of our default VPH run where an additional mixing term of the specific entropies was included.

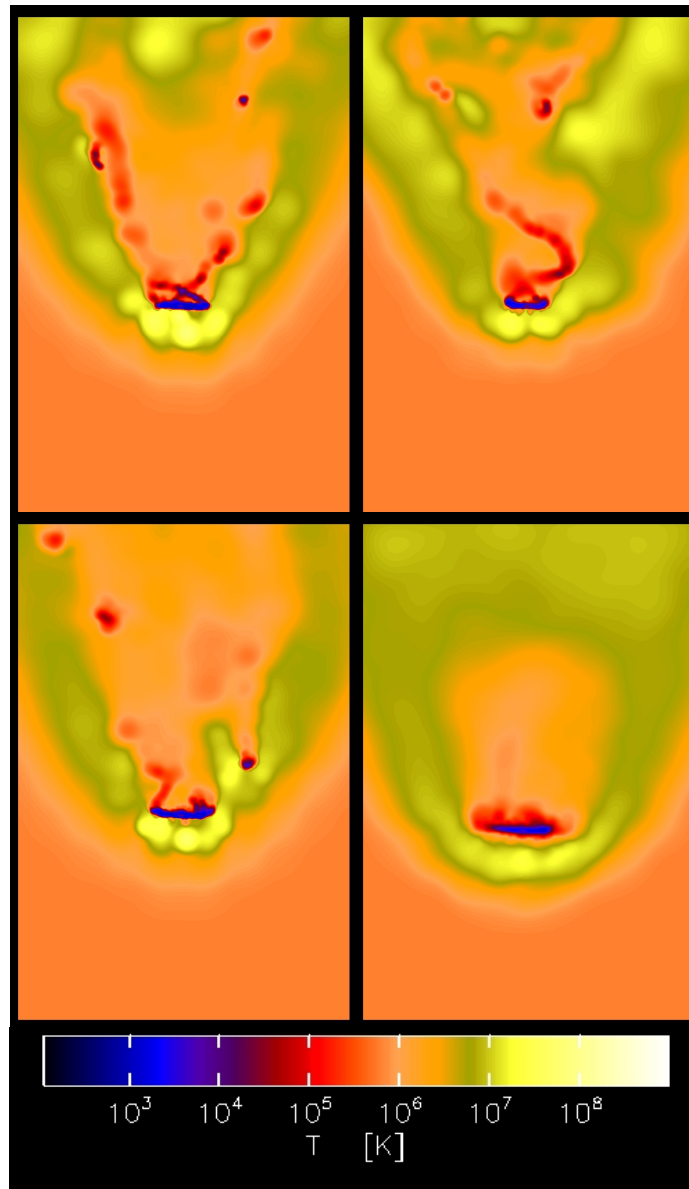


**Figure 4.15:** Logarithmic temperature maps of a galaxy (seen edge-on) that encounters a tenuous high velocity wind. The maps have an extension of  $30 \text{ kpc} \times 45 \text{ kpc}$  and show the temperature in a slice through the mid-plane of our wind tunnel simulations, at time  $T = 0.35 \text{ Gyr}$ . The two panels on top, and the one in the lower left, show simulations carried out with different variants of VPH. Our standard setting for the artificial viscosity is shown in the top left, a run with reduced artificial viscosity in the top right, and a run with an additional mixing term for the specific entropies in regions of strong shear flow in the bottom left. For comparison, the bottom right displays the results for AREPO.



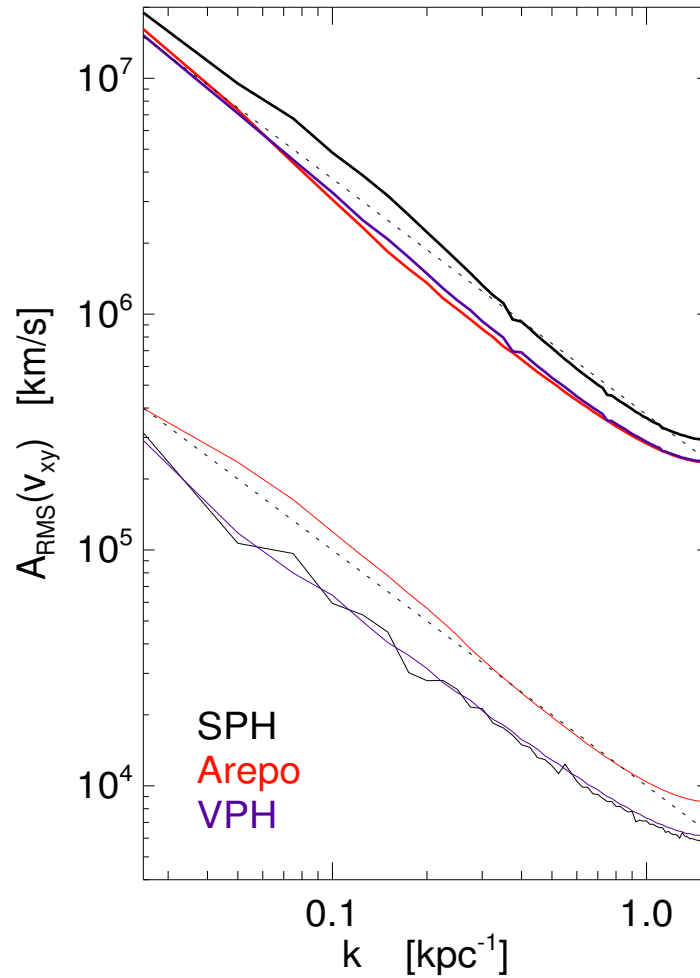


**Figure 4.16:** Average *rms* velocity amplitude as a function of scale in the transverse velocity field in two regions of our wind tunnel, upstream before the galaxy (lower set of lines) and downstream in the wake of the galaxy (upper set of lines). We show results obtained for VPH, SPH, and AREPO, as labelled. The dotted line indicates a slope of  $-1$ .

the other simulations, which agree quite well. However, in the density structure of the wake, SPH manages to agree quite well with the other results, but here it is the AREPO simulation that shows a somewhat larger difference, featuring a smaller gas density in the first  $\sim 15$  kpc of the downstream flow behind the disk. The ‘mixing’ variant of VPH results in essentially identical results in these measurements compared to ordinary VPH. We only see a slightly smoother entropy distribution of the wake, whereas the the general trend remains.

In Figure 4.15, we show the temperature field in the wake region of the disk, at time  $T = 0.35$  Gyr. We compare three different treatments of VPH, where either the artificial viscosity is varied, or additional entropy mixing terms are enabled. We also include the result of a corresponding calculation with AREPO. One can see that the reduced viscosity variant of VPH leads to a slight reduction of dense gas in the disk and the downstream part of the flow, indicating that the stripping is somewhat accelerated. On the other hand, the bow shock in front of the galaxy shows marginally more irregularity, suggesting that the shock-capturing is not as good with reduced viscosity and probably associated with larger post shock oscillations. The mixing variant of VPH produces a somewhat smoother downstream flow, as expected. Overall, the differences between the different VPH variants are quite small, and in any case, they are much smaller than the difference with respect to the AREPO result. The latter shows a more pronounced bow shock, no cool clumps in the downstream flow, and an overall less noisy appearance.

Finally, we investigate the structure of the velocity field in the wake. We are especially interested in the degree of random (‘turbulent’) gas motions produced by the galaxy in the downstream wind. To quantify the strength of these motions, we only consider the transverse velocity field perpendicular to the  $z$ -direction and measure the root-mean-square amplitude of Fourier modes of the velocity field in two different regions of our wind tunnel. We consider both a downstream region ( $z \in [10, 30]$  kpc), and a region in front of the galaxy ( $z \in [-30, -10]$  kpc) where the impinging wind is still essentially laminar. In Figure 4.16, we show our measurements for simulations carried out with VPH, SPH, and AREPO. As expected, in the region in front of the galaxy, the transverse velocity field is very quiet, and VPH and SPH agree very well. Here AREPO lies slightly higher as a result of the different approach to create the incoming mesh, which is in this case based on cell-splitting and subsequent regularization of the mesh. This procedure introduces a small level of noise in the incoming wind, whereas in SPH and VPH a perfectly quiet Cartesian grid of points is moving into the wind tunnel. More interesting is however the result for the downstream flow behind the galaxy. Here the typical turbulent velocity in the transverse direction lies two orders of magnitude higher than in the upstream region of the wind. Remarkably, the result for VPH matches that for AREPO nearly perfectly, suggesting that the statistical properties of the transverse velocity fields in the two simulations are very close. In contrast, SPH shows an elevated strength of transverse motions, which probably is a signature of a larger level of noise in the SPH run.

## 4.5 Stripping of a galaxy during cluster infall

In order to complement our wind-tunnel experiments carried out in the previous section with more realistic setups, we here want to conduct a few simulations where galaxy models are infalling into live models of galaxy clusters. This approach includes a full treatment of gravity as well as a modeling of cooling and star formation. In particular, it accounts correctly for the tidal effects of a galaxy traveling within the cluster potential. The latter inevitably changes the structure of the galaxy, most prominently by reducing its dark matter mass through tidal truncation, which in turn changes the conditions under which the hydrodynamical processes occur.

Besides looking at the stripping of the gas, we will also compare how the star formation rates in the infalling galaxy declines in our different simulations, since we expect that different numerical ram pressure will strongly affect this quantity (e.g. Kronberger et al. 2008; Kapferer et al. 2009). We note that a number of recent studies both with grid-based codes (Roediger and Brüggén 2007; Iapichino and Niemeyer 2008) and SPH codes (Jáchym et al. 2007; McCarthy et al. 2008) have begun to investigate this question in detail. Our focus here will be much more limited though and only be concerned with a comparison of our new VPH scheme relative to SPH and AREPO.

### 4.5.1 Setup of galaxy-cluster interaction simulations

For definiteness, we consider a parabolic encounter of a  $10^{12} M_{\odot}$  disk galaxy with a small  $M_{200} = 5 \times 10^{13} M_{\odot}$  galaxy cluster. The galaxy is constructed as a compound system as described in Section 4.3 but with fewer particles than in our earlier simulations. This was necessary to reduce the computational cost to an acceptable level, given that in this setup we need to represent the much larger cluster with the same mass resolution as the galaxy in order to avoid numerical problems in SPH. The latter does not work very accurately if particles of very different masses interact. In our default set-up, we have therefore chosen 4000 gas particles for the ISM of the infalling galaxy, and  $10^6$  gas particles of identical mass for the IGM of the galaxy cluster.

For the cluster, we adopted a gas-fraction of 17% and a NFW concentration of  $c = 2.0$ . The trajectory of the encounter starts at a distance of 700 kpc, just outside of the virial radius, and follows a parabolic orbit where the minimal distance of the two objects would be 50 kpc if they were point masses. Compared to the orbital plane the galaxy's disk is tilted by  $\theta = 30^{\circ}$  and  $\phi = 30^{\circ}$  (see Duc et al. 2000, for a sketch of the orbital geometry). We note that we can draw general conclusions from a single choice of inclination angles since they have no significant effect on the gas stripping (Roediger and Brüggén 2006).

### 4.5.2 Properties of the head wind

In Figure 4.17, we show the properties of the wind encountered by the infalling galaxy as a function of time. In order to define whether a gas particle or cell still belongs to the

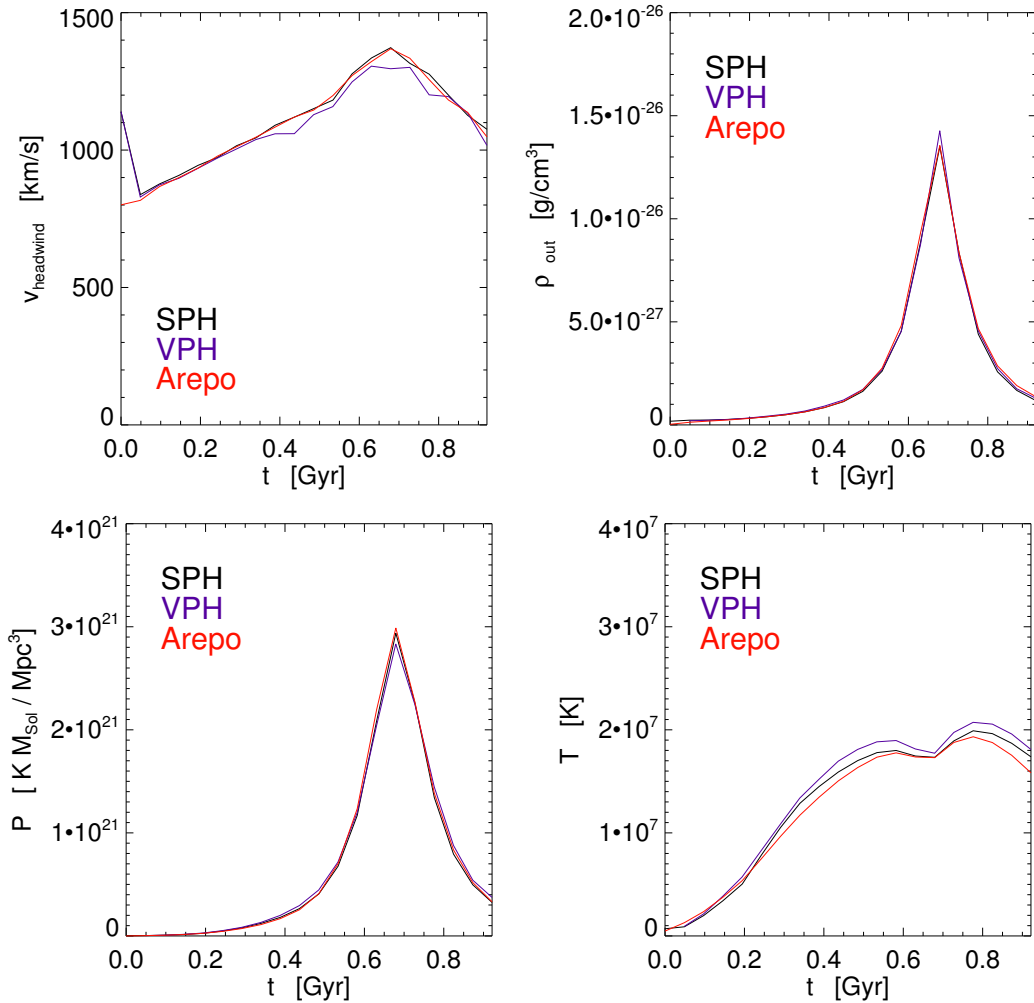


**Figure 4.17:** Properties of the ‘headwind’ encountered by the infalling galaxy. The velocity difference is calculated between the center-of-mass of the galaxy (defined according to Eqn. 4.4) and the environment, which is taken as a sector of a spherical shell with an opening angle of 30deg in the direction of the velocity vector and at a distance of [45,99] kpc with respect to the galaxy centre. All simulations have been conducted with cooling and star formation. In each panel, we show results for simulations with VPH (blue), SPH (black), and AREPO (red), comparing from top left to bottom right the relative velocity, density, pressure and temperature of the wind encountered by the galaxy as a function of time.

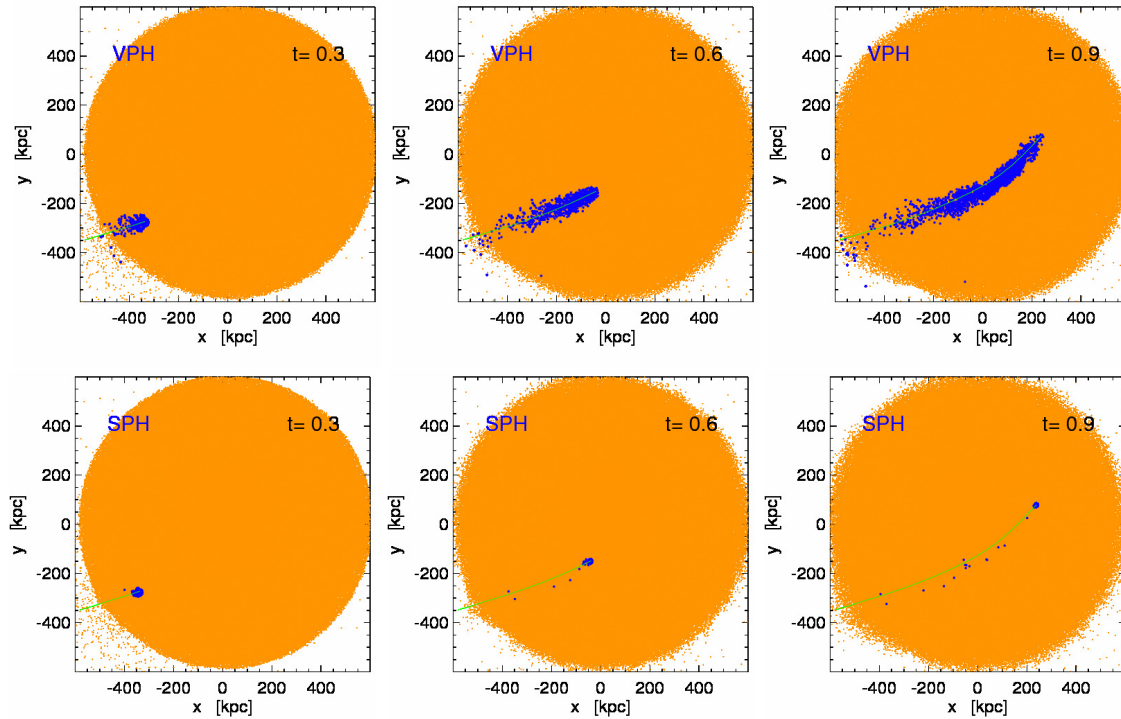


**Figure 4.18:** Visual comparison of the spatial distribution of lost gas particles (large blue dots) from the ISM of an infalling galaxy simulated with VPH (top row) and SPH (bottom row) at  $t = 0.3$  Gyr (left column),  $t = 0.6$  Gyr (middle column) and  $t = 0.9$  Gyr (right column) and. The green curve traces out the orbit of the galaxy through the cluster up to the time of each individual panel, as labelled. The gas particles of the target cluster's IGM are shown as yellow dots.

galaxy we have used the criterion

$$\rho > 4 \times 10^{-26} \text{ g cm}^{-3} \quad \text{and} \quad T < 10^6 \text{ K.} \quad (4.4)$$

Furthermore, we additionally impose the condition that the separation  $r$  of particles from the centre-of-mass of the remaining gravitationally bound DM of the galaxy is less than 20 kpc. We note that with this definition the galaxy can in principle also accrete new gas from the cluster that cools onto the ISM and helps to feed star formation. We include results for VPH, SPH and AREPO in Figure 4.17, and as the comparison shows, there is generally very good agreement between the three different simulation techniques. All three show a strong rise of density and pressure as the galaxy approaches and passes pericentre, while the temperature is roughly constant, reflecting the nearly isothermal conditions in the cluster gas. There are no significant deviations in the orbit of the galaxy between the different methods, hence any difference in the evolution of the galaxies can only arise from differences in the hydrodynamical treatment of the interaction of galaxy and cluster gas.

### 4.5.3 Gas stripping and star formation truncation

In Figure 4.18, we show a visual comparison of the gas stripping in the VPH and SPH simulations, where it is readily apparent that the gas mass loss proceeds much slower in SPH than in VPH. This is confirmed by quantitative measurements shown in Figure 4.19, which include results for the gas stripping in three different simulations of the encounter of a galaxy with the cluster ICM. Interestingly, VPH loses gas here even somewhat faster than AREPO, but both methods yield a substantially faster loss of gas than SPH. While at time  $\sim 1$  Gyr the VPH simulation has lost *all* of the gas, the galaxy in SPH still retains half of it.

This substantial difference is corroborated by the behaviour of the star formation rate in the galaxies, shown in Figure 4.20. Here SPH shows the slowest decline overall, while both VPH and AREPO lead to a rapid termination of star formation, which implies a quick reddening of the galaxies. It is a well known problem in galaxy formation to understand the colours of cluster galaxies in detail. Semi-analytic models of galaxy formation have commonly predicted a rather quick truncation of star formation upon cluster infall, yielding cluster populations that are actually too red (e.g. Weinmann et al. 2006). It can be expected, due to the fast stripping, that our VPH and AREPO simulations suffer from the same problem, and even SPH may be in tension. This likely indicates that the stripping efficiencies in these simulations are in general too large, probably because the ISM is still underresolved and appears as a homogenous dense phase instead of being resolved into a true multi-phase medium. The latter would make the medium more porous, allowing very dense clouds of gas to resist the ICM wind for a longer time and to stay in the infalling galaxy.

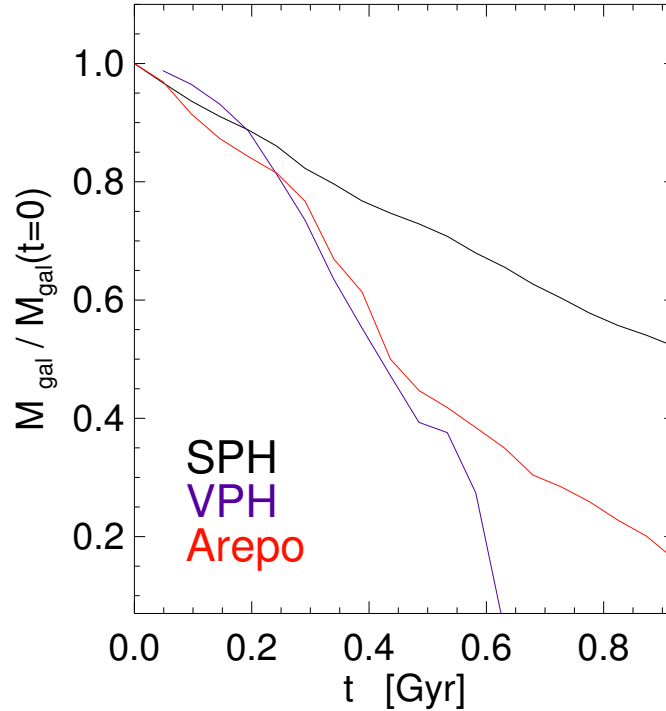


**Figure 4.19:** Gas mass as a function of time still bound to a galaxy that is infalling into a galaxy cluster. We include simulation results for SPH (black), VPH (red) and AREPO (blue).

## 4.6 Cosmological cluster simulations

We now turn to results for fully cosmological simulations of cluster formation. We first carry out a comparison of the gas content of satellite systems in ‘zoom’ simulations of the formation of rich galaxy clusters, carried out with VPH, SPH and AREPO. We here primarily want to check whether the differences we have observed in the stripping of dense ISM gas out of galaxies in our earlier more idealized simulations manifest themselves also in non-radiative simulations, where the density contrast is much smaller. Second, we study the well known Santa Barbara cluster of Frenk et al. (1999) in order to investigate whether VPH produces a higher entropy in the cluster centre compared to SPH, which would then make it closer to the results of mesh codes that have been applied to this problem. We also use this cluster in order to assess the numerical convergence of VPH for the properties of the intracluster gas.

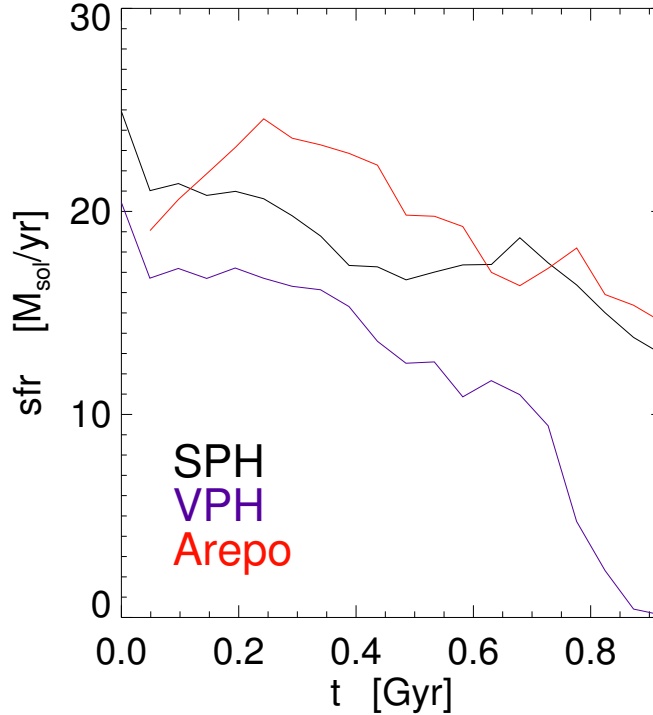


**Figure 4.20:** The star forming rate within a distance of 20kpc from the galaxy centre as a function of time. We include simulation results for SPH (black), VPH (blue) and AREPO (red).

#### 4.6.1 Gas stripping in non-radiative zoom simulations of galaxy clusters

In order to simulate the formation of rich galaxy clusters in the  $\Lambda$ CDM cosmology, we extract a massive halo from the Millenium Simulation (Springel et al. 2005c), and resimulate this cluster with the addition of gas. To this end we trace the particles that make up the cluster back to the original initial conditions at  $z = 127$ , thereby finding the Lagrangian region out of which the cluster formed. This region is then populated both with dark matter and gas particles, which are pertubed with the original displacement field. We can also increase the resolution compared to that in the original simulation if desired, in which case additional small-scale fluctuation power is added in the region between the old and new Nyquist frequencies. Further away from the region that holds the cluster material and its immediate surroundings, the resolution is reduced by combining particles into progressively heavier 'boundary' particles. In this way, the resolution gradually declines with distance from the cluster while the gravitational tidal field that influences its formation is still accurately determined. With this standard 'zoom' technique, the computational



cost is concentrated in the small region of interest, allowing high resolution simulations of individual objects in comparably short time.

For definiteness, we have picked a cluster of virial mass  $M_{200} = 1.8 \times 10^{15} M_{\odot}$ , which we resimulate with a baryon fraction  $\Omega_b = 0.045$ . The other cosmological parameters are the same as in the original Millennium Simulation and are given by  $\Omega_m = 0.25$ ,  $\Omega_{\Lambda} = 0.75$ ,  $\sigma_8 = 0.9$ ,  $h = 0.73$ , and  $n = 1$ . We have initialized the resimulations at  $z = 127$  and evolved them with VPH and SPH to the present epoch, treating the gas as a non-radiative mix of hydrogen and helium.

We identify halos in the simulations by applying the FOF algorithm to the high-resolution dark matter particles. Each gas particle is assigned to the group in which its closest dark matter particle lies. We then apply the SUBFIND algorithm to the particle groups found this way in order to decompose them into gravitationally bound (sub)groups. Using the IDs attached to each particle we can track individual halos/subhalos as a function of time, and, in particular, study how the gas content of subhalos declines as a halo falls into the cluster. In order to reduce numerical noise in our simulation comparison, we however restrict our substructure selection to a sample where more than 60% of the DM particles can be found in every studied simulation run.

As an example, we show in Figure 4.21 the evolution of the gas fraction of two different substructures as a function of their distance to the cluster centre (the corresponding times are indicated by the redshift labels on the upper axis), comparing results for VPH and SPH simulations. For both substructures, we find good agreement in the early infall phase, for distances larger than about  $\sim 3 R_{\text{vir}}$ . At smaller separations, the influence of the cluster is however very noticeable already, and the substructures lose gas quickly. However, in both of these examples, we clearly identify a considerably larger gas loss in the VPH run than in SPH at the last time when we can still find the substructures before they are disrupted. This is consistent with our earlier findings for the stripping of the dense ISM gas.

In Figure 4.22, we now consider all of the substructures around the cluster at the final time, and simply compare the gas mass fraction in substructures as a function of clustercentric radius. Even though the results are a bit noisy, we find a clear statistical trend of a smaller gas mass fraction in the VPH run relative to SPH, especially in the region  $\sim 1 - 3 R_{\text{vir}}$ , where the gas fraction declines rapidly. Interestingly, a simulation with AREPO for the same cluster initial conditions shows a yet smaller gas fraction still bound to the infalling dark matter halos. We hence conclude that even at the level of non-radiative simulations, there are already significant differences in the stripping of gas out of infalling substructure, which also implies that the mixing of gas in massive halos can be expected to be substantially different.

### 4.6.2 The Santa Barbara Cluster

The ‘Santa Barbara cluster comparison project’ of Frenk et al. (1999) analyzed the results of a large number of different cosmological hydrodynamical codes for the formation of a rich cluster of galaxies with non-radiative gas. The comparison involved both SPH codes and hydrodynamical mesh codes, and focussed, in particular, on the resulting thermodynamic

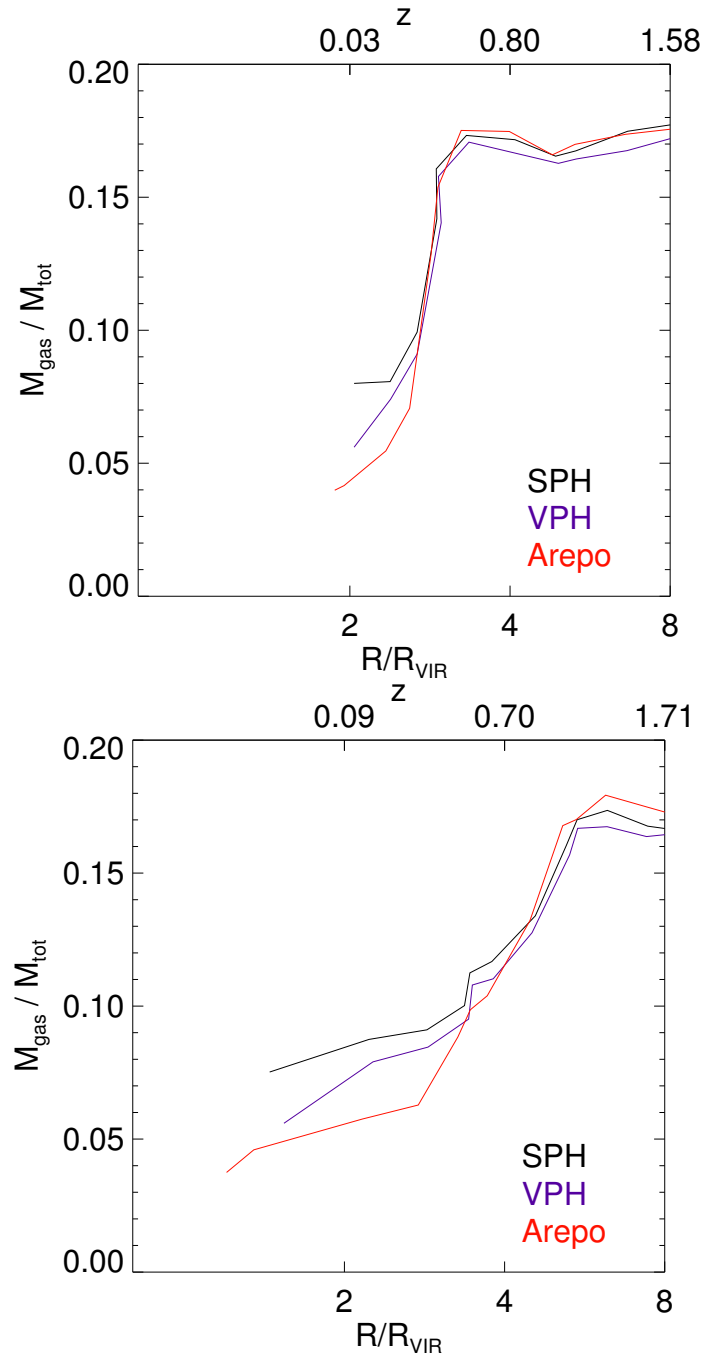


**Figure 4.21:** Gas fraction as a function of distance to the cluster center for two representative (sub)halos that fall into the cluster. We show results for a substructure with  $4.5k$  DM-particles (top panel) and  $1.8k$  DM-particles (bottom) panel, comparing results for SPH (black), VPH (blue) and AREPO (red). We find a clear difference in the stripping process. In the SPH simulation, the substructure keeps a higher gas content until it is disrupted.

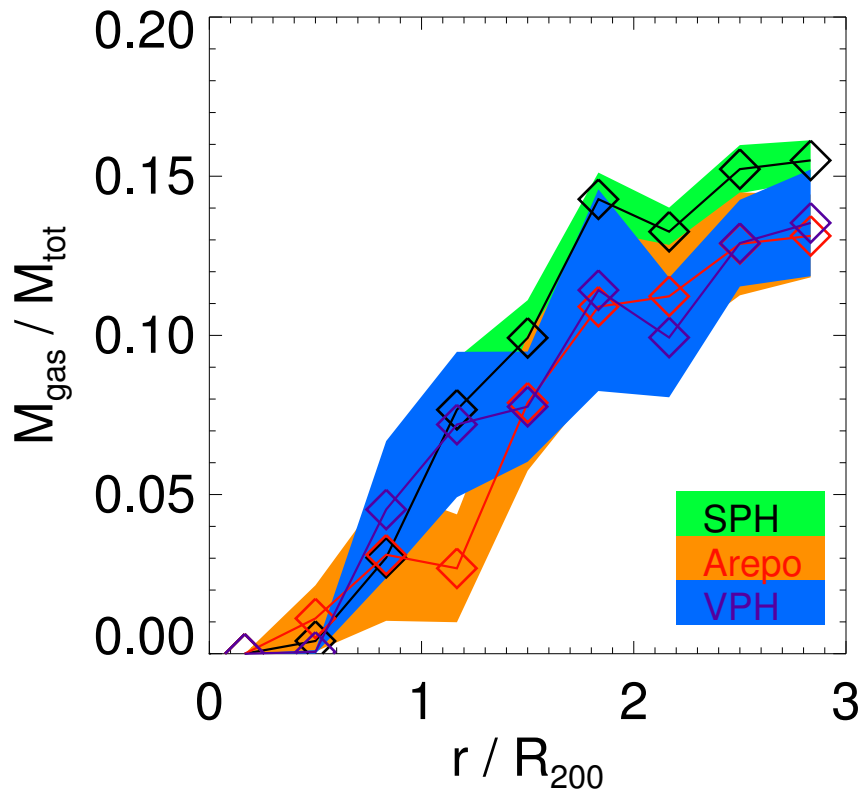


**Figure 4.22:** Gas fraction of substructures as a function of their distance to the cluster center. We compare results for SPH (black with green shade), VPH (blue) and AREPO (red with orange shadow), including only subhalos more massive than  $M > 3 \cdot 10^{11} M_{\odot}$  to exclude poorly resolved small structures. The shaded areas indicate one standard deviation from counting statistics.

properties of the intracluster gas. An important result that emerged from the study was that the different methods systematically disagree in the amount of entropy predicted for the central regions of the cluster, with the mesh-based approaches yielding consistently higher central entropy and correspondingly lower density than the SPH codes.

The Santa Barbara (SB) cluster has become a standard test problem for cosmological hydrodynamic codes, with results reported in numerous studies. Recently, some studies have suggested that the difference seen between the various techniques is primarily associated with differences in the treatment of mixing (Mitchell et al. 2009), which is suppressed in SPH by construction, and this may artificially lower the central entropy. Specifically, it has been suggested that this problem may be related to a suppression of Raleigh-Taylor fluid instability in SPH. If the difference is caused by the lack mixing at the particle level as pointed out by Tasker et al. (2008); Wadsley et al. (2008b) the VPH results should agree with SPH.

In the spirit of the original project (Frenk et al. 1999), we here rerun the SB cluster

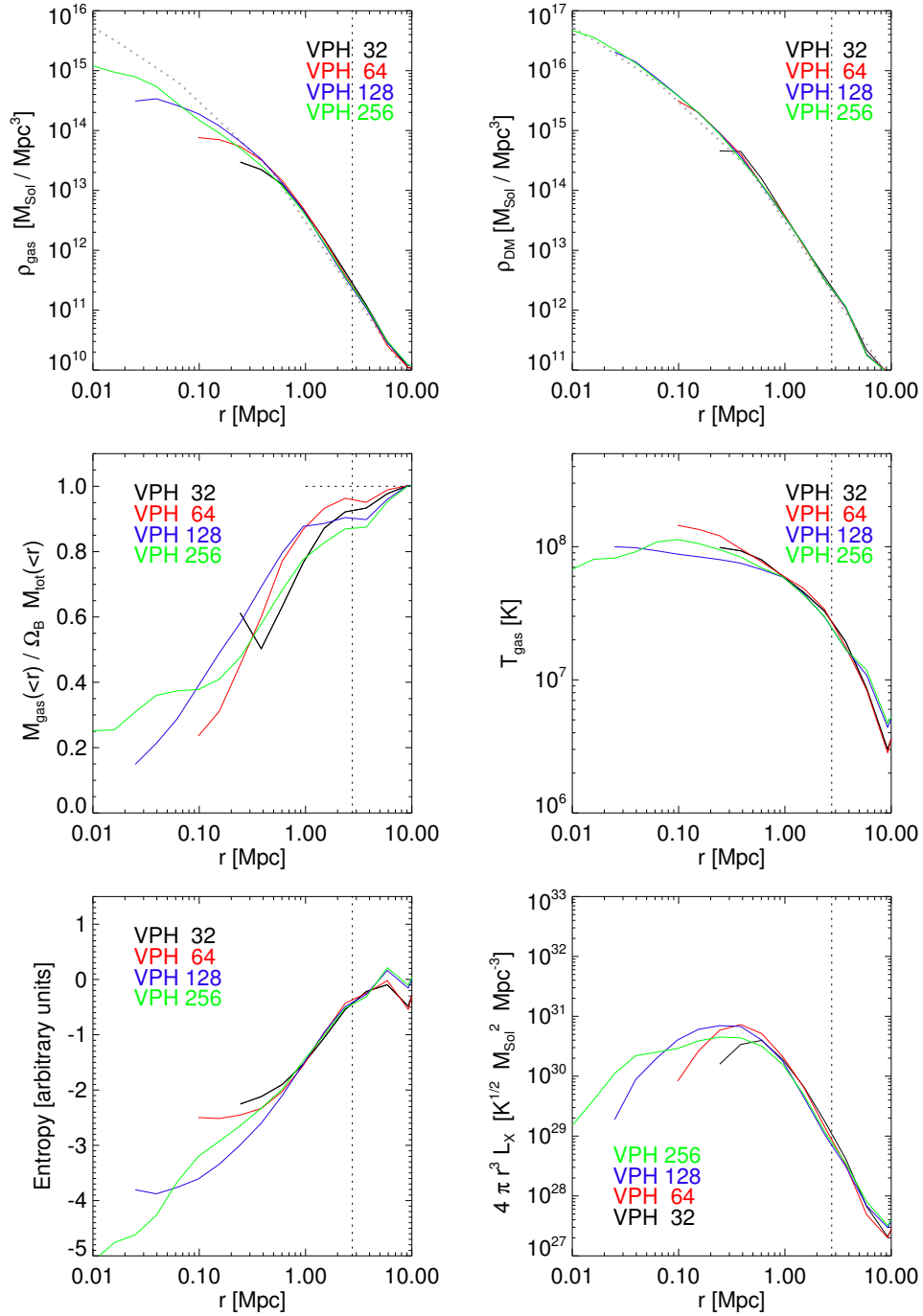


**Figure 4.23:** Comparison to the cosmological “Santa Barbara Cluster Comparison project“. Radial profiles of (from top left to bottom right): Gas-density, Dark matter density, cumulative gas-fraction, gas-temperature, specific entropy and x-ray luminosity. All properties have been obtained by massweighted arithmetic mean values within logarithmic spaced bins. Shown VPH simulation with resolutions with gas particle numbers of  $32^3$  (black),  $64^3$  (red),  $128^3$  (blue) and  $256^3$  (green).

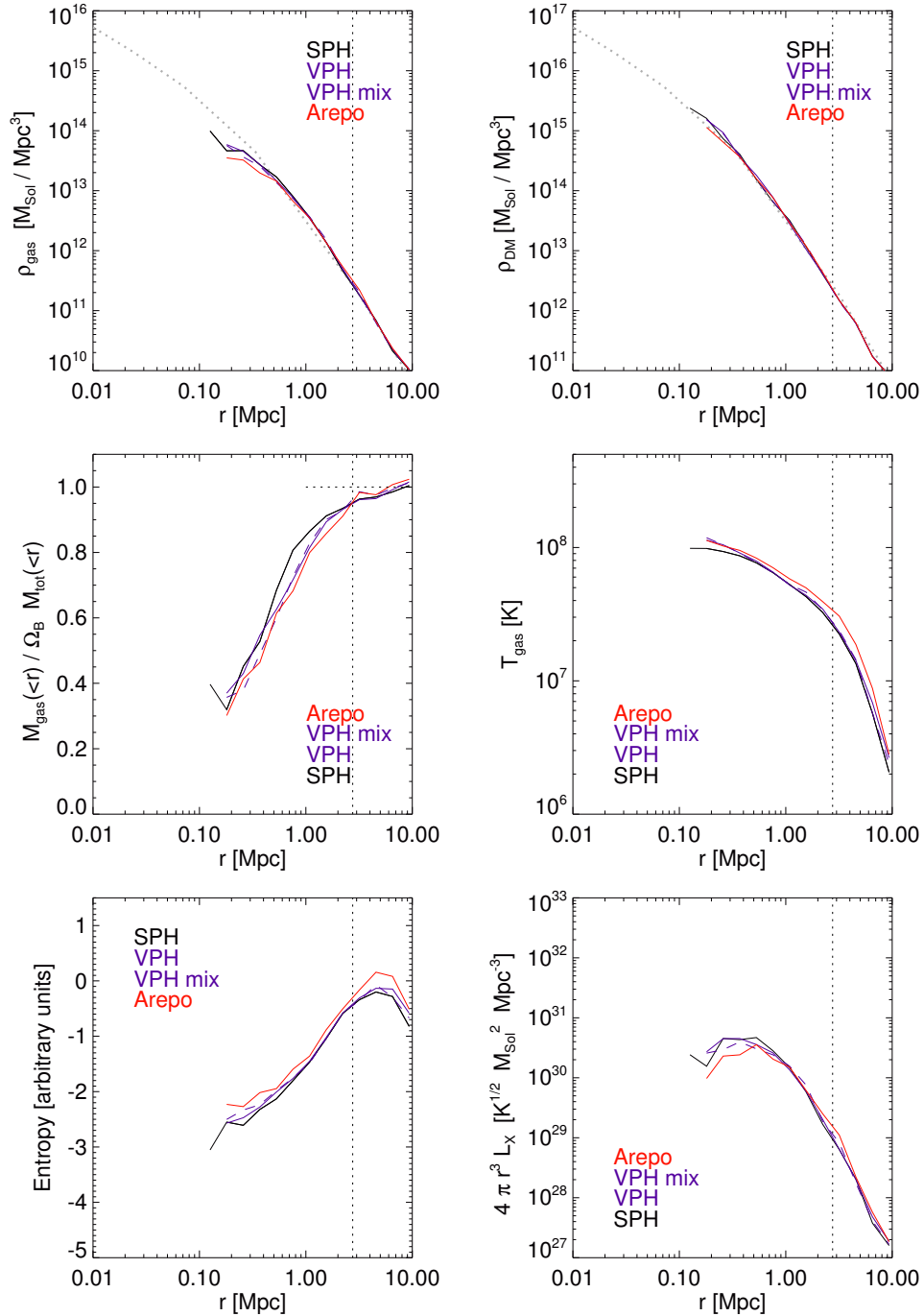


**Figure 4.24:** Comparison to the cosmological “Santa Barbara Cluster Comparison project“. Radial profiles of (from top left to bottom right): Gas-density, Dark matter density, cumulative gas-fraction, gas-temperature, specific entropy and x-ray luminosity. All properties have been obtained by massweighted arithmetic mean values within logarithmic spaced bins. Shown are SPH (black), AREPO (red), VPH (blue solid) and a variant of VPH with mixing scheme (blue dashed).

with the different hydrodynamical methods studied so far in this paper. We are especially interested in the question whether VPH differs in its predictions for the central cluster region compared with SPH, which may be expected due to the different stripping efficiencies of these techniques. We use the same initial conditions that have been used in the original SB cluster comparison project, where an Einstein-de-Sitter cosmological model with mean density  $\Omega_m = 1$ , Hubble constant  $H_0 = 50 \text{ km s}^{-1} \text{ Mpc}^{-1}$ , and baryon fraction of  $\Omega_b = 0.1$  was used. The initial conditions were constructed as a constrained realization where a rich cluster corresponding to a  $3\sigma$  peak was imposed to form in the centre of a cubic box with a sidelength of 64 Mpc, in an otherwise random realization.

We first simulate the SB cluster at a variety of different resolutions using VPH, ranging from  $2 \times 32^3$  to  $2 \times 256^3$  particles, in order to see how well the method converges for the primary cluster properties. In Figure 4.23, we show the results of this convergence test, in terms of radial profiles for gas density, dark matter density, enclosed gas fraction, temperature, entropy, and specific X-ray emissivity. We find that the convergence is in general very good for the outer profiles and the dark matter properties. Only in the very centre some interesting differences can be observed. For the most part they can be simply understood as an imprint of the varying spatial and mass resolution across the sequence, where shortly before the resolution limit is reached the lower resolution runs peel away from the converged result seen in the higher res simulations. This is for example the case for the entropy and gas density profiles. It is clear however that VPH predicts the formation of an entropy core region, which is qualitatively different from the falling entropy profiles that are typically observed with SPH all the way to the centre of halos.

It is therefore interesting to compare the VPH results directly to the other methods. We do this at the fixed resolution of  $2 \times 128^3$  in Figure 4.24. Besides VPH, SPH and AREPO, we here also include results for our ‘artificial mixing’ variant of VPH, which may yield interesting differences if the origin of the discrepancy between SPH and mesh techniques is indeed caused by a mixing effect. Interestingly, our results for the entropy profile of VPH lie intermediate between SPH and the mesh-code AREPO. The mixing variant of VPH leads to an additional increase in the central entropy, but this is a small effect overall and subdominant compared to the difference present between SPH and VPH. Although we can not be sure that our mixing scheme solves the problem of mixing on a sub-particle level entirely, Figure 4.24 shows that especially the entropy towards the core is indeed elevated when an artificial mixing is included. The quantitative strength of this effect depends however somewhat on the parameters adopted to describe the mixing, and the optimum choice for them is uncertain at this point. We note however that already ordinary VPH shows significant differences to SPH, and is qualitatively closer to the mesh-based result, as it also develops a clear entropy core. This suggests that the different treatment of stripping and of contact discontinuities in VPH is an important improvements that directly influences the thermodynamic structure of the central cluster gas.

## 4.7 Discussion

In this study, we have carried out a systematic comparison of the properties of our new Voronoi particle hydrodynamics (VPH) method with respect to SPH and mesh-based hydrodynamics. We have focussed on stripping processes in galaxies and halos upon infall into galaxy clusters. Here, it is expected that the outer parts of gaseous disks are quickly removed due to ram pressure stripping (Gunn and Gott 1972), but the subsequent more gradual gas loss sensitively depends on the ability of hydrodynamical codes to capture fluid instabilities occurring in shear flows around the galaxies. The recent findings that SPH appears to exhibit severe inaccuracies in this regime has prompted us to develop the alternative VPH method (Heß and Springel 2010). In the present paper, we study how this new technique compares with traditional SPH and the new moving-mesh code AREPO.

To this end, we first compared results for isolated compound galaxy models, both in isolation and in wind tunnels where they were exposed to a supersonic head wind. This set-up allowed relatively high-resolution simulations of the wind-ISM interaction. Our simulations have revealed substantial differences in the rate at which dense ISM gas is stripped, and in the appearance of this gas in the downstream part of the flow. SPH showed a much lower stripping rate than both VPH and the mesh-code AREPO. Also, we could show that essentially none of the ISM gas could ever be lifted in SPH to lower density. Instead, if gas was stripped, it stayed in coherent dense blobs, where even star formation could continue. As a result, the SPH galaxy also experienced the largest displacement due to the ram pressure of the impinging wind. AREPO, in contrast, showed a rapid loss of gas out of the disk, which was furthermore efficiently mixed with other gas, so that lower densities were reached quickly by the stripped gas and star formation was stopped. VPH exhibited a behaviour intermediate between SPH and AREPO. While almost as much gas was stripped in VPH as in AREPO, the mixing of this gas with the incoming wind was clearly much less efficient.

We followed up these simulations with numerical experiments where we dropped galaxy models in real live cluster models. Even though here the resolution was substantially lower, we obtained results in good qualitative agreement with our wind tunnel runs. Likewise, in non-radiative cosmological simulations of galaxy cluster formation, we followed individual subhalos as they fell into the forming cluster, finding again that the gas content of satellite systems declined most slowly in SPH, while the stripping in VPH and especially in AREPO proceeded noticeably faster.

Finally, we considered simulations of the Santa Barbara cluster, which has become an important test problem for evaluating cosmological hydrodynamical codes. Here the VPH runs show clearly an elevated entropy compared to SPH, and their central temperature structure is much closer to being isothermal. These profiles are in fact quite close to the results of the mesh-based code AREPO, and if an additional artificial mixing term is invoked, they become even more similar. Also here, VPH takes on an intermediate role between SPH and AREPO.

Unfortunately, it is not readily possible to decide which of the numerical techniques we studied yields the correct answer. However, it can be demonstrated that SPH incorrectly

suppresses fluid instabilities and stripping in certain situations (Agertz et al. 2007; Springel 2010b), whereas VPH can be shown to do better in this respect (Heß and Springel 2010). This circumstantial evidence strongly suggests that VPH should also yield more accurate results in the cosmological context. In this study we have shown that VPH indeed gives results that come quite close to the mesh-based code AREPO. This is encouraging, and perhaps this means that we are on the way to soon reach an agreement between particle-based and mesh-based hydrodynamics in cosmology.



# Chapter 5

## Conclusions

Even though galaxies, clusters of galaxies and the still bigger structures of the cosmic web are dominated by gravity, understanding their luminous properties in detail requires simulations that include a proper description of hydrodynamical processes, especially when one wants to model the small-scale structures contained in these objects. Although there are several well-established methods to simulate the hydrodynamical processes during cosmic structure growth, the very fact that there are so many different techniques already indicates that there is no single method at this point that clearly outperforms all the competing methods. Instead, each of the methods suffers from certain disadvantages. For example, while the Lagrangian nature of SPH makes it in principle ideal for galaxy formation (and for this reason it has been widely used), it has recently been found that SPH yields physically unreliable results at sharp jumps in gas density, and the origin of this shortcoming can be traced back to the basic density estimate of SPH.

In this work, we have introduced a new approach to simulate hydrodynamics, which we call ‘Voronoi particle hydrodynamics’ (VPH). VPH is also a Lagrangian method, but its density estimate is based on a Voronoi tessellation instead of on adaptive kernel interpolation. The Voronoi tessellation is defined directly by the particle positions and yields an unambiguous volume information for each point, which can be readily converted into an estimate of the density field. The fully adaptive mesh created by the Voronoi tessellation offers higher spatial resolution for a given number of particles when compared to the kernel-based density estimation method used in SPH. In fact, the tessellation technique provides a close to optimum density estimate for a given point distribution (Pelupessy et al. 2003). In particular, contact discontinuities can be resolved on the scale of one cell and with a correct computation of the forces on the particles directly at the discontinuity. This is a rather important advantage compared to SPH, whose density estimate leads to spurious forces across density jumps. VPH can therefore eliminate the artificial surface tension effects that play a crucial role in SPH’s unphysical suppression of the growth of fluid instabilities.

These advantages of VPH have to be weighted against some disadvantages and potential problems in the new Voronoi-based particle hydrodynamics scheme. Probably the most important one of them is the noise inherent in the scheme. While this noise is in general

of comparable size as in SPH (which is in fact quite noisy compared to Eulerian methods), the noise in VPH turns out to be sensitive to the degree of regularity of the Voronoi mesh. Flows that exhibit considerable amounts of shear tend to develop Voronoi meshes with a large number of points that lie close to the surfaces of their corresponding Voronoi cells. For these cells, the accuracy of the gradient estimates decreases substantially, introducing unwanted noise into the evolution of the system. In addition, it becomes more difficult to safely prevent particle interpenetration in this situation, simply because being close to a cell boundary also implies that the distance to the next neighbour on the other side of the cell face is very small.

One way to avoid such close particle pairs is to introduce additional artificial viscosity terms that try to counteract the formation of highly elongated cells, and the occurrence of points close to a cell boundary. However, we found that this approach can be insufficient in situations where strong shear flows are present, because here the artificial viscosity forces should be as small as possible. We have therefore developed a more radical approach in which conservative correction terms are added to the fluid Lagrangian right from the beginning. These terms are chosen to penalize strong deviations from regular mesh geometries, and to exert weak non-dissipative forces on the points in order to maintain a reasonably regular mesh. Indeed, we have found that the fluid motion under these forces shows the desired properties. Provided one is careful to not make these forces too large, otherwise measurable deviations from the correct hydrodynamic behaviour are introduced, manifesting themselves for example in scale-dependent distortions of the sound speed.

If one is careful to not make these forces too large, otherwise measurable deviations from the correct hydrodynamic behaviour are introduced, manifesting themselves for example in scale-dependent distortions of the sound speed.

We have seamlessly integrated the Voronoi particle hydrodynamics scheme into the cosmological simulation code GADGET-3, where it can be used as a direct replacement for SPH if desired. This in particular means that VPH is fully parallelized for distributed memory systems, and can in principle already be used for extremely large simulations. Also, other aspects of the physics (in particular self-gravity, radiative cooling, star formation or feedback processes) that are implemented in GADGET-3 can be reused in essentially identical fashion in VPH. This makes it possible to right away apply Voronoi particle hydrodynamics to current problems in cosmological structure formation.

In our subsequent first applications of VPH, we have systematically compared the properties of our new scheme with respect to SPH and mesh-based hydrodynamics. We focused on stripping processes in galaxies and halos when they first fall into galaxy clusters, because there we expect significantly different behaviour of these hydrodynamical methods. A galaxy that enters the virialized region of a cluster experiences a head wind composed of intra-cluster gas. This wind builds up ram pressure in front of the galaxy. At the outskirts of the gaseous disk, where the gas is only weakly bound and the gravitational restoring forces are small, gas is quickly removed by ram pressure stripping (Gunn and Gott 1972). After this initial phase with intense stripping, a more gradual loss of gas sets in which is sensitive to the details of the flow around the galaxy. In particular, the loss of gas at the edges of the gaseous disk depends on the capability of the hydrodynamical method

at a given resolution to simulate fluid instabilities in the shear flows around the ‘galaxy obstacle’. Especially for SPH, severe doubts have arisen (Agertz et al. 2007) whether its dampening of fluid instabilities leads to wrong estimates of the stripping rate. Since we have implemented VPH and SPH in the same code, we have been in the situation to test for differences between SPH and VPH that have their origin only in the different hydrodynamical treatment, because we can otherwise guarantee the same treatment for self-gravity, star formation and cooling. In addition, in order to compare the results of VPH also to a mesh-based method, we have extended our comparisons to also include the new moving-mesh code AREPO.

First, we compared the behaviour of isolated compound galaxy models and found that the different techniques agree on the general evolution of the galaxy when no external influence is present. Then we put these compound galaxy models into a wind tunnel and exposed them to a supersonic wind representing the hot intra-cluster medium (ICM) of an infalling galaxy. This particular setup allowed relatively high-resolution simulations. Indeed, in our simulations we have discovered significant differences between the codes in the stripping rate of the ISM, and in the properties of the stripped gas. SPH showed the lowest rate of gas-stripping, whereas both VPH and AREPO agreed better with each other when the resolution was high. The remaining difference between the particle-based VPH code and the mesh-based method appears to arise from the complete lack of mixing in VPH at the particle scale, a property that it also shares with SPH. This influences the density of the stripped gas, which remains higher in VPH and SPH compared to AREPO. This in turn favours continued star formation in the stripped gas in the particle codes, something that does not happen in AREPO, where the gas is diluted much more quickly and star formation shuts down in everywhere in the stripped gas.

Furthermore, in SPH the high density contrast between the ISM and the wind leads to spurious forces which effectively act as an additional surface tension that tries to minimize the “surface area” of the phase boundary. This behaviour suppresses fluid instabilities which should arise as an important part of the stripping process. Hence these spurious forces reduce the stripping rate, in addition to forming small ‘droplets’ out of gas that manages to be stripped. Overall, this leads to a higher level of star formation in the stripped gas in SPH compared to VPH. Another consequence of the fact that more gas remains in the galaxy for a longer time in SPH is that the galaxy then experiences a higher effective ram pressure force. This implies a higher acceleration of the galaxy in SPH compared with VPH and AREPO simulations. This in turn should lead to a faster decay of the orbit of a galaxy as it falls into a galaxy cluster, and hence to a modification of the merger timescale.

To check whether our findings also hold in more realistic setups where the gravitational tidal field of a galaxy cluster potential is self-consistently included, we dropped our compound galaxy models into a full three-dimensional cluster model. Here the resolution in the galaxy itself had to be lowered substantially in order to have an equal resolution for the large cluster and the infalling galaxy. Nevertheless, our results were in very good qualitative agreement with our findings from the more idealized wind tunnel runs. Again, SPH predicted the lowest gas stripping rate, AREPO the highest, with VPH taking on an

intermediate role.

We have also examined the performance of VPH in fully cosmological simulations of structure formation. To this end we first considered simulations of the formation of galaxy clusters in zoom simulations where we in particular followed individual subhalos as they fell into the forming cluster. Here again we found that our results for the stripping efficiency of gas agreed with our earlier findings. The fraction of gas in an infalling substructure again declined faster in VPH simulations as in SPH, actually even a bit faster in some objects than in AREPO simulations.

Finally, we turned to simulations of the Santa Barbara cluster (Frenk et al. 1999), which has become an important test problem for evaluating cosmological hydrodynamical codes. It has been used to compare many different hydrodynamic simulation methods in the past, and is therefore a good test to compare VPH with previous results that have been published for this problem. Interestingly, we have found that the VPH runs show a small core with an elevated entropy compared to SPH, making the radial structure overall closer to that found with the mesh-based code AREPO. If we add an artificial mixing mechanism that averages the thermal energies of nearby cells in the presence of strong shear, the core in VPH becomes even closer to the AREPO results.

In this thesis, we have confirmed that the peculiarities of SPH can lead to substantial differences in cosmological simulations, especially when fluid instabilities occur. Our new Voronoi particle hydrodynamics (VPH) scheme does not suffer from some of SPH's shortcomings, because it uses a different density estimate. VPH performs better in simulating fluid instabilities, and our tests showed that the results obtained in VPH simulations are closer to mesh-based methods. However, there remain still residual differences. We suspect that a key to resolving these differences would be to reliably and correctly account for mixing at the resolution scale, both in Lagrangian and mesh-based methods. Currently both Lagrangian and mesh-based approaches cannot claim to treat mixing in the physically correct fashion, however, and further investigations are needed to understand what the correct answer for this really is. Nevertheless, we have shown that VPH is a worthwhile improvement compared to the popular SPH method. It retains all of its principle advantages, offers an improved spatial resolution for the same number of resolution elements, and avoids the spurious suppression of fluid instabilities across large density jumps. These characteristics make it a very attractive tool for future high-resolution cosmological simulations.

# Appendix A

## Voronoi mesh operators and shape control

### A.1 Differential operators on Voronoi meshes

In this Appendix, we collect some useful formulae for discretized versions of differential operators on Voronoi meshes, such as the gradient or the divergence, and we test the accuracy of the gradient estimate as a function of the regularity of the Voronoi mesh.

#### A.1.1 Gradient

The cell averaged gradient of any quantity  $\phi$  can be estimated via Gauss' theorem. One can use Gauss' theorem on a product of a constant vector times a scalar field and arrives at:

$$\frac{1}{V} \int_V \vec{\nabla} \phi \, dV = \frac{1}{V} \int_{\partial V} \phi \, d\vec{S}, \quad (\text{A.1})$$

which can be used as one way to derive an estimate of the local gradient by approximating the value of  $\phi$  on the surface of a cell with the arithmetic mean between the cell and its neighbours. However, one can also circumvent the problem of finding a proper value for  $\phi$  on the surface by using a different starting point. We now use Gauss' theorem on  $(\vec{1} \cdot \vec{r}) \vec{\nabla} \phi$ , where  $\vec{1}$  is the unit vector. This yields:

$$\int_V \vec{\nabla} \phi \, dV = \int_{\partial V} \vec{r} (\vec{\nabla} \phi \cdot d\vec{S}) - \int_V \vec{r} \Delta \phi \, dV \quad (\text{A.2})$$

With the help of  $R_{ij} = |\vec{r}_j - \vec{r}_i|$  as the distance between points  $i$  and  $j$ , and  $\vec{r}^\perp$  as  $\vec{r}$  projected onto the plane of the face  $A_{ij}$  (for definition see Figure 3.1 and Fig A.1),  $\vec{r}$  becomes  $\vec{r} = \vec{r}^\perp + (\vec{r}_i - \vec{r}_j)/2 + \vec{r}_i$ , and then the right hand side can be discretized for the Voronoi mesh as follows:

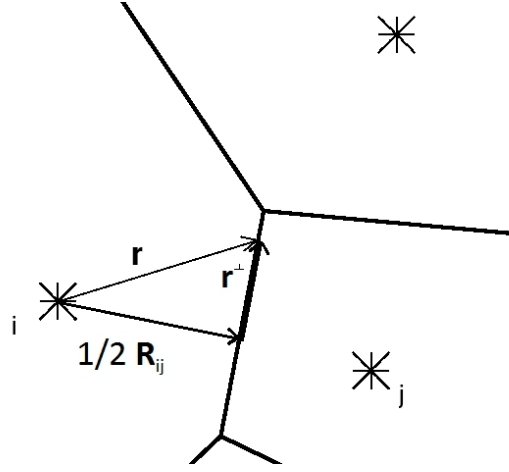


**Figure A.1:** Sketch of a Voronoi diagram to illustrate the integration variables

$$\int_{\partial V} \vec{r} (\vec{\nabla} \phi \cdot d\vec{S}) \quad (\text{A.3})$$

$$= \sum_{j \neq i} \int_{A_{ij}} \vec{r} (\vec{\nabla} \phi \cdot d\vec{S}) - \int_{V_i} \vec{r} \Delta \phi dV \quad (\text{A.4})$$

$$= \sum_{j \neq i} \int_{A_{ij}} \left( \frac{1}{2} \vec{R}_{ij} + \vec{r}^\perp \right) (\vec{\nabla} \phi \cdot \vec{e}_{ij}) dS + \vec{r}_i \sum_{j \neq i} \int_{A_{ij}} (\vec{\nabla} \phi \cdot \vec{e}_{ij}) dS - \int_{V_i} \vec{r} \Delta \phi dV \quad (\text{A.5})$$

$$= \sum_{j \neq i} (\vec{\nabla} \phi \cdot \vec{R}_{ij}) A_{ij} \left( \frac{1}{2} \vec{e}_{ij} + \frac{1}{R_{ij} A_{ij}} \int_{A_{ij}} \vec{r}^\perp dS \right) + \vec{r}_i \int_{V_i} \Delta \phi dV - \int_{V_i} \vec{r} \Delta \phi dV \quad (\text{A.6})$$

$$= \sum_{j \neq i} (\vec{\nabla} \phi \cdot \vec{R}_{ij}) A_{ij} \left( \frac{1}{2} \vec{e}_{ij} + \frac{\vec{c}_{ij}}{R_{ij}} \right) - \int_{V_i} (\vec{r} - \vec{r}_i) \Delta \phi dV \quad (\text{A.7})$$

$$(\text{A.8})$$

The second term vanishes for linear scalar fields. It is therefore only a second order correction that becomes negligible for sufficiently smooth fields if the points lie near the centroids of their cells so that  $\int_V (\vec{r} - \vec{r}_i) dV = 0$ .

Now we use  $\vec{R}_{ij} \cdot \vec{\nabla} \phi = (\phi_j - \phi_i)$ , so that we obtain for the gradient estimate  $(\vec{\nabla} \phi)_i$  at point  $i$

$$(\vec{\nabla} \phi)_i = \frac{1}{V_i} \sum_{j \neq i} (\phi_j - \phi_i) A_{ij} \left( \frac{1}{2} \vec{e}_{ij} + \frac{\vec{c}_{ij}}{R_{ij}} \right) \quad (\text{A.9})$$

$$= \frac{1}{V_i} \sum_{j \neq i} A_{ij} \left[ (\phi_j - \phi_i) \frac{\vec{c}_{ij}}{R_{ij}} + (\phi_j + \phi_i) \frac{\vec{e}_{ij}}{2} \right]. \quad (\text{A.10})$$

We note that application of this gradient estimate to the Euler momentum equation in the form

$$m_i \ddot{\vec{r}}_i = -V_i \vec{\nabla} P_i \quad (\text{A.11})$$

yields

$$m_i \ddot{\vec{r}}_i = - \sum_{j \neq i} A_{ij} \left[ (P_j - P_i) \frac{\vec{c}_{ij}}{R_{ij}} + (P_j + P_i) \frac{\vec{e}_{ij}}{2} \right] \quad (\text{A.12})$$

which is consistent with the expression derived directly from the Lagrangian.

### A.1.2 Divergence and curl

To estimate the divergence and curl of the velocity which we need for the viscosity calculation of Section 3.2.4 we use the same reasoning as in A.2.

$$\int_{V_i} (\vec{r} \nabla (\nabla \vec{v}) + \nabla \vec{v}) dV = \int_{\partial V} \vec{r} (\nabla \vec{v} \cdot d\vec{S}). \quad (\text{A.13})$$

Provided that  $\frac{1}{V_i} \int_{V_i} \nabla \times (\nabla \times \vec{v})$  vanishes for a linear field we define our estimator for the divergence operator as

$$(\nabla \cdot \vec{v})_i = -\frac{1}{V_i} \sum_{j \neq i} A_{ij} \left[ (\vec{v}_j - \vec{v}_i) \cdot \left( \frac{1}{2} \vec{e}_{ij} + \frac{\vec{c}_{ij}}{R_{ij}} \right) \right]. \quad (\text{A.14})$$

Similarly, the curl estimator can be defined in the form

$$(\nabla \times \vec{B})_i = -\frac{1}{V_i} \sum_{j \neq i} A_{ij} \left[ (\vec{B}_j - \vec{B}_i) \times \left( \frac{1}{2} \vec{e}_{ij} + \frac{\vec{c}_{ij}}{R_{ij}} \right) \right], \quad (\text{A.15})$$

where  $\vec{B}$  denotes some vector field. Again applying Gauss' theorem to  $\nabla \phi$  the Laplacian of a scalar function  $\phi$  can be computed as

$$\int_V \Delta \phi dV = \sum_{j \neq i} \int_{A_{ij}} (\vec{\nabla} \phi \cdot d\vec{S}) \simeq \sum_{j \neq i} A_{ij} \frac{\phi_j - \phi_i}{R_{ij}}. \quad (\text{A.16})$$

### A.1.3 Accuracy of the gradient

To test the accuracy of the numerical gradient estimate, we assume a quadratic model function  $\phi(\vec{r})$  with constant gradient and Hesse matrix, of the form

$$\phi(\vec{r}) = \phi_0 + \vec{A} \vec{r} + \frac{1}{2} \vec{r}^T \vec{B} \vec{r}. \quad (\text{A.17})$$

For definiteness, we set  $\vec{B} = b \vec{I}$ , where  $\vec{I}$  is the identity matrix. We then populate a box of unit length on a side with a set of points, and evaluate the function  $\phi(\vec{r})$  at the coordinates

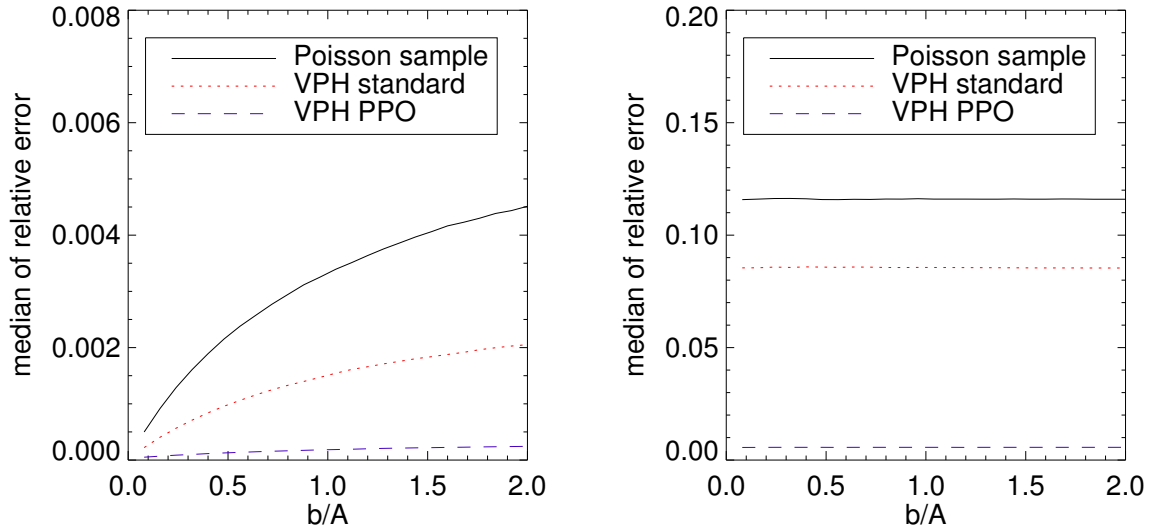


**Figure A.2:** Median relative error in the gradient estimate obtained either with our default formula (left) or with the simpler Green-Gauss estimate where the  $\vec{c}_{ij}$  terms are omitted (right). We show results for three different types of point sets, a Poisson sample (black), a regularized distribution where each Voronoi cell has equal volume (red), and a regularized distribution where in addition the cells are quite ‘round’ and regular (blue). The accuracy is measured as function of the strength of a second order variation in the underlying field.



of each of the points. After constructing the Voronoi tessellation for the point set, we then estimate the local gradient for each cell based on

$$(\nabla\phi)_i = \frac{1}{V_i} \sum_j (\phi_j - \phi_i) A_{ij} \left( \frac{1}{2} \vec{e}_{ij} + \frac{\vec{c}_{ij}}{R_{ij}} \right), \quad (\text{A.18})$$

and alternatively also based on a simpler version of this formula where the terms proportional to  $\vec{c}_{ij}$  are omitted, which corresponds to the simplest version of a Green-Gauss gradient estimate. We use three different point distributions with 4096 points in a box of size unity. First we use a (i) random Poisson point distribution, a (ii) relaxed point distribution obtained from the VPH scheme where each cell has the same volume (obtained from the top of Figure 3.6), and (iii) a distribution relaxed with PPO (obtained from the bottom of Figure 3.6) where in addition very round cells were produced in which the majority of the points lies close to the geometric centres of the cells. In all three cases we compare the magnitude of the estimated gradient vector to the magnitude of  $\vec{A}$ , and we plot the median of the relative error as a function of  $b/|\vec{A}|$ . To exclude boundary effects, only cells whose neighbours do not overlap with the box boundary are considered in the measurement.

In Figure A.2, we show the results. The panel on the left gives our adopted gradient estimate, while the panel on the right is for the simpler version of the Green-Gauss gradient estimate. Interestingly, for  $b = 0$ , the error vanishes exactly, independent of the regularity of the Voronoi mesh. However, once the second order term starts to influence the measurement, i.e. for large values of  $b/|\vec{A}|$ , the more regular meshes clearly yield a lower error, as expected. In all cases, the gradient estimate that includes the  $\vec{c}_{ij}$  term is superior to the simple Green-Gauss gradient estimate. In particular, only when it is included, a vanishing error for a linearly varying field is obtained.

## A.2 Controlling the shape of cells

As outlined in Section 3.3.2, we modify the fluid Lagrangian slightly to include factors that penalize highly distorted cell shapes. If such shapes occur, we want small adjustment forces to appear that tend to make the mesh more regular again. These adjustment forces need to preserve energy and momentum conservation of the scheme, which will automatically be the case if they are derived from a suitably defined Lagrangian or Hamiltonian. In this Appendix, we derive the equations of motion for the Lagrangian

$$L = \sum_k \frac{1}{2} m_k \dot{\vec{r}}_k^2 - \sum_k \frac{P_k V_k}{\gamma - 1} \left[ 1 + \beta_0 \frac{(\vec{r}_k - \vec{s}_k)^2}{V_k^{2/d}} \right] \left\{ 1 + \beta_1 \left( \frac{\vec{w}_k^2}{V_k^{2/d}} - \beta_2 \right) \right\}, \quad (\text{A.19})$$

where the factor in square brackets disfavors displacements of points from the geometric centres of their cells, and the factor in curly brackets disfavors cells with large aspect ratios.

We define the centroid of a cell as

$$\vec{s}_k \equiv \langle \vec{r} \rangle_k = \frac{1}{V_k} \int \vec{r} \chi_k(\vec{r}) d\vec{r}, \quad (\text{A.20})$$

where  $\chi_k$  is the characteristic function of cell  $k$ . The shape of a cell is measured via the second moment

$$\vec{w}_k^2 \equiv \langle (\vec{r} - \vec{s}_k)^2 \rangle_k = \frac{1}{V_k} \int (\vec{r} - \vec{s}_k)^2 \chi_k(\vec{r}) d\vec{r}. \quad (\text{A.21})$$

Here  $d$  counts the number of dimensions, i.e.  $d = 2$  for 2D and  $d = 3$  for 3D. The factor  $V_k^{2/d}$  is hence proportional to the ‘radius’  $R_k = V_k^{1/d}$  of a cell squared.  $\beta_0$  measures the strength of the effect of displacements of points from the centroid of a cell, while  $\beta_1$  is the corresponding factor for the aspect-ratio factor. The constant  $\beta_2$  is only introduced to prevent that even round cells lead to a significant enhancement of the thermal energy. For perfectly round cells, we expect in 2D roughly circles for which  $w_k^2 = V^{2/d}/(2\pi)$ , hence we pick  $\beta_2 = 1/(2\pi)$ . In 3D, we have approximately spheres instead and we pick  $\beta_2 = 3/5(3/4\pi)^{2/3}$ .

Note that this Lagrangian is *only* a function of the point coordinates for given entropies, so the equations of motion for conservative dynamics are perfectly well defined, even though they lead to more lengthy expressions than in the standard case. We first obtain the following Lagrangian equation of motion:

$$m_i \ddot{\vec{r}}_i = \frac{\partial L}{\partial \vec{r}_i} = - \sum_k \frac{1}{\gamma - 1} \left( \frac{\partial}{\partial \vec{r}_i} P_k V_k \right) \left[ \left[ \left\{ \right\} \right] \right] \quad (\text{A.22})$$

$$- \sum_k \frac{P_k V_k}{\gamma - 1} \left\{ \right\} \beta_0 \frac{\partial}{\partial \vec{r}_i} \frac{(\vec{r}_k - \vec{s}_k)^2}{V_k^{2/d}} \quad (\text{A.23})$$

$$- \sum_k \frac{P_k V_k}{\gamma - 1} \left[ \left[ \right] \right] \beta_1 \frac{\partial}{\partial \vec{r}_i} \frac{w_k^2}{V_k^{2/d}}, \quad (\text{A.24})$$

where the empty square and curly brackets are notational short-cuts for the corresponding terms in the original Lagrangian. We note that we can use the identity

$$\frac{\partial}{\partial \vec{r}_i} P_k V_k = (1 - \gamma) P_k \frac{\partial V_k}{\partial \vec{r}_i}. \quad (\text{A.25})$$

We also note that in the second and third terms of equation (A.24) we encounter partial derivatives of  $V_k$ , which we can combine with the first term into a more compact form. This allows us to write the equation of motion in the form

$$m_i \ddot{\vec{r}}_i = \sum_k P_k^* \frac{\partial V_k}{\partial \vec{r}_i} - \sum_k Q_k \frac{\partial}{\partial \vec{r}_i} (\vec{r}_k - \vec{s}_k)^2 - \sum_k L_k \frac{\partial}{\partial \vec{r}_i} w_k^2 \quad (\text{A.26})$$

where we have defined

$$P_k^* \equiv P_k \left( \left[ \left[ \left\{ \right\} \right] \right] + \frac{2}{d} \frac{\beta_0}{\gamma - 1} \frac{(\vec{r}_k - \vec{s}_k)^2}{V_k^{2/d}} \left\{ \right\} + \frac{2}{d} \frac{\beta_1}{\gamma - 1} \frac{w_k^2}{V_k^{2/d}} \left[ \left[ \right] \right] \right) \quad (\text{A.27})$$

and introduced the quantities

$$Q_k \equiv \frac{\beta_0}{\gamma - 1} P_k V_k^{1-2/d} \left\{ \right\}, \quad (\text{A.28})$$

$$L_k \equiv \frac{\beta_1}{\gamma - 1} P_k V_k^{1-2/d} \left[ \right]. \quad (\text{A.29})$$

We already know an explicit expression for  $\partial V_k / \partial \vec{r}_i$ , but we still need to derive such a thing for the derivatives of  $(\vec{r}_k - \vec{s}_k)^2$  and  $w_k^2$ . Let us first deal with the term involving  $Q_k$  in the equations of motion, i.e.

$$\left( m_i \ddot{\vec{r}}_i \right)_Q = - \sum_k Q_k \frac{\partial}{\partial \vec{r}_i} (\vec{r}_k - \vec{s}_k)^2 = -2 \sum_k Q_k \left( \frac{\partial (\vec{r}_k - \vec{s}_k)}{\partial \vec{r}_i} \right)^T (\vec{r}_k - \vec{s}_k). \quad (\text{A.30})$$

Here the exponent  $T$  stands for the transpose, and the notation  $\frac{\partial \vec{a}}{\partial \vec{b}}$  is the Jacobian matrix with elements  $\left( \frac{\partial \vec{a}}{\partial \vec{b}} \right)_{lm} = \frac{\partial a_l}{\partial b_m}$ . Based on the definition of  $\vec{s}_k$  in terms of the characteristic function we find

$$\frac{\partial}{\partial \vec{r}_i} (\vec{r}_k - \vec{s}_k) = \delta_{ki} \mathbf{1} - \frac{1}{V_k} (\vec{r}_k - \vec{s}_k) \left( \frac{\partial V_k}{\partial \vec{r}_i} \right)^T + \frac{1}{V_k} \int d\vec{r} (\vec{r}_k - \vec{r}) \left( \frac{\partial \chi_k}{\partial \vec{r}_i} \right)^T. \quad (\text{A.31})$$

For the derivative of the characteristic function we can use a result from Serrano and Español (2001) and write

$$\frac{\partial \chi_k}{\partial \vec{r}_i} = \sum_j \delta_{ki} \frac{\chi_k \chi_j}{\sigma^2} (\vec{r} - \vec{r}_k) - \frac{\chi_k \chi_i}{\sigma^2} (\vec{r} - \vec{r}_i), \quad (\text{A.32})$$

which is based on approximating the characteristic function with

$$\chi_k(\vec{r}) = \frac{\exp \left[ -\frac{(\vec{r} - \vec{r}_k)^2}{2\sigma^2} \right]}{\sum_j \exp \left[ -\frac{(\vec{r} - \vec{r}_j)^2}{2\sigma^2} \right]}, \quad (\text{A.33})$$

which becomes exact in the limit  $\sigma \rightarrow 0$ . Putting these results into equation (A.30) one gets

$$\left( m_i \ddot{\vec{r}}_i \right)_Q = -2Q_i (\vec{r}_i - \vec{s}_i) + 2 \sum_k \frac{Q_k}{V_k} (\vec{r}_k - \vec{s}_k)^2 \frac{\partial V_k}{\partial \vec{r}_i} \quad (\text{A.34})$$

$$\begin{aligned} & -2 \sum_j \frac{Q_j}{V_j} \int d\vec{r} \frac{\chi_i \chi_j}{\sigma^2} (\vec{r} - \vec{r}_i) (\vec{r}_i - \vec{r})^T (\vec{r}_i - \vec{s}_i) \\ & + 2 \sum_k \frac{Q_k}{V_k} \int d\vec{r} \frac{\chi_i \chi_k}{\sigma^2} (\vec{r} - \vec{r}_i) (\vec{r}_k - \vec{r})^T (\vec{r}_k - \vec{s}_k). \end{aligned} \quad (\text{A.35})$$

We can now identify the area of a face between two cells as

$$A_{ij} = R_{ij} \int d\vec{r} \frac{\chi_i \chi_j}{\sigma^2}, \quad (\text{A.36})$$

and the centroid of the face as

$$\vec{s}_{ij} = \frac{R_{ij}}{A_{ij}} \int d\vec{r} \frac{\chi_i \chi_j}{\sigma^2} \vec{r}. \quad (\text{A.37})$$

Furthermore, we define a second-order tensor of the face relative its centroid as

$$\vec{T}_{ij} = \frac{R_{ij}}{A_{ij}} \int d\vec{r} \frac{\chi_i \chi_j}{\sigma^2} (\vec{r} - \vec{s}_{ij})(\vec{r} - \vec{s}_{ij})^T. \quad (\text{A.38})$$

With these definitions, we can rewrite equation (A.35) as

$$\left( m_i \ddot{\vec{r}}_i \right)_Q = - 2Q_i(\vec{r}_i - \vec{s}_i) \quad (\text{A.39})$$

$$+ 2 \sum_k \frac{Q_k}{V_k} (\vec{r}_k - \vec{s}_k)^2 \frac{\partial V_k}{\partial \vec{r}_i} \quad (\text{A.40})$$

$$+ 2 \sum_{j \neq i} \frac{A_{ii}}{R_{ij}} \left\{ \vec{T}_{ij}(\vec{e}_i - \vec{e}_j) + [(\vec{s}_{ij} - \vec{r}_i)\vec{e}_i - (\vec{s}_{ij} - \vec{r}_j)\vec{e}_j](\vec{s}_{ij} - \vec{r}_i) \right\},$$

where we introduced the further short-cut

$$\vec{e}_i \equiv \frac{Q_i}{V_i} (\vec{r}_i - \vec{s}_i). \quad (\text{A.41})$$

We note that the second term in this equation can be absorbed in yet a further redefinition of  $P_k^*$ , which we will exploit later on. We next consider the term in the full equation of motion that involves the  $L_k$  factor. This is given by

$$\left( m_i \ddot{\vec{r}}_i \right)_L \quad (\text{A.42})$$

$$= - \sum_k L_k \frac{\partial w_k^2}{\partial \vec{r}_i} = - \sum_k L_k \left[ - \frac{w_k^2}{V_k} \frac{\partial V_k}{\partial \vec{r}_i} + \frac{1}{V_k} \int d\vec{r} \frac{\partial \chi_k}{\partial \vec{r}_i} (\vec{r} - \vec{s}_k)^T (\vec{r} - \vec{s}_k) \right] \quad (\text{A.43})$$

$$= \sum_k \frac{L_k w_k^2}{V_k} \frac{\partial V_k}{\partial \vec{r}_i} \quad (\text{A.44})$$

$$- \sum_j \frac{L_i}{V_i} \int d\vec{r} \frac{\chi_i \chi_j}{\sigma^2} (\vec{r} - \vec{r}_i)(\vec{r} - \vec{s}_i)^T (\vec{r} - \vec{s}_i) + \sum_j \frac{L_j}{V_j} \int d\vec{r} \frac{\chi_i \chi_j}{\sigma^2} (\vec{r} - \vec{r}_i)(\vec{r} - \vec{s}_j)^T (\vec{r} - \vec{s}_j).$$

We now define a further moment for each cell face, namely the vector-valued quantity

$$\vec{g}_{ij} \equiv \frac{R_{ij}}{A_{ij}} \int d\vec{r} \frac{\chi_i \chi_j}{\sigma^2} (\vec{r} - \vec{s}_{ij})^2 (\vec{r} - \vec{s}_{ij}). \quad (\text{A.45})$$

Note that  $\vec{g}_{ij}$  always vanishes in 2D but can be non-zero in 3D. With this definition, we

can rewrite equation (A.43) as

$$\left(m_i \ddot{\vec{r}}_i\right)_L \quad (\text{A.46})$$

$$= \sum_k \frac{L_k w_k^2}{V_k} \frac{\partial V_k}{\partial \vec{r}_i} \quad (\text{A.47})$$

$$+ \sum_{j \neq i} \frac{A_{ij}}{R_{ij}} \left\{ \left( \frac{L_j}{V_j} - \frac{L_i}{V_i} \right) \vec{g}_{ij} + 2\vec{T}_{ij}(\vec{f}_j - \vec{f}_i) \right\} \quad (\text{A.48})$$

$$+ \frac{A_{ij}}{R_{ij}} \left\{ \left[ (\vec{f}_j(\vec{s}_{ij} - \vec{s}_j) - \vec{f}_i(\vec{s}_{ij} - \vec{s}_i)) + \text{Tr}(\vec{T}_{ij}) \left( \frac{L_j}{V_j} - \frac{L_i}{V_i} \right) \right] (\vec{s}_{ij} - \vec{r}_i), \right\}$$

where we have defined the short-cut

$$\vec{f}_i \equiv \frac{L_i}{V_i} (\vec{s}_{ij} - \vec{s}_i). \quad (\text{A.49})$$

Again, the first term involving  $\partial V_k / \partial \vec{r}_i$  can be absorbed into a redefinition of  $P_k^*$ . Putting everything together, the complete equation of motion can then be written as

$$\begin{aligned} & m_i \ddot{\vec{r}}_i \quad (\text{A.50}) \\ & = \sum_k P_k^{**} \frac{\partial V_k}{\partial \vec{r}_i} - 2Q_i(\vec{r}_i - \vec{s}_i) \\ & + \sum_{j \neq i} \frac{A_{ij}}{R_{ij}} \left\{ 2\vec{T}_{ij}(\vec{e}_i - \vec{e}_j + \vec{f}_j - \vec{f}_i) \right. \\ & + \left[ 2(\vec{s}_{ij} - \vec{r}_i)\vec{e}_i - 2(\vec{s}_{ij} - \vec{r}_j)\vec{e}_j + (\vec{s}_{ij} - \vec{s}_j)\vec{f}_j - (\vec{s}_{ij} - \vec{s}_i)\vec{f}_i + \text{Tr}(\vec{T}_{ij}) \left( \frac{L_j}{V_j} - \frac{L_i}{V_i} \right) \right] (\vec{s}_{ij} - \vec{r}_i) \\ & \left. + \left( \frac{L_j}{V_j} - \frac{L_i}{V_i} \right) \vec{g}_{ij} \right\}, \quad (\text{A.51}) \end{aligned}$$

where we have defined

$$P_k^{**} = P_k^* + \frac{L_k w_k^2}{V_k} + \frac{2Q_k(\vec{r}_k - \vec{s}_k)^2}{V_k}. \quad (\text{A.52})$$

While a bit lengthy, this can be straightforwardly calculated for the VPH scheme. Nevertheless, we want to add a brief note on how to compute the Tensors  $T_{ij}$ , which is done as part of the mesh construction. We have

$$\langle (\vec{r} - \vec{s})^2 \rangle_k = \langle (\vec{r} - \vec{r}_0)^2 \rangle_k - (\vec{r}_0 - \vec{s})^2 \quad (\text{A.53})$$

for any reference point  $\vec{r}_0$ . Suppose we have a triangle in 2D given by  $(\vec{r}_0, \vec{r}_1, \vec{r}_2)$ , then the moment can be obtained as

$$\langle (\vec{r} - \vec{r}_0)^2 \rangle_k = \frac{1}{6} [(\vec{r}_1 - \vec{r}_0)(\vec{r}_1 - \vec{r}_0)^T + (\vec{r}_1 - \vec{r}_0)(\vec{r}_2 - \vec{r}_0)^T + (\vec{r}_2 - \vec{r}_0)(\vec{r}_2 - \vec{r}_0)^T]. \quad (\text{A.54})$$

Similar relations hold for 3D and can be exploited for an efficient calculation of the tensors  $\vec{T}_{ij}$  and the vectors  $\vec{g}_{ij}$ .



# Appendix B

## More stripping results for the VPH code

### B.1 Wind tunnel simulations

#### B.1.1 Stripped clumps

To further elucidate the nature of the stripped gas, in Figure B.1 we show the evolution of the star forming mass that is spatially close to the galaxy centre and therefore fulfills Eq. (4.3), compared to the total star forming gas as defined by Eq. (4.2). The figure shows that especially in SPH clumps of the ISM that are stripped nevertheless continue to form stars, and therefore fulfill Eq. (4.2) but not Eq. (4.3). Hence the curve representing Eq. (4.3) is substantially below the curve representing all star forming gas. Both curves merge after a time  $\approx 0.5$  Gyr when the clumps exit the simulation domain of the wind tunnel. Note that VPH shows significantly less stripped gas that still forms stars, whereas in AREPO such gas is almost completely absent.

#### B.1.2 Statistical analysis of resolution elements

In Figure B.2, we compare the simulation methods with respect to where the resolution elements are to be found as a function of density. The plot reveals that SPH tends to concentrate its resolution elements in the galaxy centre, whereas the transition region between the galaxy and the wind is least well resolved. AREPO on the other hand has most of its resolution elements in this transition area. VPH lies in between these two codes.

#### B.1.3 Variable wind properties

In Chapter 4, we have only investigated the influence of a constant wind with a constant mass loading. However, we may also try to arrive at a more realistic temporal behaviour of the wind, say by varying the velocity of the headwind and its density. This can, for example, be done in terms of the time dependent properties of Section 4.5 (Figure 4.17),

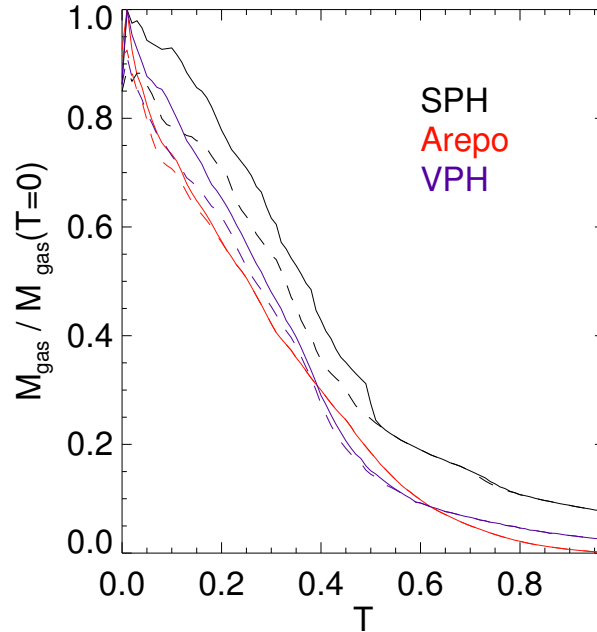


**Figure B.1:** Loss of star-forming ISM gas as a function of time due to stripping through a supersonic wind. The gas remaining in the ISM of the galaxy is here measured according to the criteria of Eq. (4.2) (solid lines), and with both Eq. (4.2) and Eq. (4.3). Shown are the simulations with SPH, VPH and AREPO, as labelled. We find that the stripping is quite similar in VPH and AREPO, but significantly less efficient in SPH.

measured directly in a full hydrodynamic simulation. In this specific example we find in agreement with Gunn and Gott (1972) that a reduced wind density at early times leads to a slower stripping of the gas (top panel in Figure B.3), hence the gas remains longer in the main galaxy and forms more stars (bottom panel in Figure B.3). Therefore, the sum of the mass of star-forming gas and the mass of the newly formed stars (bottom panel in Figure B.3) stays at a higher level. This can also be seen in the corresponding plot of the simulation of Section 4.5, which is depicted in Figure B.4. Here the sum of star-forming gas and the mass of the newly formed stars also stays at a nearly constant level.



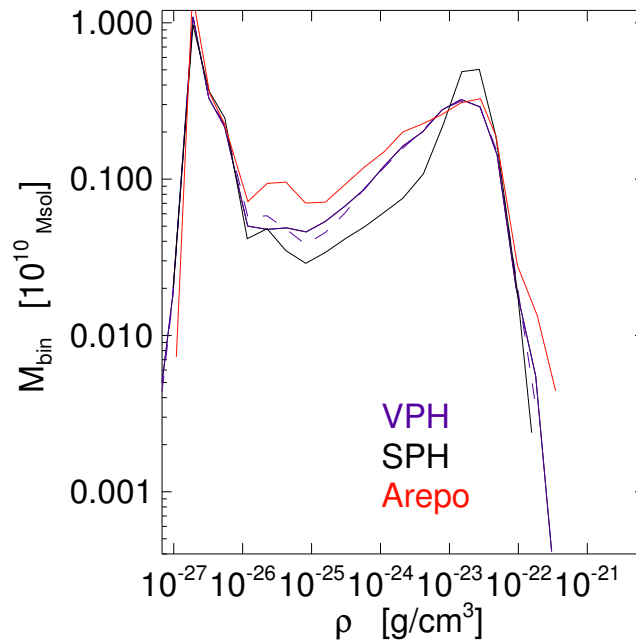


**Figure B.2:** A statistical analysis of the distribution of resolution elements over density, for simulations of a galaxy exposed to a supersonic wind at  $t = 0.04$  Gyr, carried out with three different numerical techniques. This demonstrates that the resolution elements are distributed differently depending on the method (solid lines, as labelled). The blue dotted line is a variant of VPH which used an artificial mixing scheme. Please note that due to the variable mass of the resolution elements in AREPO, the AREPO curve (red) represents the number of resolution elements per bin times the average mass of all gas particles.

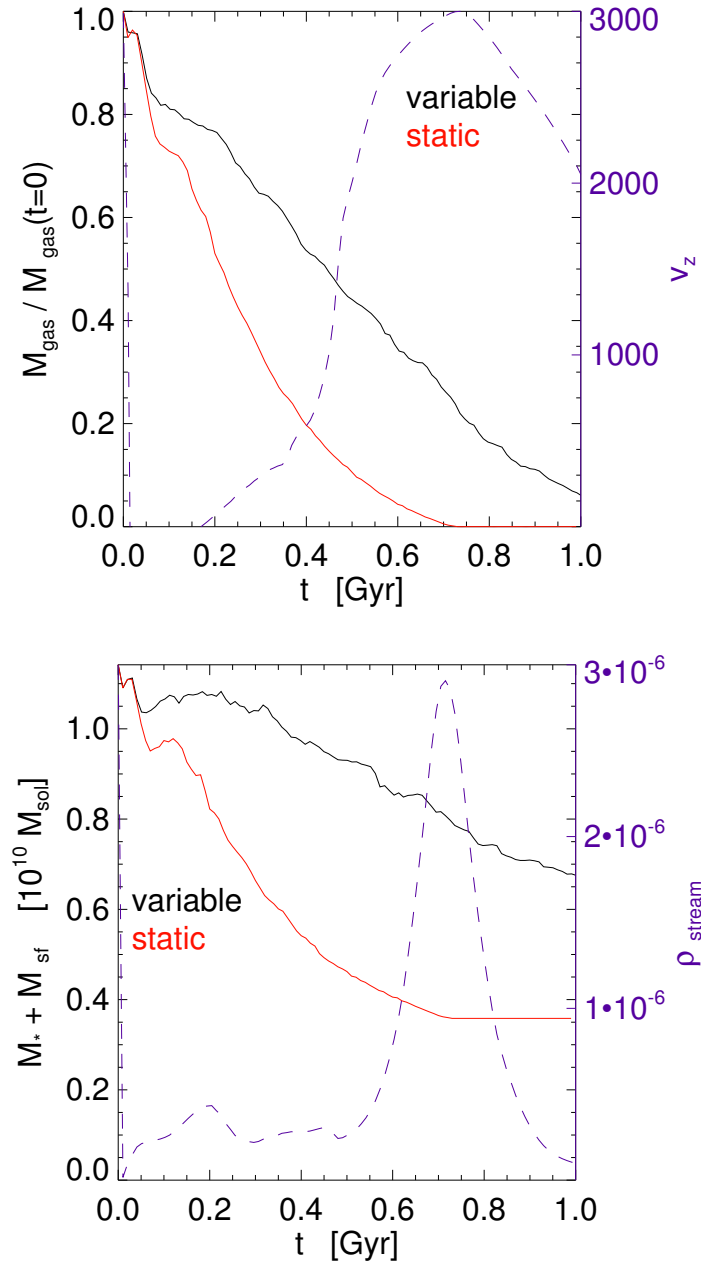


**Figure B.3:** A galaxy in a wind tunnel experiencing a static flow of wind compared to a more realistic simulation with varying velocity (dashed blue in top panel) and varying wind density (dashed blue in bottom panel). Both simulations are AREPO-based. Shown is the sum of the mass of the remaining star forming gas plus the newly formed stellar mass as a function of time.

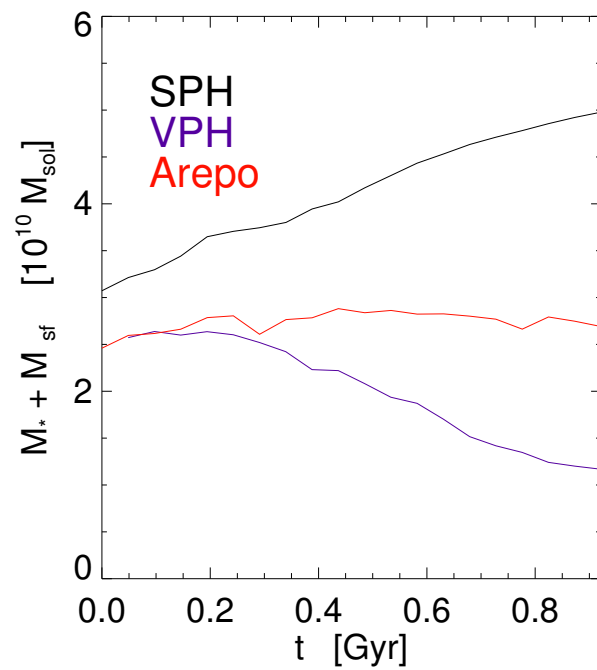


**Figure B.4:** Sum of the mass of star-forming gas and formed stars for an infalling galaxy within a distance of 20 kpc from the galaxy centre as a function of time. We include simulation results for SPH (black), VPH (blue) and AREPO (red).



# References

- Abadi, M. G., Moore, B., and Bower, R. G. (1999). Ram pressure stripping of spiral galaxies in clusters. *MNRAS*, 308:947–954.
- Agertz, O., Moore, B., Stadel, J., Potter, D., Miniati, F., Read, J., Mayer, L., Gawryszczak, A., Kravtsov, A., Nordlund, Å., Pearce, F., Quilis, V., Rudd, D., Springel, V., Stone, J., Tasker, E., Teyssier, R., Wadsley, J., and Walder, R. (2007). Fundamental differences between SPH and grid methods. *MNRAS*, 380:963–978.
- Balsara, D. S. (1995). von Neumann stability analysis of smooth particle hydrodynamics— suggestions for optimal algorithms. *J. Comp. Phys.*, 121:357–372.
- Barnes, J. and Hut, P. (1986). A hierarchical  $O(N \log N)$  force-calculation algorithm. *Nature*, 324:446–449.
- Cole, S., Percival, W. J., Peacock, J. A., Norberg, P., Baugh, C. M., Frenk, C. S., Baldry, I., Bland-Hawthorn, J., Bridges, T., Cannon, R., Colless, M., Collins, C., Couch, W., Cross, N. J. G., Dalton, G., Eke, V. R., De Propris, R., Driver, S. P., Efstathiou, G., Ellis, R. S., Glazebrook, K., Jackson, C., Jenkins, A., Lahav, O., Lewis, I., Lumsden, S., Maddox, S., Madgwick, D., Peterson, B. A., Sutherland, W., and Taylor, K. (2005). The 2dF Galaxy Redshift Survey: power-spectrum analysis of the final data set and cosmological implications. *MNRAS*, 362:505–534.
- da Silva, A. C., Barbosa, D., Liddle, A. R., and Thomas, P. A. (2000). Hydrodynamical simulations of the Sunyaev-Zel’dovich effect. *MNRAS*, 317:37–44.
- Dave, R., Dubinski, J., and Hernquist, L. (1997). Parallel TreeSPH. *New Astronomy*, 2:277–297.
- De Fabritiis, G., Serrano, M., Delgado-Buscalioni, R., and Coveney, P. V. (2006). Fluctuating hydrodynamic modelling of fluids at the nanoscale. *ArXiv Physics e-prints*, physics/0612230.
- Dirichlet, G. L. (1850). *Reine Angew. Math.*, 40:216.
- Dolag, K., Borgani, S., Murante, G., and Springel, V. (2009). Substructures in hydrodynamical cluster simulations. *MNRAS*, 399:497–514.

- Dolag, K., Vazza, F., Brunetti, G., and Tormen, G. (2005). Turbulent gas motions in galaxy cluster simulations: the role of smoothed particle hydrodynamics viscosity. *MNRAS*, 364:753–772.
- Duc, P., Brinks, E., Springel, V., Pichardo, B., Weilbacher, P., and Mirabel, I. F. (2000). Formation of a Tidal Dwarf Galaxy in the Interacting System Arp 245 (NGC 2992/93). *AJ*, 120:1238–1264.
- Einasto, J. (1965). *Trudy Inst. Astrofiz. Alma-Ata*, 5:87.
- Evrard, A. E. (1988). Beyond N-body - 3D cosmological gas dynamics. *MNRAS*, 235:911–934.
- Frenk, C. S., White, S. D. M., Bode, P., Bond, J. R., Bryan, G. L., Cen, R., Couchman, H. M. P., Evrard, A. E., Gnedin, N., Jenkins, A., Khokhlov, A. M., Klypin, A., Navarro, J. F., Norman, M. L., Ostriker, J. P., Owen, J. M., Pearce, F. R., Pen, U.-L., Steinmetz, M., and et al., T. (1999). The Santa Barbara Cluster Comparison Project: A Comparison of Cosmological Hydrodynamics Solutions. *ApJ*, 525:554–582.
- Gao, L., White, S. D. M., Jenkins, A., Stoehr, F., and Springel, V. (2004). The subhalo populations of  $\Lambda$ CDM dark haloes. *MNRAS*, 355:819–834.
- Gingold, R. A. and Monaghan, J. J. (1977). Smoothed particle hydrodynamics - Theory and application to non-spherical stars. *MNRAS*, 181:375–389.
- Governato, F., Willman, B., Mayer, L., Brooks, A., Stinson, G., Valenzuela, O., Wadsley, J., and Quinn, T. (2007). Forming disc galaxies in  $\Lambda$ CDM simulations. *MNRAS*, 374:1479–1494.
- Gunn, J. E. and Gott, III, J. R. (1972). On the infall of matter into cluster of galaxies and some effects on their evolution. *Astrophys. J.*, 176:1–19.
- Gunn, J. E. and Gott, III, J. R. (1972). On the Infall of Matter Into Clusters of Galaxies and Some Effects on Their Evolution. *ApJ*, 176:1–+.
- Helly, J. C., Cole, S., Frenk, C. S., Baugh, C. M., Benson, A., and Lacey, C. (2003). Galaxy formation using halo merger histories taken from N-body simulations. *MNRAS*, 338:903–912.
- Hernquist, L. (1993). N-body realizations of compound galaxies. *ApJS*, 86:389–400.
- Hernquist, L. and Katz, N. (1989). TREESPH - A unification of SPH with the hierarchical tree method. *ApJS*, 70:419–446.
- Hernquist, L., Katz, N., Weinberg, D. H., and Miralda-Escudé, J. (1996). The Lyman-Alpha Forest in the Cold Dark Matter Model. *ApJL*, 457:L51+.

- Heß, S. and Springel, V. (2010). Particle hydrodynamics with tessellation techniques. *MNRAS*, 406:2289–2311.
- Hockney, R. W. and Eastwood, J. W. (1981). Numerical simulations using particles. *MNRAS*.
- Iapichino, L. and Niemeyer, J. C. (2008). Hydrodynamical adaptive mesh refinement simulations of turbulent flows - II. Cosmological simulations of galaxy clusters. *MNRAS*, 388:1089–1100.
- Icke, V. and van de Weygaert, R. (1987). Fragmenting the universe. *A&A*, 184:16–32.
- Jáchym, P., Palouš, J., Köppen, J., and Combes, F. (2007). Gas stripping in galaxy clusters: a new SPH simulation approach. *A&A*, 472:5–20.
- Jarosik, N., Bennett, C. L., Dunkley, J., Gold, B., Greason, M. R., Halpern, M., Hill, R. S., Hinshaw, G., Kogut, A., Komatsu, E., Larson, D., Limon, M., Meyer, S. S., Nolta, M. R., Odegard, N., Page, L., Smith, K. M., Spergel, D. N., Tucker, G. S., Weiland, J. L., Wollack, E., and Wright, E. L. (2010). Seven-Year Wilkinson Microwave Anisotropy Probe (WMAP) Observations: Sky Maps, Systematic Errors, and Basic Results. *ArXiv e-prints*.
- Jubelgas, M., Springel, V., and Dolag, K. (2004). Thermal conduction in cosmological SPH simulations. *MNRAS*, 351:423–435.
- Kapferer, W., Sluka, C., Schindler, S., Ferrari, C., and Ziegler, B. (2009). The effect of ram pressure on the star formation, mass distribution and morphology of galaxies. *A&A*, 499:87–102.
- Kowalski, M., Rubin, D., Aldering, G., Agostinho, R. J., Amadon, A., Amanullah, R., Baland, C., Barbary, K., Blanc, G., Challis, P. J., Conley, A., Connolly, N. V., Covarrubias, R., Dawson, K. S., Deustua, S. E., Ellis, R., Fabbro, S., Fadeyev, V., Fan, X., Farris, B., Folatelli, G., Frye, B. L., Garavini, G., Gates, E. L., Germany, L., Goldhaber, G., Goldman, B., Goobar, A., Groom, D. E., Haissinski, J., Hardin, D., Hook, I., Kent, S., Kim, A. G., Knop, R. A., Lidman, C., Linder, E. V., Mendez, J., Meyers, J., Miller, G. J., Moniez, M., Mourão, A. M., Newberg, H., Nobili, S., Nugent, P. E., Pain, R., Perdureau, O., Perlmutter, S., Phillips, M. M., Prasad, V., Quimby, R., Regnault, N., Rich, J., Rubenstein, E. P., Ruiz-Lapuente, P., Santos, F. D., Schaefer, B. E., Schommer, R. A., Smith, R. C., Soderberg, A. M., Spadafora, A. L., Strolger, L., Strovink, M., Suntzeff, N. B., Suzuki, N., Thomas, R. C., Walton, N. A., Wang, L., Wood-Vasey, W. M., and Yun, J. L. (2008). Improved Cosmological Constraints from New, Old, and Combined Supernova Data Sets. *ApJ*, 686:749–778.
- Kronberger, T., Kapferer, W., Ferrari, C., Unterguggenberger, S., and Schindler, S. (2008). On the influence of ram-pressure stripping on the star formation of simulated spiral galaxies. *A&A*, 481:337–343.

- Landau, L. D. and Lifshitz, E. M. (1966). *Hydrodynamik, Lehrbuch der theoretischen Physik, Berlin: Akademie-Verlag, 1966.*
- Larson, R. B. (1978). A finite-particle scheme for three-dimensional gas dynamics. *Journal of Computational Physics*, 27:397–409.
- Lucy, L. B. (1977a). A numerical approach to the testing of the fission hypothesis. *AJ*, 82:1013–1024.
- Lucy, L. B. (1977b). A numerical approach to the testing of the fission hypothesis. *AJ*, 82:1013–1024.
- Mayer, L., Quinn, T., Wadsley, J., and Stadel, J. (2002). Formation of Giant Planets by Fragmentation of Protoplanetary Disks. *Science*, 298:1756–1759.
- McCarthy, I. G., Frenk, C. S., Font, A. S., Lacey, C. G., Bower, R. G., Mitchell, N. L., Balogh, M. L., and Theuns, T. (2008). Ram pressure stripping the hot gaseous haloes of galaxies in groups and clusters. *MNRAS*, 383:593–605.
- McCarthy, I. G., Schaye, J., Ponman, T. J., Bower, R. G., Booth, C. M., Dalla Vecchia, C., Crain, R. A., Springel, V., Theuns, T., and Wiersma, R. P. C. (2010). The case for AGN feedback in galaxy groups. *MNRAS*, 406:822–839.
- Mihos, J. C. and Hernquist, L. (1996). Gasdynamics and Starbursts in Major Mergers. *ApJ*, 464:641.
- Mitchell, N. L., McCarthy, I. G., Bower, R. G., Theuns, T., and Crain, R. A. (2009). On the origin of cores in simulated galaxy clusters. *MNRAS*, 395:180–196.
- Monaghan, J. J. (1992). Smoothed particle hydrodynamics. *ARA&A*, 30:543–574.
- Monaghan, J. J. (1997). Sph and riemann solvers. *J. Comp. Phys.*, 136:298.
- Monaghan, J. J. (2005). Smoothed particle hydrodynamics. *Reports on Progress in Physics*, 68(8):1703–1759.
- Morris, J. (1997). A Switch to Reduce SPH Viscosity. *Journal of Computational Physics*, 136:41–50.
- Navarro, J. F., Frenk, C. S., and White, S. D. M. (1996). The Structure of Cold Dark Matter Halos. *ApJ*, 462:563–+.
- Navarro, J. F., Hayashi, E., Power, C., Jenkins, A. R., Frenk, C. S., White, S. D. M., Springel, V., Stadel, J., and Quinn, T. R. (2004). The inner structure of  $\Lambda$ CDM haloes - III. Universality and asymptotic slopes. *MNRAS*, 349:1039–1051.
- Pelupessy, F. I., Schaap, W. E., and van de Weygaert, R. (2003). Density estimators in particle hydrodynamics. DTFE versus regular SPH. *A&A*, 403:389–398.



- Percival, W. J., Reid, B. A., Eisenstein, D. J., Bahcall, N. A., Budavari, T., Frieman, J. A., Fukugita, M., Gunn, J. E., Ivezić, Ž., Knapp, G. R., Kron, R. G., Loveday, J., Lupton, R. H., McKay, T. A., Meiksin, A., Nichol, R. C., Pope, A. C., Schlegel, D. J., Schneider, D. P., Spergel, D. N., Stoughton, C., Strauss, M. A., Szalay, A. S., Tegmark, M., Vogeley, M. S., Weinberg, D. H., York, D. G., and Zehavi, I. (2010). Baryon acoustic oscillations in the Sloan Digital Sky Survey Data Release 7 galaxy sample. *MNRAS*, 401:2148–2168.
- Petkova, M. and Springel, V. (2009). An implementation of radiative transfer in the cosmological simulation code GADGET. *MNRAS*, 396:1383–1403.
- Press, W. H. and Schechter, P. (1974). Formation of Galaxies and Clusters of Galaxies by Self-Similar Gravitational Condensation. *ApJ*, 187:425–438.
- Price, D. J. (2008). Modelling discontinuities and Kelvin Helmholtz instabilities in SPH. *Journal of Computational Physics*, 227:10040–10057.
- Price, D. J. and Monaghan, J. J. (2007). An energy-conserving formalism for adaptive gravitational force softening in smoothed particle hydrodynamics and N-body codes. *MNRAS*, 374:1347–1358.
- Puchwein, E., Springel, V., Sijacki, D., and Dolag, K. (2010). Intracluster stars in simulations with active galactic nucleus feedback. *MNRAS*, 406:936–951.
- Quilis, V., Moore, B., and Bower, R. (2000). Gone with the Wind: The Origin of S0 Galaxies in Clusters. *Science*, 288:1617–1620.
- Rasio, F. A. and Shapiro, S. L. (1991). Collisions of giant stars with compact objects - Hydrodynamical calculations. *ApJ*, 377:559–580.
- Read, J. I., Hayfield, T., and Agertz, O. (2009). Resolving mixing in Smoothed Particle Hydrodynamics. *ArXiv e-prints*, 0906.0774.
- Ritchie, B. W. and Thomas, P. A. (2001). Multiphase smoothed-particle hydrodynamics. *MNRAS*, 323:743–756.
- Robertson, B., Yoshida, N., Springel, V., and Hernquist, L. (2004). Disk Galaxy Formation in a  $\Lambda$  Cold Dark Matter Universe. *ApJ*, 606:32–45.
- Roediger, E. and Brüggen, M. (2006). Ram pressure stripping of disc galaxies: the role of the inclination angle. *MNRAS*, 369:567–580.
- Roediger, E. and Brüggen, M. (2007). Ram pressure stripping of disc galaxies orbiting in clusters - I. Mass and radius of the remaining gas disc. *MNRAS*, 380:1399–1408.
- Rosswog, S. (2009). Astrophysical smooth particle hydrodynamics. *New Astronomy Review*, 53:78–104.

- Saitoh, T. R. and Makino, J. (2009). A Necessary Condition for Individual Time Steps in SPH Simulations. *ApJL*, 697:L99–L102.
- Scannapieco, C., Tissera, P. B., White, S. D. M., and Springel, V. (2008). Effects of supernova feedback on the formation of galaxy discs. *MNRAS*, 389:1137–1149.
- Schaap, W. E. and van de Weygaert, R. (2000). Continuous fields and discrete samples: reconstruction through Delaunay tessellations. *A&A*, 363:L29–L32.
- Schaap, W. V. (2007). The Delaunay Tessellation Field Estimator.
- Serrano, M. and Español, P. (2001). Thermodynamically consistent mesoscopic fluid particle model. *Phys Rev E*, 64:046115.
- Shen, S., Wadsley, J., Hayfield, T., and Ellens, N. (2009). A numerical study of brown dwarf formation via encounters of protostellar discs. *MNRAS*, page 1634.
- Springel, V. (2005a). The cosmological simulation code GADGET-2. *MNRAS*, 364:1105–1134.
- Springel, V. (2005b). The cosmological simulation code GADGET-2. *MNRAS*, 364:1105–1134.
- Springel, V. (2009). E pur si muove: Galilean-invariant cosmological hydrodynamical simulations on a moving mesh. *ArXiv e-prints*, 0901.4107, *MNRAS*, in press.
- Springel, V. (2010a). E pur si muove: Galilean-invariant cosmological hydrodynamical simulations on a moving mesh. *MNRAS*, 401:791–851.
- Springel, V. (2010b). Smoothed Particle Hydrodynamics in Astrophysics. *ARA&A*, 48:391–430.
- Springel, V., Di Matteo, T., and Hernquist, L. (2005a). Black Holes in Galaxy Mergers: The Formation of Red Elliptical Galaxies. *ApJL*, 620:L79–L82.
- Springel, V. and Hernquist, L. (2002). Cosmological smoothed particle hydrodynamics simulations: the entropy equation. *MNRAS*, 333:649–664.
- Springel, V. and Hernquist, L. (2003). Cosmological smoothed particle hydrodynamics simulations: a hybrid multiphase model for star formation. *MNRAS*, 339:289–311.
- Springel, V. and White, S. D. M. (1999). Tidal tails in cold dark matter cosmologies. *MNRAS*, 307:162–178.
- Springel, V., White, S. D. M., Jenkins, A., Frenk, C. S., Yoshida, N., Gao, L., Navarro, J., Thacker, R., Croton, D., Helly, J., Peacock, J. A., Cole, S., Thomas, P., Couchman, H., Evrard, A., Colberg, J., and Pearce, F. (2005b). Simulations of the formation, evolution and clustering of galaxies and quasars. *Nature*, 435:629–636.

- Springel, V., White, S. D. M., Jenkins, A., Frenk, C. S., Yoshida, N., Gao, L., Navarro, J., Thacker, R., Croton, D., Helly, J., Peacock, J. A., Cole, S., Thomas, P., Couchman, H., Evrard, A., Colberg, J., and Pearce, F. (2005c). Simulations of the formation, evolution and clustering of galaxies and quasars. *Nature*, 435:629–636.
- Springel, V., Yoshida, N., and White, S. D. M. (2001). GADGET: a code for collisionless and gasdynamical cosmological simulations. *New Astronomy*, 6:79–117.
- Steinmetz, M. and Mueller, E. (1993). On the capabilities and limits of smoothed particle hydrodynamics. *A&A*, 268:391–410.
- Sunyaev, R. A., Norman, M. L., and Bryan, G. L. (2003). On the Detectability of Turbulence and Bulk Flows in X-ray Clusters. *Astronomy Letters*, 29:783–790.
- Tasker, E. J., Brunino, R., Mitchell, N. L., Michielsen, D., Hopton, S., Pearce, F. R., Bryan, G. L., and Theuns, T. (2008). A test suite for quantitative comparison of hydrodynamic codes in astrophysics. *MNRAS*, 390:1267–1281.
- van de Weygaert, R. and Icke, V. (1989). Fragmenting the universe. II - Voronoi vertices as Abell clusters. *A&A*, 213:1–2.
- van de Weygaert, R. and Schaap, W. (2009). The Cosmic Web: Geometric Analysis. In V. J. Martinez, E. Saar, E. M. Gonzales, & M. J. Pons-Borderia, editor, *Lecture Notes in Physics, Berlin Springer Verlag*, volume 665 of *Lecture Notes in Physics, Berlin Springer Verlag*, page 291.
- Vazza, F., Tormen, G., Cassano, R., Brunetti, G., and Dolag, K. (2006). Turbulent velocity fields in smoothed particle hydrodynamics simulated galaxy clusters: scaling laws for the turbulent energy. *MNRAS*, 369:L14–L18.
- Voronoi, G. F. (1908). *Reine Angew. Math.*, 134:198.
- Wadsley, J. W., Stadel, J., and Quinn, T. (2004). Gasoline: a flexible, parallel implementation of TreeSPH. *New Astronomy*, 9:137–158.
- Wadsley, J. W., Veeravalli, G., and Couchman, H. M. P. (2008a). On the treatment of entropy mixing in numerical cosmology. *MNRAS*, 387:427–438.
- Wadsley, J. W., Veeravalli, G., and Couchman, H. M. P. (2008b). On the treatment of entropy mixing in numerical cosmology. *MNRAS*, 387:427–438.
- Weinmann, S. M., van den Bosch, F. C., Yang, X., Mo, H. J., Croton, D. J., and Moore, B. (2006). Properties of galaxy groups in the Sloan Digital Sky Survey - II. Active galactic nucleus feedback and star formation truncation. *MNRAS*, 372:1161–1174.
- White, S. D. M. and Rees, M. J. (1978). Core condensation in heavy halos - A two-stage theory for galaxy formation and clustering. *MNRAS*, 183:341–358.



# Acknowledgements

I would like to thank my wife, without her this work wouldn't exist. I would also like to thank my daughter and my family for their support.

Also I would like to say that it is thanks to Volker Springel, that the work has been possible in this way. Furthermore my thanks go to Simon White and the Max-Planck-Institut für Astrophysik for their enduring support.

<b>Name</b>		Steffen Heß
<b>Date of Birth</b>		March 3rd, 1981
<b>Citizenship</b>		German
<b>Address</b>		Kopernikusstr. 31 14482 Potsdam
<b>Degrees</b>	2007	Diploma in physics at the Julius-Maximilian-Universität-Würzburg. Topic of the Diploma thesis: <i>Simulations of Cosmic Superstrings.</i>
	2005	<i>Master of Physics in Physical Science with Honours of the First Class,</i> Heriot-Watt University Edinburgh.
<b>Studies</b>	January 2011:	Unemployed
	October 2010:	Parental leave
	since May 2007:	PhD in Astrophysics at the Max-Planck-Institut für Astrophysik
	April 2007:	Diploma thesis at the Julius-Maximilian-Universität Würzburg. supervised by Prof. Dr. Jens Niemeyer
	April 2006:	Examination to Diploma in physics
	June 2005:	Examination to Master of Physics.
	Sept. 2004:	Student at the Heriot-Watt University Edinburgh in <i>General Physics and Physical Science.</i>
	Sept. 2003:	Pre-Diploma in physics.
<b>Zivildienst</b>	2000 – 2001:	'Offene Behindertenarbeit' Regens-Wagner-Stiftung
<b>School</b>	1991 – 2000:	Gymnasium Hilpoltstein, Abitur in May 2000.